APPLICATION OF AIRCRAFT'S FLIGHT TESTING TECHNIQUES TO THE AERODYNAMIC CHARACTERIZATION OF POWER KITES

Ricardo Borobia Moreno

A thesis submitted in partial fulfilment of the requirements for the degree of Doctor of Philosophy in the

Programa Interuniversitario en Mecánica de Fluidos

Universidad Carlos III de Madrid

Advisors:
Gonzalo Sánchez-Arriaga

Tutor:
Gonzalo Sánchez-Arriaga

January 2021

Dedicated to my daughter Elia.

ACKNOWLEDGEMENTS

PUBLISHED AND SUBMITTED CONTENT

Some of the research activities carried out in this thesis work have been presented in:

- R. Borobia-Moreno, A. Serino, H. Endo, and G. Sánchez-Arriaga. "Flight Testing Setup for the Aerodynamic Characterization of Power Kites Applied to Airborne Wind Energy Generation". World Wind Energy Conference (WWEC2017). Poster contribution 2017

  Material from this publication is partially included in Chapter 3. Author Roles: The experimental setup has been specified and designed by Ricardo Borobia (RB) and manufactured and integrated by RB and Alejandro Serino (AS) with the supervision of Gonzalo Sánchez (GS). The poster contribution was elaborated by RB, Hiroki Endo (HE) and GS.

- R. Borobia-Moreno, G. Sánchez-Arriaga, and R. Schmehl. "Application of the Estimation-Before-Modeling Method to the Aerodynamic Characterization of Power Kites". In Proceedings of: Airborne Wind Energy Conference 2017: (AWEC 2017). 2017, p.26. DOI: http://doi.org/10.4233/uuid:4c361ef1-d2d2-4d14-9868-16541f60edc7.

  Material from this publication is partially included in Chapter 3 and Chapter 4 and to a smaller extent in Chapter 5. Author roles: RB carried out the development and integration of the method. Results were analysed by RB and GS. Paper was written by RB and GS with the supervision of Roland Schmehl (RS).

- R. Borobia-Moreno, D. Ramiro-Rebollo, G. Sánchez-Arriaga, and R. Schmehl. "Flight Testing, Aerodynamic Parameter Identification and Dynamic Simulation of Rigid and Flexible Kites Applied to Airborne Wind Energy Systems". In Proceedings of: Airborne Wind Energy Conference 2019: (AWEC 2019). 2019, p. 133. DOI: https://doi.org/10.4233/uuid:57fd203c-e069-11e9-9fcb-441ea15f7c9c.

  Material from this publication is partially included in Chapter 3, Chapter 4 and Chapter 5. Author roles: RB carried out the development of the method. Ramiro Rebollo (RR) contributed to improving the experimental setup. Results were analysed by RB and GS. Paper was written by RB and GS with the supervision of Roland Schmehl (RS).

And published in:

- R. Borobia-Moreno, G. Sánchez-Arriaga, A. Serino, and R. Schmehl. "Flight-Path Reconstruction and Flight Test of Four-Line Power Kites." In: Journal of Guidance, Control, and Dynamics 41.12 (2018), pp. 2604-2614. DOI: 10.2514/1.G003581.

  Material from this publication is partially included in Chapter 3, Chapter 4 and Chapter 5. Author roles: RB developed the method and designed the experimental setup. AS collaborated in the manufacturing and integration of the experimental setup. RB and GS analysed the obtained results. The paper was written by RB and GS and supervised by RS.

- R. Borobia-Moreno, D. Ramiro-Rebollo, R. Schmehl, and G. Sánchez-Arriaga. "Identification of kite aerodynamic characteristics using the estimation before modeling technique." In: Wind Energy (2021). DOI: https://doi.org/10.1002/we.2591.

  Material from this publication is partially included in Chapter 3, Chapter 4 and Chapter 5. Author roles: RB developed the method and RR contributed to improving the experimental setup. RB and GS analysed the obtained results. The paper was written by RB and GS with the supervision of RS.

- G. Sánchez-Arriaga, A. Pastor-Rodríguez, R. Borobia-Moreno, and R. Schmehl. "A constraint-free flight simulator package for airborne wind energy systems." In: Journal of Physics: Conference Series 1037 (2018), p. 062018. DOI: 10.1088/1742 6596/1037/6/062018

  Material from this publication is partially included to a smaller extent in Chapter 5. Author roles: GS and Alejandro Pastor (AP) developed the method. RB contributed at analysing the simulation output and its comparison with experimental data. The paper was written by GS and AP with the supervision of RS.

The material from these sources included in this thesis is not singled out with any typographic means and/or references.

OTHER RESEARCH MERITS

- R. Borobia-Moreno, I. Castro, A. Pastor, H. Endo, C. Cobos, R. Cavallaro, and G. Sánchez-Arriaga. "Activities and Roadmap on Airborne Wind Energy Systems at UC3M." In: Journal of Japan Wind Energy Society 44.134 (2020).

  Author Roles: The paper was written by RB, Iván Castro (IC), AP, Rauno Cavallaro (RC) and GS. HE and Carlos Cobos (CC) contributed to Airborne Wind Energy Systems UC3M activities.

ABSTRACT

This thesis has developed an experimental methodology for the flight testing and data analysis of power kites applied to Airborne Wind Energy Systems (AWES). In particular, the *Estimation Before Modeling* technique, a well-known method in the aerospace industry for the aerodynamic characterization of an aircraft using real flight data, has been adapted for tethered aircraft. The developed methodology has two main building blocks: (i) an experimental setup to record experimental data during the flight testing, and (ii) a Flight Path Reconstruction algorithm to estimate the state of the system from the experimental data. From them, the aerodynamic characteristics of two types of kites were investigated.

The proposed experimental setup was designed to be low cost, portable and easily adaptable to both, rigid and semi-rigid kites. It is composed of an instrumented kite representative of the ones used in AWES, an instrumented control bar, a ground computer and a wind station. Whenever it was possible, commercial off the shelf components have been used, including low cost open-hardware sensors based on the PixHawk platform. However, after the first flight tests were conducted and the obtained results were discussed, high precision sensors were also included.

The *Flight Path Reconstruction* (FPR) algorithm for tethered aircraft is based on an *Extended Kalman Filter* (EKF). In addition to the standard set of estimated state variables (ie. Euler angles, position or ground speed), the algorithm also provides the aerodynamic torque and forces upon the kite as well as the tether tensions and wind velocity vector. The EBM technique, and the FPR algorithm have been used to identify the aerodynamic characteristics of both, four-line *Leading Edge Inflatable* (LEI) kites and two-line *Rigid Frame Delta* (RFD) kites. Quantitative and qualitative results have been obtained. Albeit both types of kites exhibited very high AoA during the flight, some significant differences were found. In particular, the estimated lift coefficient of the LEI kite showed a behavior identified with a post-stall condition, while the RFD showed a pre-stall behavior with a lower AoA and a positive relation between the lift coefficient and the kite AoA.

The presented experimental methodology can be of great interest for AWE industry as it helps to improve modeling of tethered aircraft, leading to more accurate performance figures which may increase investors interest in the technology. Moreover, flight testing methodologies and experimental data analysis are of great interest for benchmarking AWES performances, contributing to de-risk their development process and providing better tools for AWE "best concept" identification. Finally, as a sub-product of the presented methodology, the FPR algorithm can be used as a validated state estimator of the tethered aircraft, which is a key element of a closed loop flight control system.

LIST OF ABBREVIATIONS

AAA	**A**dvanced **A**ircraft **A**nalisys
ADC	**A**nalog to **D**igital **C**onverter
AoA	**A**ngle **o**f **A**ttack
AoS	**A**ngle **o**f **S**ideslip
AWE	**A**irborne **W**ind **E**nergy
AWES	**A**irborne **W**ind **E**nergy **S**ystems
CFD	**C**omputational **F**luid **D**ynamic
CoG	**C**enter **o**f **G**ravity
COTS	**C**ommercial **O**ff **T**he **S**helf
DATCOM	**DAT**a **COM**pendium
EASA	**E**uropean **A**viation **S**afety **A**gency
EBM	**E**stimation **B**efore **M**odeling
EKF	**E**xtended **K**alman **F**ilter
EU	**E**uropean **U**nion
FAA	**F**ederal **A**viation **A**dministration
FCS	**F**light **C**ontrol **S**ystem
FG	**F**light **G**eneration
FPR	**F**light **P**ath **R**econstruction
GG	**G**round **G**eneration
GPS	**G**lobal **P**osition **S**ystem
IAS	**I**ndicated **A**ir **S**peed
IMU	**I**nertial **M**easurement **U**nit
INTA	**I**nstituo **N**acional **d**e **T**écnica **A**erospacial
ISA	**I**nternational **S**tandard **A**tmosphere
LEI	**L**eading **E**dge **I**nflatable
RFD	**R**igid **F**rame **D**elta
R&D	**R**esearch **a**nd **D**evelopment
TAS	**T**rue **A**ir **S**peed
TRL	**T**echnology **R**eadiness **L**evel
USAF	**U**nited **S**tates **A**ir **F**orce

Contents

List of Figures

List of Tables

List of Symbols

$\boldsymbol{B}$	magnetic field	T
$\tilde{d}_{\pm}$	distance sensor measurements	m
D_{cb}	control bar displacement	m
$\boldsymbol{F}_a$	aerodynamic force	N
$\tilde{\boldsymbol{f}}_{IMU}$	specific force	$\mathrm{m\,s^{-2}}$
$\boldsymbol{M}_a$	aerodynamic torque	N m
$\boldsymbol{V}_{wind}$	wind vector	$\mathrm{m\,s^{-1}}$
m_k	kite mass	kg
S	kite surface	$\mathrm{m^2}$
L_{cb}	length of the control bar	m
L_{ds}	de-power stopper distance	m
L_l	lengths of the frontal lines	m
L_{ps}	power stopper distance	m
L_t	lengths of the rear lines	m
L_s	length of the sliding tether	m
$\bar{\boldsymbol{Q}}$	process covariance matrix	
$\bar{\boldsymbol{R}}$	observation covariance matrix	
$\bar{\boldsymbol{R}}_{EK}$	Earth to Kite-Body axis rotation matrix	
s_0	control bar-to-load cell distance	m
$\boldsymbol{r}$	kite position	m
$\boldsymbol{T}$	tether tension	N
$\boldsymbol{v}$	kite velocity	$\mathrm{m\,s^{-1}}$
w_{cl}	width of the chicken-loop interface	m
Δp	differential pressure	Pa
η	sensor noise	
Υ	Euler angles vector	rad
ω	kite angular velocity	$\mathrm{rad\,s^{-1}}$
ρ	air density	$\mathrm{kg\,m^{-3}}$
θ	pitch angle	rad
Θ	instrument bias	
ψ	yaw angle	rad
ϕ	roll angle	rad
ν	control bar deflection angle	rad
χ	Markov state vector	
σ^2	variances	
u_p	power ratio of the control bar	

Subscripts and accents

k	kite
K	Kite body-frame
E	Earth-frame
$A_\pm$	Attachment points $A_\pm$
$B_\pm$	Attachment points $B_\pm$
$\hat{x}$	Estimated value of x
$\tilde{x}$	Measured value of x

1 INTRODUCTION

Energy, loosely defined as ***the capacity to perform work***, and specifically the capacity to transform energy from one form to another, have been deeply related to human progress and technological development. When about 1.000.000 years ago, Homo Erectus achieved the ability (by means of an exothermic oxidation chain-reaction), to transform into heat the *chemical energy* stored in the carbon chains of vegetable fuels, a new era of energy dependence started. Fire domination allowed early humans not only to improve their diet but also to provide heat and light and ultimately opened the door to crafting. The Agricultural Revolution increased the amount of available food and the first permanent human settlements appeared increasing human population. But It was not until about 2500 years ago [63], that the first watermills were invented to transform the potential energy of water into mechanical work for crushing grain. Water and windmills were the first attempt to look for new energy resources in an economy based on biomass consumption.

By the end of the XIX century, a technical milestone in England changed the world. The steam engine allowed humans to transform chemical energy into mechanical energy and marked the beginning of the industrial era and the transformation from the so called *Organic Energy Economy* to the *Fossil Fuel Economy* [36]. As shown in Fig.1.1, world population almost doubled just in the first half of the XX century.
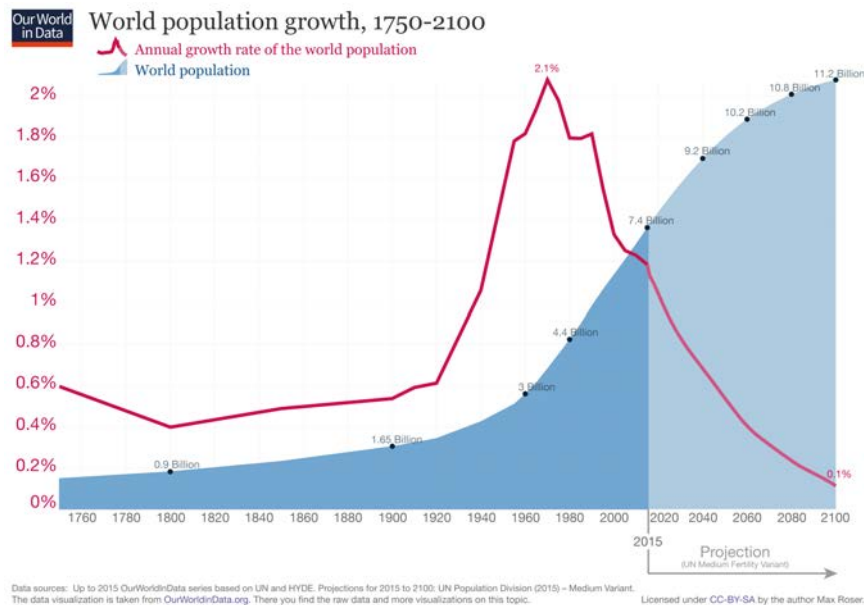
FIGURE 1.1: Evolution of the world population [82].

In the second half of the XX century that world population annual growth reached its higher peak, and population doubled again by the end of the century. This growth matches with an unprecedented increase of the humanity energy consumption as shown in Fig. 1.2. This huge increment was achieve almost in its totality by means of fossil fuels consumption. Since then, energy dependence and human population have constantly increased. Heavy industrial processes in a consumer focused economy and democratization of transportation in the second half of the century, largely contributed to a great dependence on fossil fuels. This process took place firstly in the so called "first world" countries as the relatively cheap and easy to obtain energy contributed to their economical development, and nowadays, it is still happening at a greater scale in other in-developing countries.
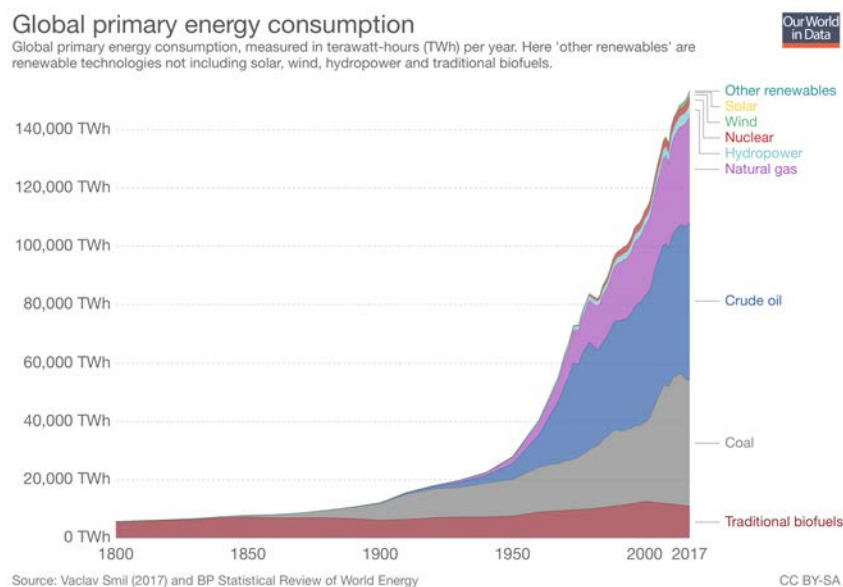
FIGURE 1.2: Evolution of the world global primary energy consumption [81].

The fast development of humanity during the last century, the most impressive and fruitful in human history, has been based on a unparalleled technological and energetic dependent development. However it has come at a cost, and human responsibility on climate change and global warming is mostly widely accepted. During the last decades a social consensus has appeared around the need to find new forms of energy, which should allow humanity to keep the pace of technological and social development while preserving the environment. Nevertheless, developed countries have the moral responsibility to lead this process as they were the main beneficiaries of the industrial revolution of the XXth century.

1.1 A shift to carbon-free energy sources

Energy is a conserved quantity (thus it can be neither created or destroyed), but it may exist in many different forms. Generally speaking, we refer to primary energy sources to natural resources from which energy can be extracted by its conversion to any other energy form which is of interest for human activity. A classical example of energy source are the so called fossil fuels, which are natural resources which store huge amount of chemical energy which can be transformed for example into mechanical or electrical energy. Although it could be argued that almost all the available primary energy sources come from nuclear energy which is transformed into other forms of energy in both natural (the stars), or human made nuclear reactors, the term renewable energy source is established to denote primary energy sources which are naturally replenished on a human time scale. Examples of those renewable primary energy sources are the kinetic energy present on the Earth atmosphere or the electromagnetic radiation received in the Earth surface directly from the Sun. However other energy sources such as biomass or geothermal energy can also been considered renewable.

When at the beginning of the twentieth century the world economy switched to a Fossil Fuel Economy, humans started to deplete a limited, not renewable (at least in a human timescale) energy source, but also started to do it in a manner which inexorability implied the emission of combustion residuals to the atmosphere (namely COx but also NOx, SOx... or solid particles). These emissions are mostly accepted to be responsible not only of Earth global warming but also of many human diseases. For these reason, major countries are promoting emissions reductions mainly by the use of alternative renewable, carbon free, energy sources. At this regard, Kyoto Protocol was intended to be an *"international agreement linked to the United Nations Framework Convention on Climate Change, which commits its Parties by setting internationally binding emission reduction targets"*. [18].

To achieve the objective of reducing the effects that modern society have on climate change, the new energy sources need to be renewable, and the transformation process of this energy must be emission free and safe. For this reason, electrical energy (electric potential energy) is called to play a main role in the de-carbonization of human activity. Electrical energy is not a primary energy source as it can not be widely found in the nature to be easily exploited by humans. It is a secondary energy source because humans have learned how to effectively and cleanly (emission free) transform it into other useful energy forms such as heat, mechanical or electromagnetic energy. However, this is not without one major caveat; humans do not know any way to directly "store" electrical potential energy, other than the capacitor. Any other attempt to store "electricity" is based on one or more transformations to other different forms of energy (e.g batteries relay on transforming electrical energy into chemical energy for storage and back to electrical energy for consumption). This adds complexity, economic cost and efficiency lost. Nevertheless, there is still not a practical economical way to store big enough

amounts of electricity in a global scale [1], representing a great technical problem for the electrification of energy demanding human activities. This is true not only for the more obvious mobility use cases, but also for installed power management, grid design and operation. As "electricity" must be produced "just in time" for being consumed, power management can not relay on conservative return periods for electrical demand, and close to peak demands must be considered at a great economical cost. Electric energy generation technologies which cannot provide demand tracking, as is the case of renewables, just make the problem worse. For these reasons, higher capacity factors [2] and usage rates are of great interest when looking for newer and better renewable technologies, as is the case for wind energy.

Figure. 1.3 puts into perspective the technological challenge that switching to a carbon free economy represents for a developed economy. The figure shows the amount of total energy consumed in Spain and the fraction of that energy that is consumed nowadays in the form of electrical energy. It must be denoted that even if electrification of some activities such as transportation or heating sector were achieved, there are still many industrial process which are highly energetic dependent and will probably take much longer to switch. Finally, as electricity can not be considered a primary energy source, but an intermediate one, the process will only be completed if we are able to develop the technological resources to harvest such a huge amount of energy from renewable sources.
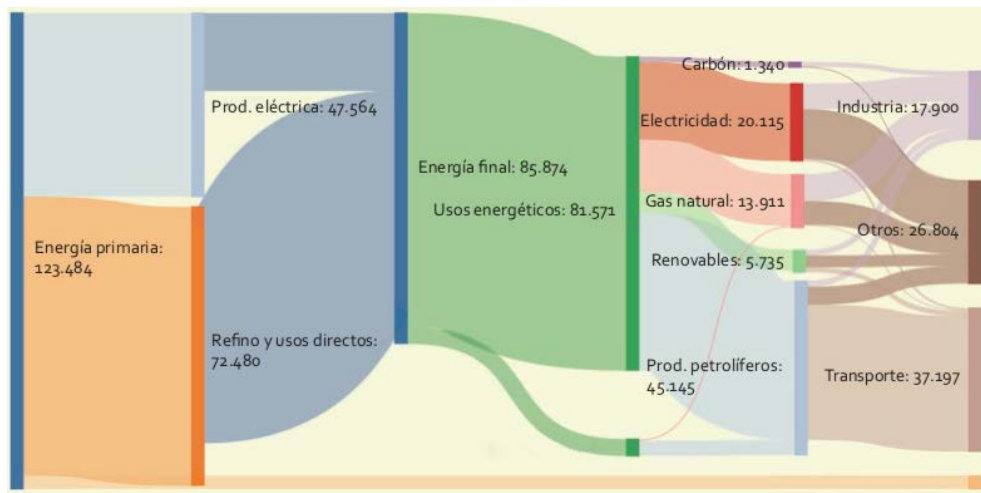
FIGURE 1.3: Sankey diagram for the Spanish energetic structure as in 2016 (KTEP). [77]

---

[1]Pumped storage in hydroelectric power stations, where electricity is transformed into water potential energy and back to electricity when needed, have been largely used for a long time, but it's not universally available due to orographic and hydric requirements and comes at a huge efficiency cost

[2]Ratio of the average generated power to the rated peak power.

1.2 Airborne Wind Energy Systems (AWES)

"Airborne wind energy is the umbrella name for a series of concepts to convert wind energy into electricity, sharing one common feature: the use of one or more automated aerial vehicles linked to the ground by one (or more) tether(s)"[27]

Although the first attempts to transform the kinetic energy of the wind into mechanical energy dates from the ancient Greece, and windmills have been used for centuries to grind cereals (Fig. 1.4) or even to pump water, it was not until the end of nineteenth century that the first wind turbines for electricity generation were designed. The first wind turbines were produced in series in Denmark in 1979. By the end of 1980, the first commercial wind farm started generating electricity at Crotched Mountain in Southwest New Hampshire. This milestone represented the beginning of a whole new industry. Since the end of the twentieth century, wind turbines have become the most successful system to harvest energy from a renewable source and constitute by far the renewable generation system with a higher installed capacity.

FIGURE 1.4: WindMills in Campo de Criptana, Ciudad Real (Spain) [89].

Figure. 1.5 shows an overview of wind power global status as in December 2017. Total installed wind power is reported to be as high as 539 GW, of which 35% are installed in China , 17% in USA and 10% in Germany. Among the new installed capacity in 2017 (52 GW), 4.3 GW were installed offshore (an 87% increase on the 2016 offshore market)[22]. Moreover, the price of the produced KWh is constantly decreasing with a new minimum of US$ 0.02/KWh produced in Mexico in a fast transition to an unsubsidized future in competition with traditional energy generation systems [22]. As any other system, each renewable energy generation technology has its own design scenario, being the yearly allowance of the sun's radiation at each location normally a mayor equilibrium factor between different technologies. Nowadays new hybrid solutions are being explored, combining solar/wind/storage plants capable to provide 24/7 renewable energy in a micro grid arrangement and looking for higher capacity factors. For pure wind power generation, these capacity factors are increasing to values up to 50% [78], while peak wind turbines power are reaching the 5MW per unit. However, architecture scalability is starting to show as a limitation factor. This point of inflection is reported to be approaching for some technologies such as power conversion systems or structural design where material constraints are so

significant[22]. This limitations are being mitigated by an effort to look for new offshore locations, where stronger and more constant winds can provide higher usage rates. Other revolutionary designs could become more competitive and AWEs may represent this new wind generation technology.

TOP 10 NEW INSTALLED CAPACITY JAN-DEC 2017		
Country	MW	% Share
PR China	19,660	37
USA	7,017	13
Germany	6,581	12
United Kingdom	4,270	8
India	4,148	8
Brazil	2,022	4
France	1,694	3
Turkey	766	1
South Africa	618	1
Finland	535	1
Rest of the world	5,182	10
Total TOP 10	47,310	90
World Total	52,492	100
		Source: GWEC

TOP 10 CUMULATIVE CAPACITY DEC 2017		
Country	MW	% Share
PR China	188,392	35
USA	89,077	17
Germany	56,132	10
India	32,848	6
Spain	23,170	4
United Kingdom	18,872	4
France	13,759	3
Brazil	12,763	2
Canada	12,239	2
Italy	9,479	2
Rest of the world	82,391	15
Total TO P10	456,732	85
World Total	539,123	100
		Source: GWEC

FIGURE 1.5: Wind Energy as in December 2017 [22].

Airborne Wind Energy Systems (AWES) are systems that allow to harvest energy from higher atmosphere layers (over 200m) than conventional wind turbines. In principle, they will do it with a theoretically lower capital cost and infrastructure requisites as they will use flexible structures instead of fixed, rigid ones. At those higher atmosphere layers, the available energy is much higher than close to the surface [7] due to more constant and strong trade winds, which will also allow to increase the usage rates and capacity factors of conventional wind turbines. In 2013, Marvel et al. [67] published a study estimating the available kinetic energy in the upper layers of atmosphere to be as high as 1800TW. In this study, climatic consequences of atmosphere kinetic energy extraction was considered negligible at the levels of present global energy demands.

The first idea for an AWE system was developed by American engineer Miles Loyd in 1980 [62]. His work presented the scenario of a kite flying crosswind trajectories to induce an aerodynamic speed higher than wind speed. Loyd found that on a crosswind trajectory, generated apparent wind speed could be as high as $V_{wind}\frac{Lift}{Drag}$, thus for a

typical efficiency ratio $\frac{Lift}{Drag} = 5$, expected aerodynamic forces would be us much as 25 times the generated by the same kite flying in a static scenario. Maximum theoretical achievable power by a kite flying a crosswind trajectory was determined by Loyd to be,

$$P_{max} = \frac{2}{27}\rho A V_{wind}^3 C_L(\frac{C_L}{C_D})^2 \tag{1.1}$$

where C_L and C_D are the lift and drag coefficients, A is the reference area for the kite, and V_{wind} and ρ are the wind speed and atmospheric density at the given flying altitude and location.

Since Wubbo J. Ockels presented the LadderMill concept [54] in the 1999 European Energy Conference, AWEs have constantly increased the interest of academia. In 2009 the first Phd Thesis was published [32] and, since then, AWEs related publications have constantly increased. Also, many experimental projects and startups have been created around AWEs. In 2001 Skysails was founded in Germany to explore the use of power kites to aid ship's propulsion. In 2006 Makani power and KiteGen projects were started in USA and Italy respectively. Basic technology demonstrators were developed around 2006 at Politecnico di Torino [17] and at Delft University of Technology [103]. In June 2009 Ampyx Power in the Netherlands demonstrated power production with their first prototype AP0. Nowadays, a dynamic scientific and industrial community has been establish around AWEs, mostly of it represented under the umbrella of Airborne Wind Europe association created in 2017 [3].

1.2.1 Overview of AWEs typology and architecture.

Airborne Wind Energy Systems aim is to harvest energy from the atmosphere at altitudes which are not feasible for conventional wind turbines. All AWEs designs should provide a solution for,

- Transform the kinetic energy of the wind into electrical energy.

- Distribute the generated electric energy to the ground (when generated on board) and ultimately to the consumers (both off-grid or on-grid).

- Provide a way to place the required airborne structure at the desired atmosphere layers.

- Be able to operate autonomously, continuously and in a safe and robust manner.

In the following, depending on the solutions given to each of these requirements, a classification of the architectures that have been explored for AWE systems is provided.

Flying vs Ground-Generation AWEs.

There are two main solutions to harvest energy from the wind several hundred of meters over the Earth surface: Fly-Generation (FG) and Ground-Generation (GG) systems.

FG systems transform the kinetic energy of the moving air into electrical energy directly on board of the aircraft. This is done by means of an electric generator coaxial with a turbine which is placed directly into the air flow over the aircraft. This solution requires to transport the onboard generated electrical energy to the ground where is distributed to the grid or final consumers. This is usually done through the same tether(s) which links the aircraft to the ground. A great example of a Flying-Generation system is Makani's design (Fig. 1.6).
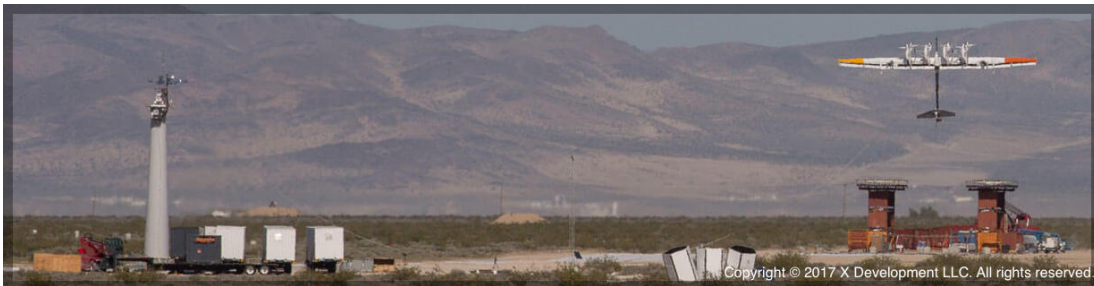
FIGURE 1.6: Makani M600. Rated Power 600KW [65].

The system is composed of a fixed ground station and a tethered drone. In this design, a conductive tether provides the electrical connection with the ground station. Unlike GG systems, its length is constant during the generation phase. The tethered drone is equipped with several wind turbines over the leading edge of its rigid wing and it is designed to take off vertically using these turbines as rotors (consuming energy). Once it has reach the desired flying altitude, it flies crosswind trajectories with the turbines extracting energy from the air flow and driving the on board electric generators. A major caveat of these systems is the added complexity and high cost of the tethered drone, which results in higher development risks and operation costs. Nevertheless, since February 2020 Makani is no longer an Alphabet company and has ceased all its activities, while its developed technologies and software have been open-sourced for the community [61].

Other FG designs propose stationary airborne devices such as a regular wind turbine lifted by and aerostatic balloon [5], by a kite, or even a combined solution similar to an auto gyro (rotor-craft).

GG systems transform the kinetic energy of the wind into mechanical energy which is transferred to the ground. The mechanical energy is transformed into electrical energy by an electrical generator on the ground. There are several ways to transfer the mechanical energy to the ground:

- Pumping is the most successful and explored GG method. In this design, the generated aerodynamic force by the kite is transferred to the ground through the tether tension which can change its length (producing work). This work is used on the ground to spin a drum coaxial with the electric generator. This is achieved reeling out the tether from the drum by the lifting force (generation phase). Once the tether has been completely reeled out, the kite flies at minimum lifting attitude and the tether is reeled in (wasting energy). This method is also known as a jo-jo method because it alternates reel-out/reel-in generating and consuming phases. Great examples of pumping systems are Kitegen designs in Italy (Fig. 1.7) and KitePower [57] and Ampix-Power [6] in the Netherlands.

FIGURE 1.7: KiteGen KSU1. Rated Power 40KW [56].

- Roto-kite. In this design, several stacked kites fly circular trajectories around an imaginary coaxial axis and generate a torque that is transferred to the ground. This torque drives the electric generator on the ground.

- LadderMill. In W. Ockels' design, a group of kites fly an ascendant and descendant vertical trajectory producing a linear displacement of a continuous loop. This is achieved by changing the relative angle of attack of the kites on the ascent and descent phases of the loop, while the whole string is supported by the lifting force of the kites. The generated rotation motion of the "ladder" is transmitted to the ground driving the electric generator.

- Other designs include linear/rotary carousels or Magnus effect. In a carousel design, kites transfer momentum to linear or rotatory mobile ground stations, and the motion of the ground station is transformed into electrical energy. In Magnus effect-based design, a rotary cylindrical device transfers the torque produced by Magnus effect to the ground by a continuous belt that spins an electric generator.

Crosswind vs Stationary Flying Trajectories.

Depending on the flying trajectories, systems can be classified as stationary or crosswind flying systems. In a **stationary system**, the flying device is only used to place the generation devices on the upper atmosphere layers, but not to induce an aerodynamic speed higher than the wind speed (stationary flight). Examples of this technology are W. Ockels' LadderMill [54] where a lifting kite supports the LadderMill, or Altaeros systems [5] where an aerostatic balloon supports a conventional wind turbine. **Crosswind generation systems** are distinguished by the fast motion of the aircraft in a plane which is roughly perpendicular to the absolute wind flow. In this fast motion,

they generate an aerodynamic speed which can be several times the wind speed. All the pumping systems described above as well as Makani and other Flying-Generation systems use crosswind trajectories. Nowadays, stationary flying systems are focused on low to medium energy generation power while the consensus for systems focused or large scale deployment is based on crosswind operation due to the scalability of the concept and much higher produced power.

Fixed vs Mobile Ground Station systems.

Depending on the typology of the ground station, they can be designed as fixed or mobile. In a **fixed system**, the ground station itself does not play an active roll in the conversion of the kinetic energy of the wind into electrical energy. Its function is only to physically host the required ground equipments and provide an anchor point for the tethered aircraft. While fixed ground station designs can be both Flying or Ground-Generation systems, all the pumping designs have a fixed ground station which host the drum and electrical generator.

In a **mobile system**, the whole ground station is a part of the energy conversion chain (by definition, all the mobile designs are Ground-Generation systems), as it is towed by the flying device linearly along a closed loop rail or in a circular motion (carousel). The mechanical energy of the moving ground station is converted into electrical energy. The main advantage of a mobile ground station is that they are conceived as continuous generation systems, as there is no need to reel-in/reel-out pumping phases. In this configuration, the ground station is towed continuously by one or more aircraft generating power at the same time. However, the increased complexity of the system and bigger footprint have caused that so far, all the existing AWE prototypes are based on fixed ground stations.

Aerostatics vs Aerodynamic Airborne Structures.

By definition, AWEs systems relay in an airborne structure tethered to the ground. To generate the required lift to support this structure into the upper layers of the atmosphere there are two possible approaches: aerodynamic or aerostatic lift. In an **aerodynamic system**, the airborne structure has an aerodynamic profile designed to generate lift in the wind flow while in an **aerostatic system**, the airborne structure is designed to be lighter than air. Nowadays most of the AWEs designs (and in particular all the AWEs flying on crosswind trajectories) are based on aerodynamic lifting devices.

1.2.2 Development of AWE systems

In September 2018, the Directorate-General for Research and Innovation of the European Commission published a study on *Challenges in the commercialization of airborne wind energy systems* [27]. In this document, the technological state of AWE systems is reviewed, market potential and barriers are discussed, and measures and a pathway

towards commercialization are outlined.

The technology readiness levels (TRLs) of the different AWE technologies are derived in the study according with the guidance principles for renewable energy technologies [31]. For high capacity, scalable designs based on crosswind flying trajectories, the most advanced designs are reported to be in a TRL 5 to 6 for FG systems based on tethered drones, and TRL 4 to 5 for "pumping" GG systems, corresponding with large scale and small scale prototypes being developed respectively. While simulation and small scale proof of concept are outlined as being the main areas of interest in AWES in the last years, power scalability and automatic, long term operation demonstration, including automatic take-off and landing, are reported to be of great interest in the coming years for the industry.

A comprehensive review of the barriers to AWEs development is provided in the study, and they are classified as

- **Exogenous conditions**, are related to potential wind resources, spatial and airspace foot print and extreme weather operation. In this regard, preliminary studies show promising resources potential, where high altitude operation is expected to provide higher utilization factors in comparison with conventional wind turbines which may overcome increased operation complexity. However, better modeling of wind resources at higher atmosphere layers are outlined to be necessary. Also, definition of required additional information for kite operation is expected from the industry, specially for extreme weather operation. Finally, preliminary site assessment for AWEs deployment requires realistic performance figures for power generation and it impacts on the viability of the systems.

- **Industry and market barriers** are within the AWEs industry domain and comprise technology readiness, safety and economic performance. One year autonomous continuous operation seems to be the consensus accepted milestone for technology reliability demonstration. This long term operation will require several capabilities which are still to be demonstrated, such as autonomous take off and landing, emergency/bad weather operation and availability factor optimization by fly level adjustment. However, next short term industry efforts, according to the study, are more focused on systems up-scaling versus continuous operation tests to demonstrate AWE viability versus conventional wind power industry. This will come at an economic performance penalization as up-scaling will increase the cost of both crashing or bad picking on the best AWE technology (which nowadays is still to be determined), representing a barrier for future investors.

  Diversification of risk, parallel development of small scale prototypes for testing new capabilities before implementation in the big-scale ones, development of supply chains readiness and economies of scale are called to mitigate these barriers. However some key components of AWEs, such as Flight Control

Systems (FCS) are expected to stay developed in-house as a differentiating point between different companies.

- **Public support and regulatory barriers**, relate with social acceptability (*not in my backyard* concept), environmental impact (expected to be higher than for conventional wind turbines), funding availability and regulatory environment.

Funding availability is required for basic research support, facilitation of test sites and de-risk of development process. R&D output sharing is outlined in the study to be still insufficient which slows the convergence of industry on the "best concept", as there is still little to none validation of technology based on experimental data. Performance and results of present technology demonstrators are considered within the company intellectual property and are not usually shared. Nevertheless, a common testing facility in a well-instrumented and controlled operating environment, is required for different AWEs demonstrators comparison and evaluation. This will accelerate the "best concept" identification, and by doing so, will minimize the risk of possible early stage investors/administrations of funding the wrong concept. Finally, the up-scaling process presents a high-cost, high-risk scenario not very attractive for future investors. Risk sharing through subsidizing or co-financing by the public sector is shown as an instrument to overcame this barrier.

Environment and airspace regulation can highly influence the development of AWEs. National aviation authorities, as well as the European Aviation Safety Agency (EASA) in EU or The Federal Aviation Administration (FAA) in USA, must be provided with evidence that operation of AWE systems will not endanger other airspace users as well as people on the ground. According to the report, the effort required to provide such an evidence could be underestimated by the industry.

The analysis of the described state of AWE technologies, as well as the barriers for AWEs development and commercialization shown in the European Commission report, show that there is still a long path towards a fully operational AWE solution. Although a great effort has been made by the community on simulation and proof of concept demonstration in the last decade, a better understanding and modeling of AWE systems is still highly desirable. In particular, overcoming most of the barriers outlined in the study will require precise flight simulation and modeling of the airborne structure of AWEs.

Performance evaluation, which is a key factor for the industry as they are going to compete with conventional wind energy technologies, will require precise modeling of both the wind resources and the system behavior. Capacity factors and peak power of the system is going to be largely influenced by the flying characteristics of the aircraft, and the capacity of its FCS to perform optimal trajectories. Development of such FCS and identification of such trajectories requires a precise simulation environment.

Indeed, bad weather operation, autonomous take off/landing or systems up-scaling will require increased complexity autonomous control capabilities. De-risk of the development process is going to be highly related with the capability of the industry to provide a simulation environment which will allow engineers to accurately study new technical solutions before even implementing and testing them in real world prototypes. This is not different to any other modern engineering environment, and in particular in the aerospace industry where off-line and real-time, software in the loop and hardware in the loop flight simulators are constantly used to develop and test new FCS among others characteristics.

Finally, public support to the AWE industry, as stated in the study, will require clear comparison metrics between different technologies as well as R&D output sharing to facilitate "best concept" identification. This will require to build up flight testing tools and strategies which allow the industry to benchmark the proposed prototypes as well as testing and validating the different designs and performance figures. Nevertheless, aviation authorities will require both numerical and experimental evidence of AWES airworthiness which will require precise modeling of the systems as well as flight testing methods and tools.

1.3 Contributions of this dissertation

This thesis is aimed at the improvement of the modeling of AWE systems flying cross-wind trajectories. Given a known initial condition, simulation of a dynamic system response (in the sense of the space state theory) refers to the time propagation of the initial state vector of the system. An accurate mathematical representation of both, the inertial properties of the system (its mass, center of mass position and tensor of inertia about the center of mass) as well as all the forces and torques acting upon the system (as a function of the state vector and control inputs to the system) are required.

A mathematical representation of the generated lift, drag and side force, as well as pitch, roll and yaw torques as a function (among others), of the relative orientation of the body within the air flow, and the absolute relative speed of the airflow over the body (aerodynamic speed), is called and aerodynamic model and it is a fundamental piece of the simulation tools. To generate this mathematical representation, several approaches can be used,

- **Preliminary analysis** based on physics or semi-empirical methods such as DAR Corporation Advanced Aircraft Analysis (AAA) [24], or the USAF Stability and Control DATCOM [20]. Those methods are very well suited for fast preliminary modeling of conventional aircraft and are usually used as a starting point prior to the detail modeling phase. However they are not very well suited for detailed aerodynamic characterization specially when the aerodynamic devices are far from conventional aircraft, or the flying envelope of the system broadness to no linear regimenes such as close to or post stall situations. Unfortunately, both of this situations characterize AWE systems.

- **Numerical methods**, i.e. Computational Fluid Dynamics (CFD), can be used for detailed aerodynamic modeling. However, they are time consuming and require multiple runs for multiple aerodynamic configurations so they are not very well suited for flexible or semi-flexible aerodynamic structures (kites). Also, complex situations such as turbulent flow or boundary layer separation requires special and computationally expensive methods.

- **Wind tunnel tests** require a sensorized aerodynamic body into an artificial airflow in a controlled environment. The generated aerodynamic forces and torques are directly measured for different conditions. However, the big size of the AWE aircraft , and the complexity of their structure, which some times relay on the tension on the tethers to provide the final shape of the aircraft (kite), make difficult and very costly to perform wind tunnel tests.

- **Flight testing** obtains the values of the different aerodynamic coefficients from data logged on real flight tests. Usually this method has been used in the aerospace industry to improve or validate the available aerodynamic models of a given flying aircraft as well as to increase the flying envelope of the given aerodynamic model.

This thesis focuses on providing a methodology aimed at obtaining a better aerodynamic characterization of a tethered aircraft using flight test data. It contributes to a better modeling of AWE systems which will allow better understanding of AWE capabilities, de-risk of the development process and fulfillment of the regulatory requirements. It also provides a complete state estimator for a tethered kite which is a requirement for developing a complete Flight Control System for an autonomous aircraft. To accomplish with these objectives, the following activities have been carried out:

- Design and implement an estimation algorithm which tacks the *Flight Path Reconstruction* (FPR) problem for a tethered wing. This algorithm provides the classical state variables of an aircraft (ie. Euler angles, position and velocity), and also the aerodynamic forces and torques, the kite angle of attack and angle of side slip, and the aerodynamic speed.

- Design a low cost and portable experimental setup based on commercial off-the-shelf components. This experimental setup provides the possibility to perform several flight campaigns with different commercial kites to gather experimental data to feed the FPR algorithm.

- Develop a flight testing methodology for power kites based on the designed experimental setup, and perform several flight campaigns.

- In an iterative process, the obtained experimental data has been used to validate an improve the proposed experimental setup, FPR algorithm, and flight testing methodology. Once the aerodynamic force and moment generated by the kites were reconstructed, a partial aerodynamic model of the kite was proposed.

The original results of the research activities carried out to fulfill these goals are described in the following chapters:

i **State-of-the-art of Flight Testing and Modeling of Tethered Wings (Chapter. 2).** A comprehensive revision of published works on flight dynamics, flight simulation, and flight testing of tethered wings is presented in this chapter. These works tackle the flight dynamics of tethered wings from the simple point-mass models to the most complex high fidelity models. Also, different approaches to flight testing of these systems are revised. However, opposite to this thesis work proposal, most of the published methods are based on ground sensing methods and provide only partial information about the kite aerodynamic behavior. Finally, a short revision of the aerospace industry solution to similar problems is also presented in this chapter, and the concept of *Estimation Before Modeling* (EBM) is introduced.

ii **Experimental Setup (Chapter. 3).** In this chapter a general overview of the experimental setup and its functional components are provided. A discussion of the criteria used to select each component is given and a comprehensive list of all the implied sensors and electronics is included.

iii **Flight Path Reconstruction (Chapter. 4).** A general overview of the geometry, reference frames and topology for four-line leading edge inflatable (LEI) kites and two-line rigid frame delta (RFD) kites are provided and the FPR algorithm is introduced. The chapter includes a comprehensive revision of the proposed measurement error models of each sensor. A detailed approach to the EKF algorithm implementation can be found in Appendix. A.

iv **Experimental Results (Chapter. 5).** The iterative approach used in this research activity for the flight testing of different power kites has been summarized in this chapter. Firstly, the results of a first *proof of concept* phase are presented and discussed. In this first phase, some of the hypothesis used to design the experimental setup are discarded, and some relevant findings on the kites behavior are incorporated into a final experimental setup design and testing procedures. Finally, some conclusions based on the definitive setup results are presented.

v **Conclusions and final Developments (Chapter. 6).** Final remarks on the ideas and results described in this thesis work are presented in this chapter, as well as proposals for future developments in this field.

2 STATE-OF-THE-ART OF FLIGHT TESTING AND MODELING OF TETHERED WINGS

This chapter provides a comprehensive review of different approaches to kite flight simulation and modeling. The technologies reviewed here include solutions to kites flight simulation, aerodynamic characterization, flight testing and performance assessment of AWEs. The chapter is organized in three different sections. Section 2.1 provides a review of recent works on AWEs flight simulators and modeling including, when available, the source of the used kite aerodynamic model. Section 2.2 provides a review of recent efforts on kite flight testing for model identification. Section. 2.3 presents an overview of similar efforts in the aerospace industry an introduces the *Estimation Before Modeling* approach.

2.1 Flight simulation of tethered wings.

The dynamics of a tethered aircraft is governed, as for any other aircraft, by the Newton's laws of motion. In an inertial reference frame, here named S_E, Newton's second law of motion states that the time derivatives of linear and angular momenta are equal to the externally applied forces and moments respectively,

$$\frac{d}{dt} \int_V \rho_a \frac{d\boldsymbol{r}'}{dt} \, dv = \int_V \rho_a \boldsymbol{g} \, dv + \int_S \boldsymbol{F} \, ds \tag{2.1}$$

$$\frac{d}{dt} \int_V \boldsymbol{r}' \times \rho_a \frac{d\boldsymbol{r}'}{dt} \, dv = \int_V \boldsymbol{r}' \times \rho_a \boldsymbol{g} \, dv + \int_S \boldsymbol{r}' \times \boldsymbol{F} \, ds \tag{2.2}$$

where $\int_V$ and $\int_S$ denotes volume and surface integrals for the entire aircraft, $\boldsymbol{r}'$ represents a vector pointing from the origin of the inertial frame to each differential of the aircraft, ρ_a represents the local mass density of the aircraft, $\boldsymbol{g}$ is the gravity vector expressed in the inertial frame, and $\boldsymbol{F}$ are the applied external forces per unit area.

The integrals in Eq. 2.1 and Eq. 2.2 can only be evaluated if the geometry of the aircraft is known. This is the case only for rigid aircraft, while for flexible ones (as in the case of textile kites), the geometry of the aircraft is the result of a balance between the structure response and the applied forces. If we define the aircraft mass as $m = \int_V \rho_a \, dv$, take $\frac{dm}{dt} = 0$, and treat the aircraft as a rigid body, $\boldsymbol{r}'$ is written as:

$$\boldsymbol{r}' = \boldsymbol{r}_P + \boldsymbol{r} \tag{2.3}$$

where $\boldsymbol{r}_P$ is a vector pointing from the origin of the inertial frame to the center of mass of the aircraft (P), and $\boldsymbol{r}$ is a vector pointing from P to each differential of the aircraft ($\boldsymbol{r}$ is constant when expressed in a frame linked to the aircraft that is called the body

axes S_B). The equations of motion then read

$$m\frac{dV_P}{dt} = m(\frac{\partial V_P}{\partial t} + \omega \times V_P) = mg + F \tag{2.4}$$

$$\bar{I}_P\frac{d\omega}{dt} = \bar{I}_P\frac{\partial\omega}{\partial t} + \omega \times \bar{I}_P\omega = M_P \tag{2.5}$$

where F and M_P are the external force and torque about the aircraft center of mass (P), and V_P, ω and $\bar{I}_{CG}$ are respectively the absolute velocity vector of P, the angular velocity vector of S_B with respect to S_E, and the inertia tensor of the aircraft with respect to P. Finally, three kinematic equations relate the times derivatives of the Euler angles, which define the orientation of S_B with respect to S_E, with the components of the angular velocity ,

$$p = \dot{\phi} - \dot{\psi}\sin\theta \tag{2.6}$$

$$q = \dot{\theta}\cos\phi + \dot{\psi}\cos\theta\sin\phi \tag{2.7}$$

$$r = \dot{\psi}\cos\theta\cos\phi - \dot{\theta}\sin\phi \tag{2.8}$$

where p, q and r are the three components of the angular velocity of the aircraft expressed in the body axes ($\omega = p\boldsymbol{i}_b + q\boldsymbol{j}_b + r\boldsymbol{k}_b$).

Equations 2.4 and 2.5 are only valid under the hypothesis of a rigid body, which may not be acceptable for some flexible kites. However, most of previous works on kites are based on this hypothesis, which limits their use to rigid or inflatable semi-rigid kites. There are some exceptions that incorporated kite flexibility effects on the model [101]. In this work, Williams et al. proposed a model with two flat plates articulated by a frictionless hinge, where each plate can reach a different attitude depending on its own dynamics and tether constraints.

In comparison with airplanes dynamic simulations, tethers introduce additional complexity to the model and represent one of the major differences among different simulation approaches. One finds approaches ranging from very simple models based on a massless, rigid, and inelastic tether [25] to more complex models that incorporate flexibility and elasticity effects [87]. Consequently, different kind of models have been proposed by the community in base of different approaches. The next sections review and classify them according to their complexity.

2.1.1 The point-mass model

In 2001, M. Diehl introduced a point-mass model for a tethered wing as a case of study of a *"nonlinear model predictive control"* methodology [25]. In this model, Diehl proposed a two lines kite model characterized by considering the kite a point with mass m, ignoring in consequence the rotational dynamic of the kite. Under this assumption,

equation 2.4 simplifies as

$$m\frac{d\boldsymbol{V}_{CG}}{dt} = m\boldsymbol{g} + \boldsymbol{F}_{aer} + \boldsymbol{F}_c \tag{2.9}$$

In Diehl's model, tether dynamics is neglected (massless tether), the kinematic constraints was imposed implicitly when using polar coordinates (constant tether length), and the tension force of the tether over the kite is modeled as a constraint force contribution ($\boldsymbol{F}_c$).

To model the aerodynamic force over the kite, a body frame was defined with its longitudinal axis $\boldsymbol{e}_l$ opposed to the aerodynamic speed, pointing from the leading edge to the trailing edge of the kite ($\boldsymbol{e}_l = -\frac{\boldsymbol{V}_{aer}}{\|\boldsymbol{V}_{aer}\|}$). A second axis with unit vector $\boldsymbol{e}_t$ was defined perpendicular to $\boldsymbol{e}_l$ and pointing from the left to the right wing tips. The frame was completed with the unit vector $\boldsymbol{e}_z$ normal to $\boldsymbol{e}_l$ and $\boldsymbol{e}_l$. The side-slip and attack angles of the kite are implicitly assumed to be zero in this definition. Under these hypothesis, lift and drag coefficients where modeled to be constant during the whole fight and a very simple aerodynamic model was derived,

$$\boldsymbol{F}_{aer} = \boldsymbol{L} + \boldsymbol{D} \tag{2.10}$$

$$\boldsymbol{D} = \frac{1}{2}\rho S\|\boldsymbol{V}_{aer}\|^2 C_D \boldsymbol{e}_l \tag{2.11}$$

$$\boldsymbol{L} = \frac{1}{2}\rho S\|\boldsymbol{V}_{aer}\|^2 C_l \boldsymbol{e}_l \times \boldsymbol{e}_t \tag{2.12}$$

where S, C_D and C_l are respectively the kite area, and the drag and lift coefficients.

Finally, after defining $\boldsymbol{i_r}$ as an unit vector in the radial direction (from the ground anchoring point to the kite), the author introduced the angle $\psi = \arcsin(\boldsymbol{e}_t \cdot \boldsymbol{i_r})$ as the control variable to completely define the kite orientation with respect to the inertial reference frame.

Some extensions to the point-mass model   The basic model introduced by Diehl in 2001 has been largely used and expanded in the following years. In 2006, B. Houska and M. Diehl published a couple of works related to it [48, 49]. In [48], a power kite tethered to a fixed point on the ground was modeled. A Lagrangian formulation was developed for the point-mass problem where the cable mass was not neglected and its kinetic and potential energies were written as

$$T_c = \int_0^1 \frac{1}{2}\rho_c A_Q r_0 \|s\dot{\boldsymbol{p}}\|^2 \, ds = \frac{1}{6}m_c\|\dot{\boldsymbol{p}}\|^2 \tag{2.13}$$

$$V_c = \frac{E A_Q}{2r_0}(r - r_0)^2 \tag{2.14}$$

$$A_Q = \frac{\pi}{4}d_c^2 \tag{2.15}$$

where ρ_c is the cable density, A_Q is the cross sectional area of the cable, $\boldsymbol{p} = r\boldsymbol{e}_r$ the kite position vector in polar coordinates and d_c and r_0 its diameter and nominal length.

In [49], the kite was tethered to a moving ship (constant velocity, inertial reference frame), introducing additional terms to the position and speed equations, while classic mechanics formulation was used. The tether dynamics was neglected, but its drag was introduced as an external force to the kite. The aerodynamic model used in 2006 is not largely different to the one used in 2001. The authors used a polar curve approximation for the drag coefficient C_D

$$C_D = C_{D_0} + kC_l{}^2 \tag{2.16}$$

while the lift coefficient, C_l, was treated as a control input to the system. Although the attitude dynamics of the kite was ignored, α was assumed to be influenced somehow through actuation over the bridle. A wind speed model as a function of height over the terrain was also introduced in this work.

In 2007, L. Fagiano et al. introduced another evolution of the point-mass model for different types of kite ground stations, considering both, the carousel and reel-in reel-out pumping approaches [17]. The carousel approach requires to derivate the equations for the rotatory ground station while the pumping approach requires to generalize the tether constraint as its length is not longer constant ($\dot{r} \neq 0$ in the polar notation). However, the kite is still considered massless and its attitude dynamics ignored. The tether force $\boldsymbol{F}_c$ was found from the operational characteristics of the electric machine ($\boldsymbol{F}_c$ is computed from a $\dot{r} = cte$ requirement).

Also in 2007, P. Williams et al. proposed a Lagrangian approach to the point-mass model to study both the case of the kite towing a free ground station, and the pumping approach with fixed ground station [102]. The tether was assumed to be rigid (there is not elastic contribution to the potential energy from the tether elongation), and the kite attitude was again assumed to be controllable by the angle of attack (α) and the kite bank angle with respect to the tether (ψ). Tether drag was considered into the generalized forces and the aerodynamic model used was similar to Diehl's 2006 model [48] with controllable C_l.

Introduction of the *"velocity angle of the wing"* In 2012, J.H. Baayen and W.J. Ockels [8] and M. Erhard and H. Strauch [30] explored even simpler dynamic models for controller design purposes. They are based on the assumption of a direct relation between a control variable and a kinematic state variable of the kite. In [8], the turning angle of the trajectory with respect to a horizontal vector in the local tangent plane is controlled using a single steering input, translating into a one- dimensional single-input, single-output tracking problem. Similarly, in [30], the yaw angle of the kite with respect to an axis parallel to the rigid tether, ψ, was directly related to the control variable δ by the simple law $\dot{\psi} = KV_{aer}\delta$. The kinematic state of the kite was found by ignoring inertial effects and assuming force equilibrium at every instant.

These assumptions were justified on data provided by both experimental and simulation results of the developed controller.

In 2014, L. Fagiano et al. published an approach for the control of tethered wings [33]. In this work a similar approach to [8] and [30] was used, and the following relation between a control variable and a kinematic variable of the kite was assumed

$$\dot{\gamma}(t) = K(t)\delta(t) \tag{2.17}$$

where the *"Velocity angle of the wing"* (γ) is defined as the angle between the local north (e_{LN}) and the wing's velocity vector(v), projected on the (L_N, L_E, L_D) local tangent plane [1]:

$$\gamma(t) = \arctan \frac{v \cdot e_{LE}}{v \cdot e_{LN}} \tag{2.18}$$

where e_{LE} is defined similarly to e_{LN} as an unit vector in the local tangent plane in the east direction.

In comparison to the experimental relationship proposed in [8] and [30], Fagiano et al. provided an analytic relationship of $K(t)$ in 2.17, with the main characteristics of the system (such as wing size, mass, and aerodynamic efficiency).

Lastly, in 2015, Erhard et al. [29] proposed again a point-mass model as a simple dynamic model for optimization purposes. However, the kite position within the wind window was found using a quaternion representation allowing for singularity-free equations of motion. The following model assumptions where introduced, (similarly to [30])

- Aerodynamic forces are large compared to masses, which lead the authors to ignore the inertia acceleration terms.

- The kite was assumed to fly always in its aerodynamic equilibrium state.

- The kite flies always with zero side slip angle and the aerodynamic force is contained within the symmetry plane of the kite.

- The kite is assumed to fly always at the same angle of attack.

- A variation on the steering control input to the kite translate into a proportional yaw angular rate.

In this work, the tether length was not a constant, and an additional constraint which relates the tether tension with the reel-in reel-out speed (which was considered a control variable) was introduced. Analogue to [30], a direct relation between a control variable

---

[1]L_N axis tangent to the wind window, pointing towards its zenith. L_D axis, called local down, pointing to the kite anchoring point (perpendicular to the tangent plane at wing's location) and L_E axis forms a right hand system and spans the tangent plane together with L_N

δ, and a kinematic variable of the kite (the bearing angle with respect to the local tangent plane north direction) was assumed. Authors concluded that under the assumed simplifications, the provided optimized control law runs on complete pumping cycles for several minutes. However further studies on AWEs performances should include extensions to the model to take into account discarded effects.

2.1.2 The rigid-body approach

In this approach, the kite is no longer treated as a point-mass, but as a 6 degree of freedom (6DOF) rigid body so that the attitude dynamics of the kite is not longer ignored. This leads to the equations of motion presented at the beginning of this chapter (Eq. 2.4 and 2.5). However, opposite to aircraft, the external forces applied over the kite must describe not only the gravitational, aerodynamic and propulsion (if applicable) forces, but also the tension(s) introduced by the tether(s), and its associated torque about the center of mass. Unlike simple point-mass approach, aerodynamics forces are modeled also as a function, among others, of the kite orientation with respect to the aerodynamic velocity of the kite, and usually expressed as an expansion on the so called aerodynamic derivatives.

A solution to the 6DOF rigid body problem was proposed by G. Sanchez-Arriaga et al. in a set of works [84, 83, 4, 85, 74, 87, 86]. In 2006 G. Sanchez developed a simple two dimensional kite model (only the dynamics of the kite in a vertical plane was considered) [84]. The system was composed of the kite, which was treated as a symmetric rigid body, the bridle, which is considered composed of rigid solid rods, and the tether, which is considered massless and drag-less. The major novelty introduced was the fact that, using Lagrangian formulation and under the previous assumptions, the work produced by the tension force of the tether is zero in any virtual displacement allowed by the kinematic constraints. This results into a simpler model in which the tension of the tether does not appear explicitly in the equations of motion of the kite. The kite was aerodynamically modeled as a flat plate using a linear expansion of the aerodynamic coefficients, which result on a force normal to the kite surface and dependent of the angle of attack of the kite.

This concept was expanded in 2014 by L. Salord et al. by introducing the lateral dynamics of the kite and non steady wind conditions [83]. In this work, the tether was still considered a constant length, massless rigid rod and its drag was neglected. The tether still produced no work in any constrained virtual displacement, thus removing the tension force in the Lagrangian formulation. However, a lateral aerodynamic force as a function of the side slip angle was introduced in the aerodynamic model of the kite.

In 2015 J. Alonso et al. developed an open-loop feedforward control scheme based on the simplified Lagrangian flight simulator which took advantage of the existence of periodic stable orbits to follow pre stablished trajectories [4]. The model presented

in [83], was extended with an inertia kite model with a semi-elliptical cross section, an aerodynamic model for the kite with drag along the longitudinal kite axis, and a external control law which provided time-dependent tether and bridle lines lengths.

In 2017 G. Sanchez-Arriaga et al. published a model for a two-line kite based on the analytical mechanic approach keeping the same advantages than in previous works [85]. In this model the kite is controlled by changing the relative lengths of both tethers. However, as a difference with previous point-mass models [33, 8, 30] where analytic laws relating the control variable and one kinematic state variable were a-priori hypothesized, the proposed model was self consistent as the evolution of the kite state vector is the result of the applied control variables, Newton laws and kinematic constraints.

Also, A. Pastor et al. progressively expanded the single line, two dimensions kite model presented in 2006 [84], to include tether flexibility and aerodynamic drag effects [74]. An evaluation of the gained accuracy of the model against the increased complexity was also performed.

Finally in 2018, G. Sanchez et al. developed previous mathematical models to the particular scenario of AWE systems based on drones flying with a single tether, both on fly or ground generating approaches [87]. In this model the drone is modeled as a rigid body, the tether is modeled as a set of inelastic segments to capture flexibility effects but neglecting elastic effects, and the aerodynamic model is constructed based on a set of aerodynamic derivatives incorporating the deflection of control surfaces. Nevertheless, control inputs to the tethers and the reel-in reel-out dynamics were rigorously incorporated to the model, as well as rotational effects of on-board turbines when available (fly-generation systems). Driven by the activities of this thesis work, G. Sanchez et al. developed the model for a four line surf-kite model[86]. In this model the kite, albeit an inflatable one, was modeled as a rigid body, while the front tethers were modeled as massless rigid rods and the control lines were modeled as a flexible set of individual inelastic rigid rods.

Alternativelly, in 2007, B. Houska et al. developed a 9 degree of freedom surf kite model [47]. In this model Houska proposed a mixture of a point-mass problem for the kite and a 6 degree of freedom for the tether model. This was justified based on the fact that the inertia of the kite was supposed to be much smaller than the tether's due to the relatively small mass of the kite in comparison with the tether and control pod masses. The used aerodynamic model was based on effective aerodynamic coefficients obtained by integration of the aerodynamic properties of all kite pieces resulting in the aerodynamic derivatives of the system. Nevertheless, deformation of the inflatable arc of the kite was considered as an additional state by the introduction of a second order differential equation. P. Williams et al. described the 6DOF rigid body approach by, in comparison to Houska [47], ignoring the tether dynamics and incorporating the inertia properties of the kite [103].

A comprehensive work on kite dynamics and modeling is presented by J. Breuckels in his thesis work [16]. Breuckels proposed a set of software tools for kite simulation in which both rigid body and multi-body approaches are explored together with different models for tethers, inflatable and foil kites. The 6DOF rigid body formulation is used here together with an aerodynamic model based on aerodynamic derivates, to analyze basic stability related behavior in base on the eigenmotions of kites in comparison with conventional aircraft.

2.1.3 High Fidelity Models

As stated at the beginning of this chapter, kites dynamic models based on the rigid body approach present major drawbacks on models fidelity as deformation of the kite is neglected. Indeed, the turning mechanism of kites is still a major debate point among the scientific community, and the kite flexibility effects can play an important role. In the very simple point-mass models this problem is obviated by an ad-hoc analytic relation between control input and kinematic response. In rigid body models the attitude dynamics of the kite is considered and the effects of control inputs over the kites are introduced by means of the tensions in the control tethers and the usual aerodynamic derivatives. However, even in rigid body models, a real insight into the turning mechanism of non rigid kites is not provided, as for flexible kites, deformation of the canopy under steering inputs is an integral part of the kite response. For this reason some authors have developed and insight into more sophisticated *"High Fidelity Models"*, referring to strategies such as multi-plate, lumped parameter or multi-body models.

Multi-plate models as the one introduced by Williams in [103, 101] substitute the deformable kite by a set of flat plates which can rotate freely one with respect to each other as a function of their own rotational dynamic and the given constraints of adjacent plates. Williams reduced the degrees of freedom between different plates to two by forcing all the plates to have the same yawing angle. However he still found the model highly nonlinear and complicated, specially when the number of plates is higher than two, resulting in great difficulties in finding equilibrium states for the system. Alternatively, lumped mass model discretized the kite as a set of masses connected by viscoelastic springs. These point masses are distributed all over the kite in a matrix scheme and simulate the structural behavior of the kite at a more basic level [34].

In his PhD thesis [16], J. Breukels developed a multi-body model using the commercial software MSC ADAMS. Multi-body models are an intermediate solution between rigid body and flexible kite models. In the later, numerical structural methods are used to calculate the shape of the kite under given loads, which in case of the aerodynamic forces, are calculated using computer fluid dynamic methods for every kite structure deformation (fluid-structure interaction). This complex interaction leads into costly and time consuming models which are difficult to implement and not suitable to be run on

a real time basis for control purposes. However, in a multi-body approach, the system is composed of several unitary rigid bodies. Each rigid body state is defined by a series of variables such us its position, orientation or inertia properties, and its dynamics is derived from the rigid-body equations of motion coupled with the constraints imposed by the adjacent bodies guaranteeing the complete system assembly consistence. J. Breukels developed a complete toolbox for ADAMS with all the necessary elementals to build a complete multi-body model of arc-shaped, inflatable kite system, including the canopy, the inflatable beams, and the tethers.

2.2 Flight testing and model validation of tethered wings.

Although many efforts have been made on kite modeling, simulation and control, empirical validation of the theoretical models is rare as flight campaigns have usually been focused on basic concept demonstration, control, and trajectory tracking rather than on systems performance assessment and model identification. This lack of empirical data is specially problematic when modeling non rigid, inflatable or ram-air kites. Inflatable kites as the ones described by J. Breukels [16] are built with an inflatable structure composed of a span-wise, arc-shaped leading edge, and a set of longitudinal struts to provide support for the kite canopy (Fig. 2.1). On the other hand, ram air kites (also called foil or closed cells kites) are composed of two layers of fabric which delimit the extrados and intrados of the wing. These wings have some air intakes in the leading edge so that, in flight conditions, pressure inside the kite builds up due to the aerodynamic speed of the kite and gives the shape to the airfoil. These kites does not have any kind of longitudinal or transversal supporting structure and the shape of the kite is guaranteed by the bridle when they are under tension (Fig. 2.2).

FIGURE 2.1: Inflatable SurfKite [35].

FIGURE 2.2: Ram-Air SurfKite [91].

The low weight of the fabric used in those types of kites, and the flexible nature of the designs (for example, canopy deformation is an essential part of the turning behavior of the kite) create a deep interrelation between the flow around the wing and the shape of the kite canopy. A change in the aerodynamic loads distribution immediately translate

into a change of the wing shape that generates a new flow around the wing.

Some efforts have been made on using wind tunnels to model and measure the aerodynamic-structural response of flexible kites. A. Wachter introduced a small ram air kite upside down in a large wind tunnel facility [98]. The underlaying idea of Wachter thesis was to use the wind tunnel not for direct forces measurement, but for kite shape identification by means of photogrammetry and laser scanning. This shape was used as a static boundary condition for a set of CFDs runs for different loads over the kite. A similar approach was used by J. Breuckels to validate his multi-body aerodynamic model.

Pure measurements of generated aerodynamic forces and torque on a kite in a wind tunnel results almost impossible. One of the major caveats of this approach is, as stated before, that flexible kites (even inflatable ones) relay on the bridle and tethers under tension to obtain its final shape. This requires to introduce complex experimental rigs into wind tunnels, which must be able to accommodate into their test section, not only the kite but a big enough section of the bridle and the tethers. Nevertheless, the classical solution for experimentation of big models in wind tunnels, which is Reynolds number conservation and geometrical similarity of down scaled models, is not feasible for big kites as the ones used in AWEs. This is due to the fact that, when testing rigid enough models to be considered rigid bodies, the structural properties of the model is not needed to be down scaled. However, in this kind of kites, because of the deep coupling between structural and aerodynamic response, this structural down scaling can not be neglected and structural similarity must be achieved by means of alternative materials which is hardly achievable. For these reasons, and the high cost of wind tunnels facilities, other attempts for kite flight testing have focused on "in the field" testing.

J. Breukels, beside developing the multi-body model, also provided and insight to some empirical validations[16]. Proposed models for inflatable beams were validated in laboratory by measuring its longitudinal and torsional stiffness. 3D shape of foil models were validated on wind tunnel by means of photometric measurements of the kite canopy under different kite attitudes. Also, the ADAMS tether model was validated by experimental measurement of waves propagation along the tether.

Some flight tests were also performed with commercial surf kites by Breukels [16]. These kites were flown in loops while the kite speed and generated tether tensions were measured. The proposed experiment consisted on a surf kite tethered to a human pilot on the ground. The kite was flown manually from the zenith of the flying window into a complete loop by a constant impulse on the control bar [2]. The instrumentation used by Breukels consisted on a GPS unit onboard the kite, one load cell in each tether (surf kites are flown on four lines, two front lines which hold most of the flying loads, and two rear control lines which are used to provide control inputs to the kite) and a weather station on the ground which provided wind speed every ten seconds. However nor the position of the kite, the tethering point or the control inputs (control bar position) were

---

[2]A further insight into surf kites control and general setup is developed in Chapter 4.1

measured. The onboard GPS was only used to obtain the kite absolute ground speed. Breukels did not provide any kind of data processing or filtering, but instead, raw sensors data was used for direct comparison with ADAMS model outputs. Since control bar position was not measured during flight tests, control inputs to the ADAMS model consisted on the measured control tethers tensions. Finally, measured absolute kite flying speed and front lines tethers tensions were compared with ADAMS simulation outputs and they were in an acceptable agreement between them.

Although Breukels provided some empirical validation of his model, a flight testing based approach for model identification was not provided. However, in his thesis work [44], De Groot proposed a method for reducing a multi-body dynamic model into a parametric rigid body model, and indirectly, a method for aerodynamic parameter identification. In particular, De Groot reduced the multi-body model for an arc shaped inflatable kite developed in ADAMS by Breukels, to a set of states describing the kite motion as a rigid body. The aerodynamics and structural deformations of the multi-body model were translated into quasi-static structural and parametric aerodynamic models. To obtain this parametric aerodynamic model, De Groot used a linear expansion of each coefficient into its aerodynamic derivatives, which were identified using a linear regression for each state. This identification was done over the aerodynamic forces and torque obtained by the ADAMS model instead of real in flight measures and was justified by De Groot due to the lack of empirical data. In this method, two assumptions were made,

- The aerodynamic forces and torque generated by the kite are known via empirical data (which is a strong assumption as they cannot be directly measured), or in this case via the ADAMS model.

- The underlying structure of the aerodynamic model is known, and each dimensionless coefficient C can be expanded in a Taylor series of the independent variables x_k for each time instant t_i and a regression error ε. This independent variables were chosen by De Groot based on his knowledge of the aerodynamic model underlaying the ADAMS model, and on experimental observations over different simulations.

$$C(t_i) = \sum_{k=1}^{r} a_k x_k(t_i) + \varepsilon(t_i) \tag{2.19}$$

In 2012, C. Jehle provided an experimental setup for model identification of the steering response of an arc-shaped inflatable kite to control lines inputs [55]. Jehle instrumented the kite with a commercial hybrid IMU/GPS unit attached to the central strut of the kite. This sensor tightly couples inertial measures (specific forces and angular rates) with GPS measures (position and velocity) via a Kalman filter to provide position, velocity and attitude of the kite. A pitot tube, situated among the front tethers and freely orientated into the airflow, was used to measure the aerodynamic speed of the kite. A wind sensor situated on a pole in the ground was used to measure wind speed

and potentiometers on the steering and power winches provided feedback of the control inputs to the kite. Jehle did not provide a complete aerodynamic model identification, but an empirical relation between the yaw angular rate and the control inputs of the kite. The identification of yaw rates instead of the yaw aerodynamic moment (usually characterized by the dimensionless coefficient C_N) was justified by Jehle as sensors did not provide angular accelerations of the kite, and numerical derivation from angular rates was ruled out. The method used by Jehle was similar to the one used by De Groot. He proposed a regression over a model proposed a-priori and parametrized by the yaw angular rate. The independent variables of this model were stated by Jehle empirically by observation of the empirical data and resulted in a model with the following structure,

$$r = c_1 \|V_{aer}\|^n P_s + c_2 \cos(\widehat{\boldsymbol{g}\boldsymbol{y}_k}) \tag{2.20}$$

where r is the yaw angular rate, $\|V_{aer}\|$ is the absolute aerodynamic speed, P_s is the steering control input, $\widehat{\boldsymbol{g}\boldsymbol{y}_k}$ denotes the angle between the gravity vector and the lateral $\boldsymbol{y}$ body axis, and n, c_1 and c_2 are coefficients to be identified.

Other attempts on kite modeling have explored towing the kite on a calm day at a constant speed to provide a well known apparent wind within the kite. In 2003 Stevenson [94] measured the generated lift and drag on a symmetric flight towed at a constant speed as a function of the control power setting (a relation between the control and main lines length). However, Stevenson found experimentally difficult to achieve precise measures on the kite efficiency due to the relation between the kite elevation measured through the lines angle and its efficiency. In 2005, Stevenson provided an alternative method consisting on flying the kite indoors on a circular pattern around the pilot [93].

In his thesis [97], R. van der Vlugt presented a similar approach to measure kite performance by flying the kite horizontally in the flying window (several runs in front of the pilot). The kite was instrumented with a GPS unit providing absolute speed of the kite, while load cells provided generated tensions, and an anemometer provided wind speed measurements. R. van der Vlugt found that for high lift to drag ratios, kite aerodynamic efficiency is approximately equal to the ratio between the kite velocity and true wind velocity.

Dadd [23] and D. Costa [21] provided additional approaches to kite flight tests based on towing rigs and J. Hummel started project TETA as part of his thesis work at TU Berlin [50]. Hummel's approach did not provide a complete solution for aerodynamic model identification as it focused on obtaining repeatable measurements of key aerodynamic characteristics of kites such as efficiency, lift and drag. This was achieved through a set of runs where the kite is stabilized in the flying window, and the generated aerodynamic forces and torque are inferred from the measured tensions on the tethers assuming static equilibrium. In this setup, the position of the kite is measured through the lines angle with respect to the towing vehicle. Control inputs to the kite are provided by a pilot through a sophisticated fly by wire system with haptic feedback.

Recently, E. Schmidt et al. proposed a State Estimator for a kite based on an Extended Kalman filter [88]. The propagation and measurement models of the filter are derived from the Lagrangian formulation of the point-mass problem with the following hypothesis,

- The aerodynamic forces are contained on the symmetry plane of the kite because the kite is assumed to be symmetric and flies with zero side slip angle.

- The direction of the drag force is determined by the direction of the kite aerodynamic velocity. However the lift force is contained in a plane perpendicular to the kite aerodynamic velocity, but its instantaneous direction is a priori unknown and estimated by the filter.

- A linear relation between the steering input (u), and the rotational speed of the lift force around the aerodynamic velocity vector (ω_l), is introduced. The constant gain (c_u) of this linear relation is considered a state variable and is estimated by the filter.

- The position of the kite is defined by the attitude angle of the tether and its length (the tether is considered a rigid rod).

Schmidt et al. performed a flight campaign with an experimental rig equipped with rotary encoders for tether attitude angles measurement, a load cell for measurement of the total tension generated by the kite, and an anemometer for wind speed measurement. The estimated results of the filter include the aerodynamic lift of the kite, the combined aerodynamic drag of the kite and the tether, the tether tension and the wind speed. Although the formulation of the problem is based on the point mass model, the effective angle of attack of the wing is calculated a-posteriori as a constant offset (α_0) of the mean cord of the kite with respect to the local tangent plane (this constant depends on the geometric characteristics of the kite bridle), plus an aerodynamic term involving the aerodynamic velocity of the kite,

$$\alpha = \alpha_0 + \arcsin\left(\frac{\boldsymbol{V}_{aer}}{\|\boldsymbol{V}_{aer}\|} \cdot \frac{\boldsymbol{r}}{\|\boldsymbol{r}\|}\right) \tag{2.21}$$

The experimental results were on concordance with the results obtained on simulations, except that the efficiency of the real kite was higher than the one of the simulator. A negative relation between the angle of attack and the efficiency of the kite, which was justified due to assumption that the kite was flying with angles of attack higher than the optimal, was also obtained.

G. Licitra et al. proposed an alternative method for system identification of the longitudinal aerodynamic model of an AWE system based on flight tests [60]. However, in this case the method is suitable only for a drone-like rigid wing controlled through aerodynamic surfaces and not through tethers inputs. Moreover, Licitra ignored the

dynamic interaction of the tether over the aircraft, and all the flight data was gathered in un-tethered flight tests (the drone flied un-tethered as a conventional aircraft). The proposed methodology is based on a Model-Based Parameter Estimation (MBPE) algorithm, where the longitudinal aerodynamic model of the aircraft is fitted to a conventional, no-linear, a-priori defined, model structure. An optimal control problem was formulated to fit the output of a dynamic model of the aircraft, which depends on the a-priori structure of the aerodynamic model, to the observed data over a set of flight tests. Although the method can provide some useful results for a particular set of AWE systems, it presents some important limitations. The method just estimated longitudinal aerodynamic parameters and ignored essential tether effects. It is basically the same used for untethered aircraft, which is a problem that has been largely studied by aerospace industry in the past.

In 2019, J. Oheler et al. published a study on aerodynamic characterization of soft kites using onboard measures of the kite aerodynamic velocity [72]. The efficiency and lift coefficient of an inflatable kite were estimated by using in-situ measurements. The experimental tests where performed with the Kitepower company AWEs prototype. Kitepower's design is based on a $25m^2$ inflatable kite, tethered to the ground by a single line, and controlled through a suspended pod (Kite Control Unit) which provides control inputs to the kite by varying the lengths of the lines of the bridle. As shown in previous works, an estimation of the wing efficiency of a kite can be achieved if the aerodynamic velocity of the kite is known. In this study, Oheler pointed out that the resulting precision of estimating the aerodynamic velocity of the kite by composition of the wind and kite velocity vectors (measured or estimated through a GPS or IMU unit) was not appropriate for reliable estimation of the aerodynamic characteristics of the kite. For this reason, an experimental rig consisting on a pitot tube and two wind vanes for side slip and attack angles measurement was developed. This rig was placed on the bridle over the KCU to avoid aerodynamic interference with the wing.

Oehler's approach is based on assuming quasi-static equilibrium of forces during the flight. The aerodynamic efficiency of the kite and its lift coefficient were found from the angle of attack of the kite, which is respectively computed from the "angle of attack of the tether" measured by a wind vane, and some corrections which take into account the deformation of the bridle due to gravitational force over the KCU and the de-power angle of the kite (related to the geometry of the bridle). The method did not provide a complete estimation of the lift coefficient, but only some general qualitative relations between the kite efficiency, the angle of attack and the flight phase (reel-in or reel-out). It was concluded that just the angle of attack is not enough to capture a full model for the kite lift and efficiency in cross-wind maneuvers.

2.3   Aerodynamic characterization of aircraft based on experimental flight data.

2.3.1   A short literature review.

Flight testing of AWEs has been largely focused on systems proof of concept and control reliability, more than on characterization of the flying devices except for some notable efforts. Even for the exceptions discussed above, the proposed methods are incomplete, as they are usually based on unrealistic a-priori hypothesis such as point-mass models where the attitude dynamic is ignored, symmetric flight with zero side slip angle or static-flight assuming massless systems. Previous works were focused on describing simple characteristics as the kite efficiency or lift coefficient, but they do not provide a solution for identification of a complete aerodynamic model of the aircraft, as in many cases the kite attitude or even lateral dynamics are not modeled.

On the other hand, flight testing and in particular aerodynamic characterization of aircraft based on flight data has been largely used and documented in the aerospace industry.

As it is happening now on AWE systems [94, 93, 97, 23, 21, 50, 72], first attempts on aircraft parameter identification in conventional aerospace industry were done using static maneuvers. The aerodynamic forces and torques were derived from the static equilibrium equations, and evolved through frequency-domain studies to dynamic maneuvers and transient state estimation [9]. The first attempt to apply state estimation to in flight recorded data was performed by O. Gerlach in the 1960's in TU Delft [39]. Gerlach used integrations on recorded angular rate from a pitch-rate gyroscope plus normal and longitudinal accelerometers to provide a post-flight estimation of the angle of attack, pitch angle and airspeed during dynamic maneuvers of the aircraft. He also introduced the concept of *"Flight Path Reconstruction"* to describe a-posteriori estimation of the estate variables of an aircraft during a dynamic maneuver. These estimated time histories of certain estate variables were used for parameter identification studies. In USA, the first attempts on *"Flight Path Reconstruction"* of an aircraft dynamic maneuver were documented in the early seventies in NASA, Calspan, and Sikorsky Aircraft Division [104, 105, 99, 69]. These first *"Flight Path Reconstruction"* techniques evolved to more sophisticated algorithms and Extended Kalman Filters were soon introduced as in [58, 45, 37]. The concept of *Estimation Before Modeling* (EBM) was also born. One of the most relevant technique for parameter identification in the aerospace industry is the *"maximum likelihood method"*. In this method, both the state variables and the aerodynamic parameters are identified at the same time by an optimization process. This is done by a formulation of the process model which implicitly includes the aerodynamic derivatives, requiring an a-priori knowledge of the aerodynamic model structure [68, 75]. This approach is similar for example to the one used by G. Licitra et al [60] or De Groot [44], as an a-priori model structure is always proposed in base of their knowledge of the problem or just direct empirical observation. However, when this model structure is not well known or at some point it is considered that needs to be changed, the whole algorithm must be re-written.

2.3.2 The Estimation Before Modeling technique.

The *Estimation Before Modeling* method is a two steps method, as opposed to the previously described methods. Two steps techniques (or estimation-before-modeling (EBM) [79, 46]) estimate first the time histories of the state variables of the system. Such time histories, which include the aerodynamic force and torque about the center of mass, are used in the second phase to perform the aerodynamic parameters identification of the system. Since the space state trajectory estimation, i.e the so called flight-path-reconstruction (FPR) [71], is independent of the proposed aerodynamic model structure, a-priori knowledge of the system is not longer needed, and different model structures can be tested afterwards without a reformulation of the problem. For this reason, the solution of the FPR problem is the first step towards the aerodynamic parameters identification for AWE systems using the EBM technique.

A typical EBM approach to aerodynamic parameter identification is shown in Figure. 2.3. In the estimation phase, given the process and measurement models of the system, a bayesian filter provides an estimation of the kite state vector ($\hat{x}$). Then, for each time instant of the reconstructed space-state trajectory, the reconstructed aerodynamic coefficients ($\hat{C}_{aer}$) can be expressed as a function of the reconstructed state vector ($\hat{x}$). Afterwards, in the modeling phase, an aerodynamic model structure as a function of the system state vector (x), the control inputs to the system ($u_{1 \cdots m}$) and a series of parameters ($k_1, k_2 \cdots k_n$) is proposed. An optimization process provides the optimal aerodynamic model parameters ($k_1, k_2 \cdots k_n$) that minimizes the error between the reconstructed aerodynamic coefficients and the proposed ones.
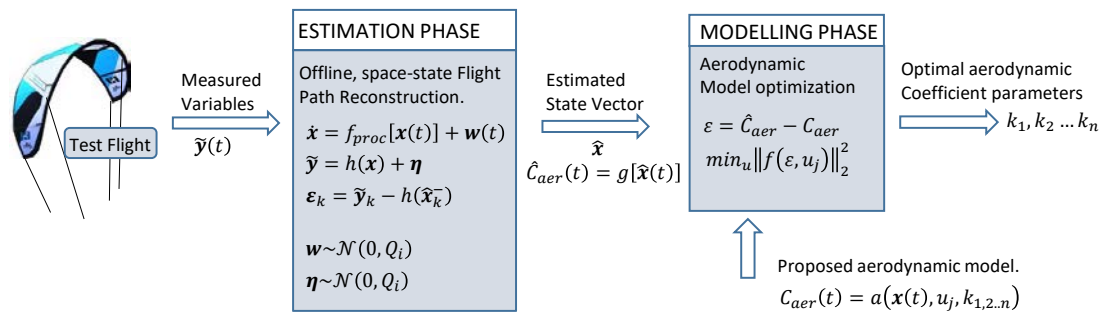
FIGURE 2.3: Estimation Before Modeling approach to kite flight testing.

The effectiveness of this approach to the modeling phase, largely depends on the ability to provide an aerodynamic model structure representative of the system aerodynamic behavior, which is usually achieved through a-priori knowledge of the aerodynamic characteristics of the aircraft. However, for the kite aerodynamic identification problem, the a-priori knowledge of the kite aerodynamic model structure may result a

challenging assumption due to the complex interactions of the kite aeroelastic characteristics and tethers contributions. Given the reconstructed flight path of an aircraft, A. Morelli proposed an aerodynamic parameters identification method, by using *multivariate orthogonal functions* which does not require any a-priori hypothesis on the structure of the aerodynamic model on the independent variables [70]. This method results of great interest for the modeling phase of the EBM technique of tethered wings as no a-priori knowledge of the system is required.

In a classical approach, the dependent variable y (the aerodynamic coefficient) is expressed as a linear expansion of the independent variables $\boldsymbol{x}_i$

$$y = a_1 \boldsymbol{x}_1 + a_2 \boldsymbol{x}_2 + \dots a_m \boldsymbol{x}_m + \boldsymbol{e} \tag{2.22}$$

$$\tag{2.23}$$

where

$$\boldsymbol{y} = [y_1, y_2, \dots y_N]^T \tag{2.24}$$

$$\boldsymbol{x_i} = \left[x_{i_1}, x_{i_2}, \dots x_{i_N} \right]^T \qquad i = 1, 2 \dots m \tag{2.25}$$

$$\boldsymbol{e} = [e_1, e_2, \dots e_N]^T \tag{2.26}$$

N is the number of samples, m is the number of independent variables of the proposed model and $\boldsymbol{e}$ denotes the modeling error vector. An estimation of the $a_1, a_2, \dots a_m$ parameters can be obtained by minimization of the least square function J

$$J = (\boldsymbol{y} - \bar{X}\boldsymbol{a})^T (\boldsymbol{y} - \bar{X}\boldsymbol{a}) \tag{2.27}$$

where

$$\bar{X} = [\boldsymbol{x}_1, \boldsymbol{x}_2, \dots \boldsymbol{x}_m] \tag{2.28}$$

$$\boldsymbol{a} = [a_1, a_2, \dots a_m]^T \tag{2.29}$$

If we denote the least-square estimation of $\boldsymbol{a}$ by $\hat{\boldsymbol{a}}$,

$$\hat{\boldsymbol{a}} = (\bar{X}^T \bar{X})^{-1} \bar{X}^T \boldsymbol{y} \tag{2.30}$$

However, in Morelli's approach, the m vectors of N samples of the independent variables $(\boldsymbol{x}_1, \boldsymbol{x}_2, \dots \boldsymbol{x}_m)$ are substituted by a set of k multivariate orthogonal functions $(\boldsymbol{p}_1, \boldsymbol{p}_2, \dots \boldsymbol{p}_k)$. Each $\boldsymbol{p}_j$ is an N-dimensional vector which in general depends on a set of the $\boldsymbol{x}_i$ independent variables so that $\boldsymbol{p}_j$ can be written as $\boldsymbol{p}_j = \boldsymbol{p}_j(\bar{X})$. The least-square function $\boldsymbol{J}$ reads

$$J = (\boldsymbol{y} - \bar{P}\boldsymbol{a})^T (\boldsymbol{y} - \bar{P}\boldsymbol{a}) \tag{2.31}$$

$$\bar{P} = [\boldsymbol{p}_1, \boldsymbol{p}_2, \dots \boldsymbol{p}_k] \tag{2.32}$$

where,

$$p_i^T \cdot p_j = 0, \qquad \forall i \neq j, \quad i, j \in [1, k] \qquad (2.33)$$

$$(2.34)$$

and,

$$\hat{a} = (\bar{P}^T \bar{P})^{-1} \bar{P}^T y \qquad (2.35)$$

It can be shown that matrix $\bar{P}^T \bar{P}$ is diagonal and the least-squares problem is decoupled, since each row in Eq. 2.35 can be solved independently

$$\hat{a}_j = \frac{p_j y}{p_j^T p_j} \qquad (2.36)$$

Consequently, the contribution of each orthogonal function to the reduction of the modeling error e is independent of the contribution to the error reduction by all the others independent orthogonal functions. As there are infinite combinations of the independent variables into multivariate orthogonal functions ($k = 1 \ldots \infty$), E. Morelli proposed a weighting method which quantitatively looked for an optimal combination of model accuracy versus model complexity.

J. Grauer et al [41] published in 2014 a study focused on identifying, if possible, a generic compact aerodynamic model structure which may suit different typologies of aircraft. Its main applications are on onboard *Flight Control Systems* for non-linear control, and to provide smooth analytical functions for control and optimization purposes. Complete tabulated aerodynamic models of eight different aircraft were reduced to eight parametric models using the *multivariate orthogonal functions* method. The more relevant terms of the aerodynamic model structure for each aircraft were retained and compared among the eight aircraft, finding an unified model structure which could suit any of them. The obtained accuracy for each aircraft was assessed by nonlinear flight simulations which demonstrated that *"the generic aerodynamic model produced accurate trim solutions, local dynamic behavior (modal frequencies and damping ratios), and global dynamic behavior under large-amplitude excitation"*.

In this thesis work, the *Estimation Before Modeling* approach is used to obtain a parametric aerodynamic model of a four-line LEI kite, which is representative of the ones used AWE system, and a two-line RFD kite.

3 Experimental Setup

An experimental setup aimed at the aerodynamic characterization of power kites with application to airborne wind energy generation systems has been designed, manufactured, and tested. A comprehensive set of onboard and ground sensors have been integrated and a flight testing procedure has been implemented, providing experimental flight data from different types of kites. This flight data was used on the *Flight Path Reconstruction* algorithm described in Chapter. 4.

The proposed experimental setup has evolved within the research activity, from a simpler *proof of concept* design, to the more complex, final iteration of the system. The first iteration of the system was based on the idea of developing an experimental setup as simple and low cost as possible. The limited budget of the GreenKite UC3M project [42], and the uncertainness of the handling qualities of a kite equipped with the selected onboard hardware, suggested a conservative approach for the first test flights. Consequently, only low cost hardware based on the PixHawk™open-hardware was firstly used onboard the kite. As discussed in Chapter. 5, after the first flights were completed and the obtained data analyzed, more expensive sensors were incorporated to the experimental setup. A scheme of the experimental setup architecture in its final configuration is presented in figure 3.1, while an insight into the first flight testing results is given in Chapter. 5 to justify the introduced modifications.
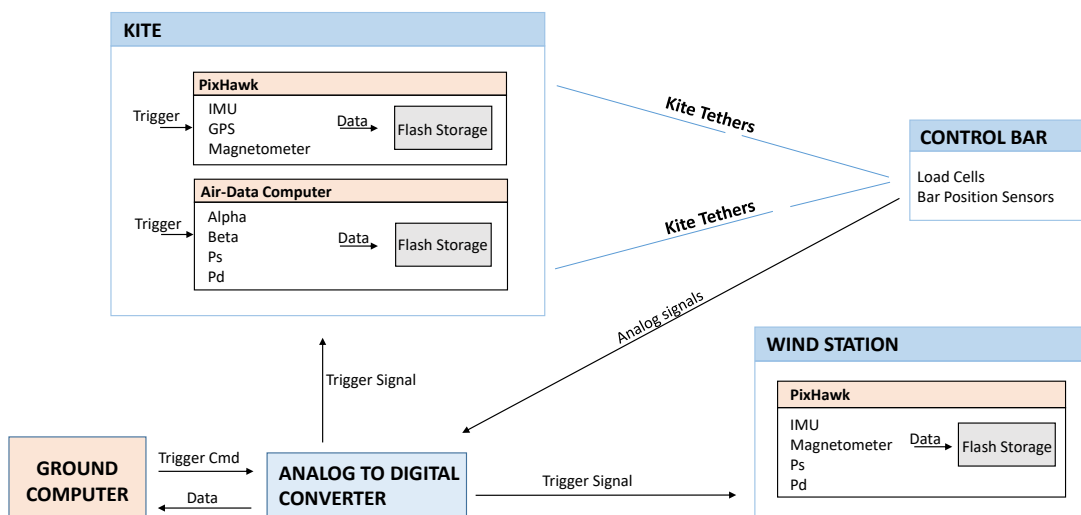

FIGURE 3.1: Scheme of the Experimental Setup in its final iteration.

In its final iteration, the experimental setup is composed of an instrumented textile kite, an instrumented control bar with two or four tethers and a ground wind station. The full setup was designed to be low-cost and easily portable and adaptable to different kinds of kites. The kite is manually controlled by a pilot on the ground by means of a *control bar*. Flight data is recorded synchronously onboard the kite, in the ground wind-station and in the ground computer. When possible, due to the UC3M kite-project limitations, *Commercial Off-The-Shelf* (COTS) components where chosen and adapted to the experimental rig requisites. However, some ad-hoc solutions were adopted for the control bar and the instruments supporting.

3.1 Kite Selection

When discussing Airborne Wind Energy generation systems based on power kites, large-scale kites flying hundreds of meters high are often considered. Those systems are being developed on the basis of flexible ram-air kites (KiteEnergy, Kite Power Solutions and SkySails), semi-rigid inflatable kites (KitePower), and tethered fixed-wing drones (Makani M600 or Ampyx Power solutions) [19]. The procedures described in this thesis work are focused on testing a tethered kite which could be representative of such a system, and although is based on small scale kites which can be easily operated under the UC3M Kite Project environment, it can be easily adapted to larger systems. However, as the proposed solution to the FPR problem assumes the rigid body hypothesis, the presented algorithm is more suitable for semi-rigid inflatable kites or tethered fixed-wing drones.

3.1.1 Leading Edge Inflatable (LEI), Semi-Rigid Kites

For the first iteration of the system, LEI kites were explored due to their larger lifting areas, great stability, and expected payload capability. For these reasons, a COTS 13 m^2 Cabrinha Contra™(Fig. 3.2) and a 10 m^2 Cabrinha Switchblade™(top panel of Fig. 3.11), inflatable surf-kites were chosen. LEI kites are built with an inflatable structure composed of a span-wise, arc-shaped leading edge, and a set of longitudinal struts to provide support for the kite canopy and are flown using four tethers, namely, two front tethers attached to the leading edge of the kite, and two control tethers attached to the trailing-edge tips. A detailed layout of these kites is presented in Chapter. 4.1. The selected kites have a supported leading edge (bridled leading-edge), concave trailing-edge and swept back wing. The bridled leading edge allows for a flatter and higher aspect ratio kite than those with unsupported ones, thus increasing the aerodynamic efficiency and projected lifting area of the kite. At the same time, the concave trailing edge and swept back angle in the wing, allows for greater lift control by increasing control bar induced pitch variations, while retaining acceptable forces on the bar by shifting the attaching point of control lines further back of the pressure center of the wing. These characteristics, in comparison with the so called C type unsupported leading edge kites, provide a wider flying envelope allowing a wide degree of variation in the measured variables, which are of great interest in terms of system parameter

identification and observability in this project.

FIGURE 3.2: Cabrinha Contra™13 m^2 kite during a flight test.

These two kites are flown on the same control bar and lines, and while being at a smaller scale, are still representative of the ones used in AWE systems. The techniques, tools, and hardware components developed in this work can be easily implemented with much larger kites (such as KitePower solution). From a practical point of view, two different sized kites were also chosen to have a wider flying envelope. Depending on wind speed, the kite size is selected to keep generated forces within the load sensors range and avoiding the need of switching to different scaled ones, while at the same time showing the portability of the experimental rig.

Table 4.1 shows the most important characteristics of the kites. They both have the same mass but there is a 30% difference in surface area. Compared to the larger kite, the smaller one is more rigid because it has two additional struts. Although each kite bridle are different, the control bar, tether lengths, and experimental setup used for both kites are identical. The mass and geometric characteristics of these kites are not provided by the manufacturer, but they were found via measurements in the laboratory [66, 73, 80]. However, as these kites are not completely rigid and present a complex 3D geometry, obtaining their geometry, mass distribution, and inertia tensors resulted in a challenging task with inherent modeling errors. In particular, 3D models of both kites had to be defined from the ground, and the mass distribution along the kites was estimated based on typical materials used in surf-kite manufacturing.

3.1.2 Rigid Framed Delta (RFD) Kite

After the first *proof of concept* test flights, in an effort to decrease the kite modeling error and also, due to the very high observed angle of attack of the LEI kites, the

experimental setup was adapted to be used with a faster RFD kite with a simpler 2D geometry. A COTS RFD kite (HQ Fazer XXL™, Fig. 3.3), with a span of 3.6 m was selected. The main criteria for the selection of this kite was the maximum payload that the kite could lift, as the weight of all the onboard sensors exceed the 0.6 kg (the kite empty mass is 1.27 kg). This payload does not represent a major inconvenient for the big inflatable surf-kites but it represents a concern for a typical *off the shelf* RFD kite. For this reason, the biggest available RFD kite in the market was selected.

This kite is a two-line kite, with a carbon fiber reinforced plastic rigid frame, and a delta shape. In this setup, opposite to four-line kites, both tethers are used to both support all the generated forces and to control the kite, and they are symmetrically attached at both sides of the central keel of the kite (Chapter. 4.1). As for the LEI kites, the geometrical characteristics of the kite are not provided by the kite manufacturer and they were obtained by direct measurement in the laboratory. In this case, the kite was modeled as a 2D body composed of a set of point masses, and each element of the kite structure was weighted and referenced to a reference frame linked to the kite, called the geometry axes[1]. The kite mass and the location of its center of gravity (CoG) could be modeled. These calculations have been experimentally validated in terms of the observed versus the calculated longitudinal position of the CoG and the total mass of the kite. The inertia tensor of the empty kite was calculated was calculated analytically by taking into account the position and masses of every element of the kite. The estimated characteristics of the Fazer XXL™RFD kite are provided in Table. 4.1 for its comparison with both Cabrinha™surf-kites.

FIGURE 3.3: HQ Fazer XXL™rigid kite during a flight test

---

[1]For this particular kite, the origin of the geometry axes was placed in the furthest point from the leading edge of the kite, over its central keel. The x_G axis points to the leading edge of the kite along its central keel and the y_G axis spans from the left to the right wing tips as seen from the intrados of the wing.

3.2 Control Bar

For all the tested power kites, kite control was achieved through changing the relative lengths of two lines. As described in Chapter. 4, the four-line LEI kites are controlled by changing the relative lengths of the rear control tethers, while the two-line RFD kite is controlled by changing the relative length of the two main supporting tethers. In both cases, this is achieved through the so called *kite control bar*, which the human pilot steers to asymmetrically elongate/shorten the control lines, or pull-push to symmetrically elongate/shorten the control lines (only for the 4-line kites).

During the first phase of the project, a COTS Cabrinha control bar was employed with both LEI surf-kites (Fig. 3.4). A scheme of the Cabrinha bar is found in Figure 3.5. In this bar, the front lines from the kite joint in the so called *front lines splitter* (F_v), from which most of the generated forces are transmitted to the ground attaching point by a single de-power rope of constant length L_s. The attaching point to the ground is achieved through a security fuse which can be manually opened so that the kite can be released if needed. Additionally, both control lines are routed to the tips of the bar which is steered, pushed and pulled by the pilot. This bar cannot be moved freely in the space but only around the central rope described before, which crosses the bar though a hole in its middle point. The push-pull movement of the bar is limited by the power stopper at a distance L_{cl} from the attaching point, and the de-power stopper at a distance L_{ds} to the F_v point.
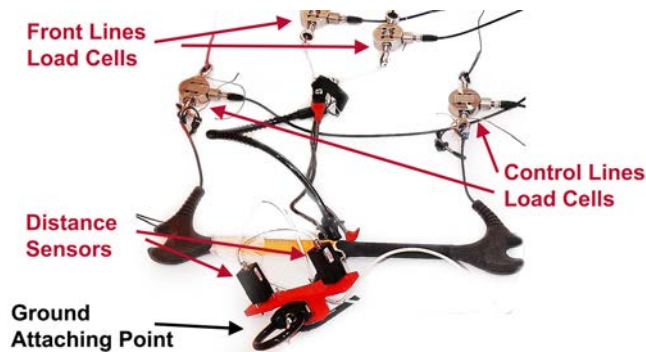
FIGURE 3.4: COTS Cabrinha control bar with load-cells and distance sensors installed.

Four load sensors were installed to measure the tether tensions at points $S_{c\pm}$ and $S_{l\pm}$ (the sensors at $S_{c\pm}$ are at distance s_0 from the tips of the control bar). As these load-cells were hanging from the kite, the tension transmitted to the kite because of their own weight (0.6 kg) was not being measured and incorporated to the FPR algorithm, thus representing an error source in the experimental rig. Additionally, a specifically designed and manufactured interface with two distance sensors was secured to the safety fuse of the control bar for the *proof of concept* test flights. Those sensors provided the distances $\tilde{d}_\pm$ between the tips of the interface, placed at distance w_{cl} from the tether

of length L_s, and points $S_{c\pm}$ (Fig. 3.5), and were required to calculate the relative position of the control bar during the flight. A detailed explanation of the involved trigonometric relations, and the control vector of the kite are provided in Chapter 4.1, while the in-flight obtained measures for the kite control vector and its relation with the kite behavior are discussed in chapter. 5. The numerical values of the characteristic lengths related to the experimental setup of the control bar can be found in Table. 3.1.
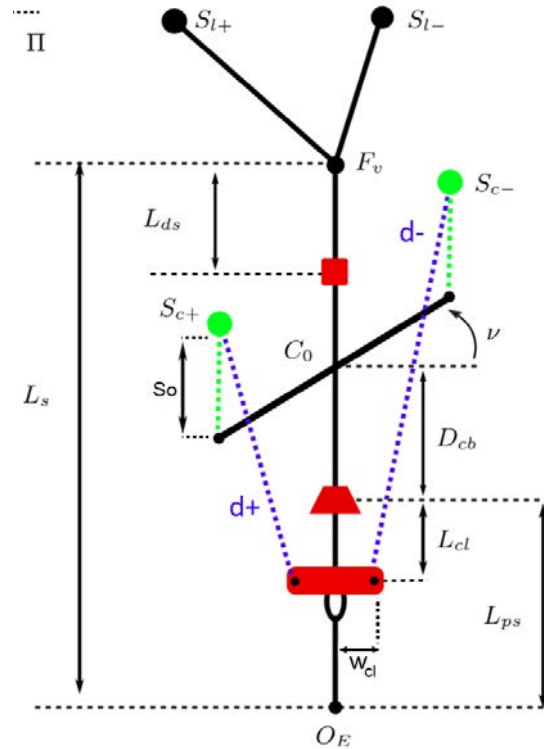
FIGURE 3.5: Control bar layout with load-cells and distance sensors

Symbol	Value	Symbol	Value
L_c	0.56 m	L_s	2.07m
L_{ds}	0.52m	L_{ps}	1.1 m
L_{cl}	0.1m	w_{cl}	0.07m
s_0	0.35m		

TABLE 3.1: Characteristic lengths related with the control bar

3.2.1 Ad-Hoc Control Bar

As described in Chapter. 5, in some phases of the flight, the tensions on the control lines were not enough to keep these lines straight because of the weight of the suspended

load-cells. This deformed the slacked lines creating an additional error in the FPR algorithm, which assumes straight tethers from the control bar to the kite attaching points (Chapter. 4.1). Finally, at some phases of the flight, it could even compromise the flying characteristics of the kite resulting in the kite stalling for a low wind speed situation (Chapter. 5.1.2). For these reasons, a new ad-hoc control bar was designed and built (Fig. 3.6).
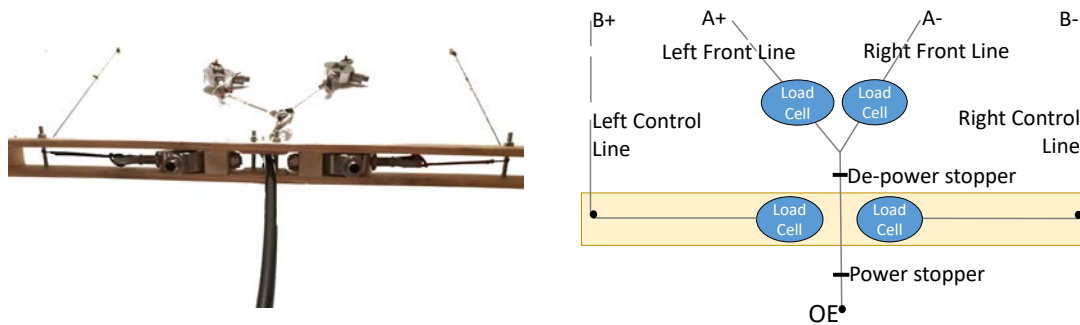
FIGURE 3.6: Ad-hoc control bar scheme for a four-line kite

For this new control bar, it was considered that retaining the load-cells inserted into the front lines was acceptable as the tensions produced during the flight in these main tethers were much bigger than the weight of the load-cells. Thus the front tethers stay straight and the flight characteristics of the kite are not affected. This hypothesis has been validated visually in flight and quantitatively by monitorization of the generated tensions (Fig. 5.2). However, as discussed before, inserting the load-cells into the control lines was not acceptable. For this reason, in the new control bar, the load cells were integrated in the structure of the bar and the tethers were guided by two small pulleys placed at the tips of the bar. The main advantage of this new control bar was that the weight of the load-cells is no longer supported by the rear control lines, but by the pilot who is hanging the control bar. At the same time, it allowed to re-use the ground attaching point (chicken loop in the surf-kites argot), the main de-power rope, power and de-power stoppers and front lines splitter (F_v) of the original Cabrinha control bar. Additionally, after the *proof of concept* phase, it was considered that the distance sensors for measuring the control bar position were not longer needed. For simplicity, these sensors were removed in the new control bar.

The new control bar can also be used with the RFD kite with minor modifications (See right panel of Fig. 3.7). For this kite, the control lines are also the main supporting lines, and were linked to the load-cells integrated into the control bar, while the front lines splitter was no longer used. When the control bar is used with this kite, the bar is always situated at the de-power stopper and all the flying forces are supported by the control lines. This resulted in the need to change the scale of the load-cells (Chapter. 3.4) integrated on the control bar, depending on if a 4-line LEI kite or a 2-line RFD

kite is being flown.
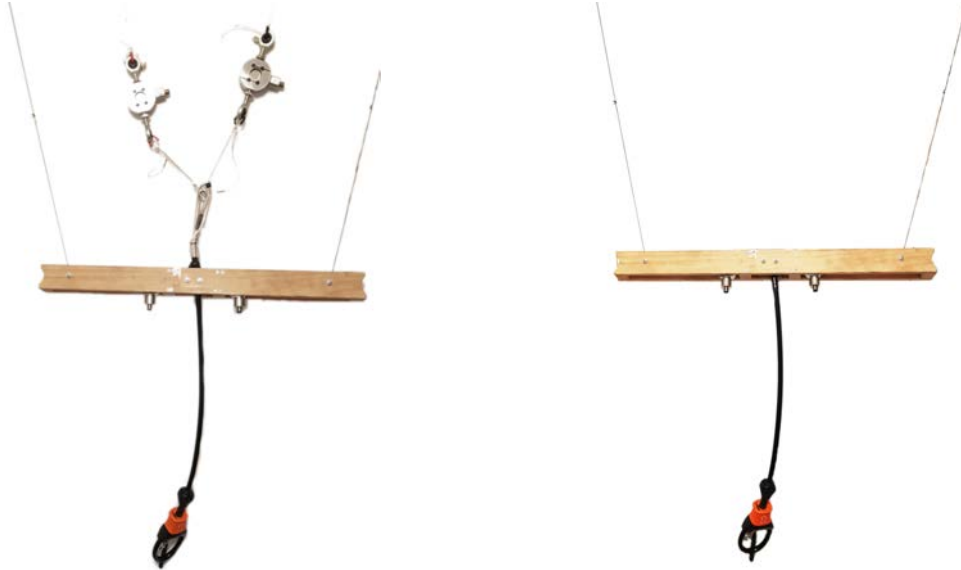
FIGURE 3.7: Ad-hoc control bar used with four-line (left panel) and two-line (right panel) kites.

Finally, in case of loss of control, COTS surf-kites' control bars are equipped with the described manual safety fuse that allows the rear lines to become completely slack, so the kite flags on the front lines with zero angle of attack and falls to the ground. In order to make this safety method compatible with the experimental setup, a fifth line linking the leading edge with the ground was added. This safety line is long enough to be completely slack during the flight, and its influence on the kite dynamics is negligible. The aerodynamic drag of the lines was ignored in our model.

3.3   Wind-Station

As described in Chapter 4, wind speed (V_w) and heading (ψ_w), are treated as system state variables. The kite aerodynamic velocity (V_a), can be then calculated a-posteriori, as a combination of the reconstructed state variables (kite ground speed (v), wind speed (V_w) and wind heading (ψ_w)), which are mapped to the kite and wind-station measurements through the EKF measurement model (Appendix A). However, in the first phase of the project, such a ground-wind station providing wind speed and heading measurements during the whole flight was not part of the experimental setup. We assumed that the wind velocity was constant during the flight and just a velocity measurement was taken before take off. After the analysis of the flight data of the first flights (Chapter. 5), a ground wind station was designed and manufactured to provide the FPR algorithm with instantaneous measurements of these two important variables (wind velocity and heading angle) (Fig. 3.8).

FIGURE 3.8: Ground Wind-Station

The ground wind station was designed [66] around an Inertial Measurement Unit (IMU), a pitot tube with total and static pressure transducers and a magnetometer sensor. It provides the FPR algorithm with measurements of the wind speed ($\tilde{V}_w$), wind yaw angular rate ($\tilde{r}$), and Earth magnetic field projected in a wind station body-axes [2] ($\tilde{\boldsymbol{B}}$). These sensors are similar to the ones used onboard the kite, and are mounted on a 3D printed rotating platform which is orientated to the wind by means of a wind vane, and installed on a rotatory bearing over a portable tripod.

3.4 Instrumentation

The flight testing instrumentation implemented in the experimental setup is split into three groups, namely the kite onboard instruments, the control bar instruments and the ground wind-station instruments. As described in Fig. 3.1, all the data measured by the three groups of instruments is synchronously recorded using a trigger signal generated by an *Analog to Digital Converter* (ADC), and is collected and analyzed after each flight test.

3.4.1 Onboard Instruments

Due to weight concerns for the onboard instruments and the project boundary conditions, a development of ad-hoc hardware for reading and logging the required sensors was discarded. Instead, COTS hardware was considered to provide measurements of the flight related variables of the kite. In particular, hardware used in the drone market was selected.

---

[2]A formal definition of the experimental setup layout and used reference frames are provided in Chapter. 4.

A ProfiCNC PixHawk2™ (Fig. 3.9) running Px4™ open source flight control software, was used for measuring and data logging of the following variables

- GPS position and velocity of the kite center of mass ($\tilde{\boldsymbol{r}}$, $\tilde{\boldsymbol{v}}$).

- Earth magnetic field vector ($\tilde{\boldsymbol{B}}$).

- Specific force ($\tilde{\boldsymbol{f}}_{IMU}$) and angular velocity ($\tilde{\boldsymbol{\omega}}$).

- Static and differential pressures ($\tilde{p}_0$, $\tilde{p}_d$).

PixHawk2™ is an all in one flight control hardware integrating a 32bits micro-controller, a GPS receiver, IMU, Magnetometer and Pressure sensors. The Px4™ flight control software provided a state estimation of the kite which was also recorded during the

first flight tests. This allowed to compare the estimation of some key state variables (such as kite attitude and ground trajectory) by both the FPR algorithm and the Px4™ estimator, in order to validate the obtained results (Fig. 5.4). Additionally, after the *proof of concept* test-flights, it was determined that for improving the accuracy of the FPR algorithm, direct measurements of the angle of attack (AoA) and angle of side-slip (AoS) of the kite were needed. Moreover, the aerodynamic speed measurements provided by the pressure sensors on the onboard Pix-Hawk™ resulted heavily biased and noisy (Fig. 5.3).

FIGURE 3.9: ProfiCNC PixHawk2 integrated Flight Control Hardware [76].

For this reason, an air data computer coupled with a multi-hole pitot tube manufactured by Aeroprobe™ (left panel of Fig. 3.10), was selected. This instrument provides the following data

- Angle of attack ($\tilde{\alpha}$).

- Angle of side-slip ($\tilde{\beta}$).

- Static and differential pressures ($\tilde{p}_0$, $\tilde{p}_d$).

The main criteria for selecting a multi-hole air data system was the minimum required dynamic pressure to provide accurate flow direction measurements. Alternative systems based on wind-vanes, require of a minimum dynamic pressure to drive the vanes. For example, Swiss Air-Data™ "Smart Miniature Vane SMV-1" (right panel of Fig. 3.10),

was advised by the manufacturer to require a minimum of $7\,\mathrm{m\,s^{-1}}$ wind speed for hysteresis free measurements and $10\,\mathrm{m\,s^{-1}}$ for full accuracy (*error* < 0.25 deg) which is well above the minimum $4\,\mathrm{m\,s^{-1}}$ wind speed required to fly the bigger kite. Additionally, the selected air-data-computer, provided a COTS, pre-calibrated, lightweight solution capable of triggered data-logging which adapted perfectly to the project requirements.

FIGURE 3.10: Aeroprobe uADC with Multihole Pitot (left panel) [1] and Swiss Air-Data Wind Vane (right panel) [2].

Aeroprobe uADCs are available with several dynamic pressure ranges. For kite flight tests, the 1 inH2O (249 Pa) range was selected (sensor characteristics for the selected range is shown in Table. 3.2). Pitot probes with serials 1190552-1 and 1190552-2 were installed in the tip of booms over the LEI and RFD kites leading edges, and specific calibration files for each probe were provided by Aeroprobe on 8/15/2019 and Mach = 0.03.

	Min.Calibrated Reading	Max.Calibrated Reading	Min. Resolution	Accuracy
TAS	$2.5\,\mathrm{m\,s^{-1}}$	$20\,\mathrm{m\,s^{-1}}$	$0.11\,\mathrm{m\,s^{-1}}$	$\pm 0.5\,\mathrm{m\,s^{-1}}$ ($TAS\,10\,\mathrm{m\,s^{-1}}$)
AoA	-20 deg	20 deg	0.1 deg	± 1 deg
AoS	-20 deg	20 deg	0.1 deg	± 1 deg

TABLE 3.2: Aeroprobe micro ADC data sheet.

Integration of the onboard instruments.

All the onboard instruments were powered by a $11.1V$ 3S Lithium-Polymer (LiPo) battery, while their positioning and orientation with respect to the kite frame was guaranteed by specifically designed 3D printed rigs. These plastic rigs were designed to align the PixHawk™ hardware to the kite body-axes described in Chapter. 4 and, therefore, all the onboard measured vector components are provided in kite body axes.

For the 4-line LEI kites, such interface allowed to safely attach the sensors to the kite central strut, just behind the leading edge (see left panel of Fig. 3.11). This location was chosen, due to the semi-rigid nature of the inflatable kite, as the only suitable attaching

point for the onboard sensors. As a result, the center of mass of the kite is shifted forward. Additionally, having a rigid union between the boom supporting the pitot tube and the kite is mandatory to guarantee the integrity of the air data measurements. Ideally, the boom and the kite should move as a rigid body. A 3D printed rig with exact the same shape of the central strut was designed and manufactured to attach the boom to the LEI kites [73, 80, 90]. This rig was secured to the strut by means of two adjustable straps. In addition, the boom was attached to the leading edge of the kite by using textile adhesive ribbons.

For the RFD kite, the correct orientation of the boom with respect to the kite was guaranteed by using a 3D-printed interface attached to the central spine of the kite, which is a very rigid carbon-fiber tube with a diameter equal to 1 cm. In this case, the location of the onboard instruments, as well as the length of the boom, were chosen with two main premises:

- Minimizing the aerodynamic interference of the wing over the pitot tube by placing the pitot tube as far as possible from the wing leading edge.

- Keeping the original position of the kite CoG in order to keep the original flying characteristics of the kite (aside from the increased inertia momentum and mass), which was not possible with the LEI kite.

To achieve these premises, the onboard instruments were installed in an ad-hoc 3D printed structure over the main spar intersection with the longitudinal keel of the kite (a detail of the RFD kite onboard instruments is given at the right panel of Fig. 3.11). This location was chosen as the furthest structural point from the kite leading edge where the supporting rig could be fixed. Once the location of the onboard instruments was fixed, the boom length was calculated to achieve the desired position on the kite CoG.
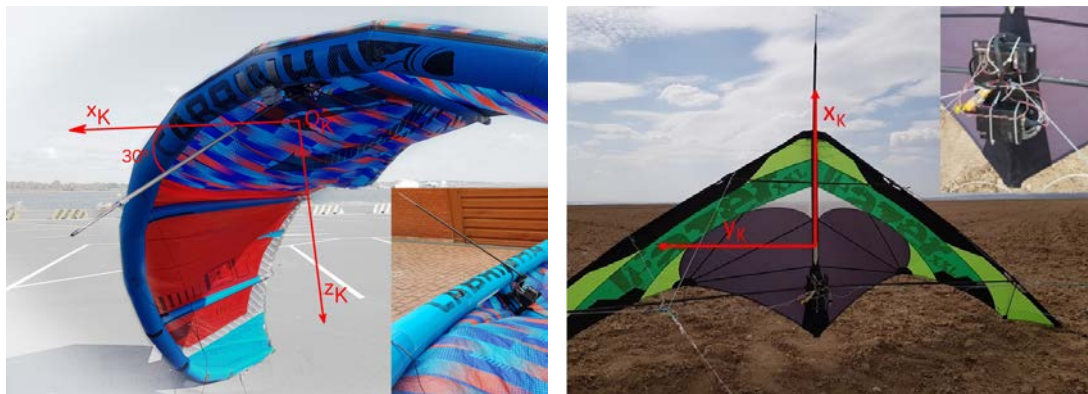

FIGURE 3.11: LEI (left) and RFD kites (rigth). The insets show a detail of the the onboard instruments.

For both types of kites, all the on-board instruments were included in the kite models as point masses. The new inertial properties of the kites (mass, center of mass location and tensor of inertia about the center of mass) were updated accordingly. Due to the experience obtained with the *proof of concept* test flights, the booms were mounted with a constant 30° offset with respect to the zero-lift axis of the kites. This axis is assumed to be located in the plane of symmetry of the kite and parallel to the selected x_K body-axis[3]. It is defined as the virtual line linking the kite's leading and trailing edges (Fig. 3.11). The 30° offset was selected in order to adapt the sensor range (±20°) to the expected AoA of the kite during the flight and avoid a saturation of the pitot tube. In the following, all the presented AoA measurements are corrected with the referred offset resulting in an effective AoA sensor range of 10° to 50°.

3.4.2 Control Bar Instruments

The selection of the load cells was based on the expected traction forces. A conservative calculation, based on a maximum aerodynamic lift coefficient ($C_L = 1.2$) and airspeed ($V_a = 7$ m/s), gives a lift force of around 460 N for the largest LEI kite. Since most of the load is supported by the front lines, two 50 kg (self-amplified, ±10 V analog output) TS-AMP load cells were selected for the front tethers. During flight tests, forces were consequently limited to 1000 N (roughly twice the expected stationary lift force) by manual control of the kite and real time supervision of the generated forces. For the rear tethers, two 10 kg TS-AMP were selected to measure control forces over the kite. When the ad-hoc control bar was used with the RFD kite, the smaller 10 kg TS-AMP load cells were removed from the control lines and substituted with the 50 kg ones, allowing to adapt the control bar to the 2-line kite.

To provide a fixed point O_E suitable to support these expected forces, the tether linking O_E with the front lines was hooked to a car on the ground. Additionally, two Posiwires WS31C 750 mm distance sensors were used in the first test flights to measure the $d_\pm$ distances, which allowed to reconstruct the control inputs to the kite.

The load cells and the distance sensors fed a National Instruments 6002 data acquisition system with eight, 16 bits, 50 kSamples/s analog inputs and two, 16bits, analog outputs. The data acquisition system was connected to a laptop running NI Signal Express Software through a USB interface. The amplified load cells and the distance sensors were powered by a 22.2 V LiPo rechargeable battery pack, while the NI 6002 was powered through the host computer USB port.

3.4.3 Ground Wind-Station Instruments

The ground wind station was built around a 3DR PixHawk1™ hardware. As for the onboard kite instruments, the PixHawk provides *off the shelf* measurements from an IMU and a magnetometer, plus static and dynamic pressures from a Pitot tube. The

---

[3]A formal definition of the selected reference frames is provided in Chapter. 4

PixHawk is powered from a 4.8 VNiMh battery pack placed also over the wind station platform.

3.5 Flight Testing Procedure

All the described measurements are logged during the flight and post-processed offline. As three different group of sensors (onboard the kite, in the control bar and in the wind station) with four different data logging devices (PixHawk™ and AeroProbe™ air-data computer onboard the kite, PixHawk™ on the wind-station and NI™ data acquisition system for the control bar) were used, a synchronization method was needed. For this purpose, a step/rise up trigger signal was generated at the beginning of the experiment by the analog output of the NI™ data acquisition system. This signal was fed from the NI output on the ground to the PixHawk™ *Analog to Digital Converter* (ADC) input in the kite, the Aeroprobe™ air-data computer trigger port, and to the PixHawk™ADC input in the wind-station.

Each measurement log generated by the PixHawk™, AeroProbe™ air-data computer and NI™ Signal Express software, are time stamped with its own time reference. The PixHawk™ data loggers were configured to automatically start recording upon the devices were powered up. The air-data computer was configured to start recording one second after the trigger signal rise up voltage. The NI™ Signal Express data recording was manually commanded. The recorded trigger signal is used offline to synchronize the experiment starting time for all the recorded logs, as the PixHawks™ and NI™ Signal express data logs are truncated to start one second after the trigger signal rise up, synchronized with the Air-Data Computer log starting point.

The procedure to perform a flight test was the following:

1. The ground computer is started and National Instrument data acquisition software (*NI Signal Express*) is initialized.

2. The National Instruments data acquisition system is powered on.

3. The trigger signal is configured to 0 (*low*) in *Signal Express* project.

4. The control bar load cells are powered on.

5. A functional test is performed to guarantee that the data acquisition system is working properly by manually applying tension over the control bar lines.

6. The trigger signal wires are connected to the analog input of the kite's PixHawk™.

7. The trigger signal wires are connected to the trigger port of the Aeroprobe™ air-data computer.

8. The trigger signal wires are connected to the analog input of the wind station's PixHawk™.

9. The kite's PixHawk™ and Aeroprobe™ airdata computer are powered on. At this point the kite's PixHawk™ starts recording data and the Aeroprobe™ is waiting for the trigger signal.

10. The wind station's PixHawk™ is powered on. At this moment the wind-station's PixHawk™ starts recording data.

11. GPS *fix* is indicated by both the kite and ground station GPS receivers.

12. NI Signal Express software is configured to start recording. At this moment, the load-cells and distance sensors of the control bar start being recorded.

13. The ADC trigger signal is configured to 1 (*high*) in *Signal Express* project. One second after this moment, the air-data computer starts recording data and will be considered the starting point for the experiment.

14. Trigger signal wires are removed from the kite and wind station.

15. The kite is launched and the flight is performed.

16. The kite is landed.

17. NI Signal Express software is commanded to stop recording data.

18. The Ground Wind Station is powered off.

19. A 2 minutes elapsed time is waited after landing to allow the air-data computer to empty it's internal buffer into it's flash storage.

20. The Kite's PixHawk™ and air-data computer are powered off.

21. The NI Signal Express log is saved and the ground computer can be turned off.

4 FLIGHT PATH RECONSTRUCTION

In this chapter, a solution to the so called Flight Path Reconstruction problem for a tethered aircraft is presented. The aim of the algorithm is to reconstruct, in a-posteriori basis, the space state trajectory of the tethered aircraft given the time histories of the measured physical magnitudes during the flight test. The output of the algorithm is the time history of the state variables of the system during the flight that better explains the observed noisy measures.

The presented methodology is based on a continuous-discrete extended Kalman filter (EKF). The state vector of the system is extended to include, aside from the kinematic variables of the kite, a complete description of the wind velocity vector, tether loads and the aerodynamic force and moment about the center of mass. This feature distinguishes it from other estimation solutions for kites and it is of great interest for future works on the aerodynamic characterization of kites based on EBM techniques. The core of the algorithm follows previous works on FPR for aircraft, where aerodynamic forces and moments were also part of the state vector and modeled as Gauss-Markov stochastic processes [46, 92, 40]. They have been adapted to consider the special characteristics of tethered aircraft and the proposed experimental setup, including wind data from a ground wind-station, airborne data, and tether loads. Additionally, the constraints introduced by control bar position and tethers lengths, together with stochastic error models for each sensor, have been respectively included into the measurement and process model of the filter.

The algorithm described in this section is the final iteration of the methods and experimental setup developed over this thesis work and has been formulated in base of the available measures obtained through the experimental setup described in Chapter. 3. This algorithm has been adapted to the particular scenario of four-line LEI and two-line RFD kites, resulting in different control bar configurations, kinematic constrains and measurement vectors for each kind of kite.

Before presenting the FPR algorithm, we introduce below some frame of references and notations that are essential for later discussions. Key hypotheses used in the FPR algorithm are also presented. Finally, an explicit formulation for the algorithm described here can be found in Appendix A particularized for both, four-line LEI, and two-line RFD kites.

Four-Line LEI kites use two front tethers and two control tethers for kite support and control. Conceptually, the front tethers span from an anchoring point on the ground (O_E) to two points $(A^{\pm})$ placed on the leading edge of the kite. The control lines connect point O_E with two points $(B^{\pm})$ on the wing tips at the trailing edge of the kite (Fig.

4.1). Such a simplified description takes into account that any characteristic length of the control bar is much smaller than the lengths of the tethers.

During the flight, most of the generated forces are supported by the front lines, which are considered to be always under tension and treated as constant length, massless rigid rods in the FPR algorithm. Under these circumstances, the two front tethers defines a plane Π which contains an isosceles triangle defined by the points O_E, A^+ and A^- (Fig. 4.4). If O_B is defined as the mid point of the imaginary line which spans $A^\pm$, $\overline{O_E O_B}$ constitutes the axis of symmetry of the isosceles triangle.

Control inputs to the kite are provided by the pilot by changing the relative lengths of the control lines. When both lengths are symmetrically shortened or elongated the whole kite changes its attitude and pivots around points $A^\pm$. When the control lines are asymmetrically elongated/shortened, the wing tips of the kite are deformed resulting in a change of the aerodynamic characteristics of the wing and the kite is steered.
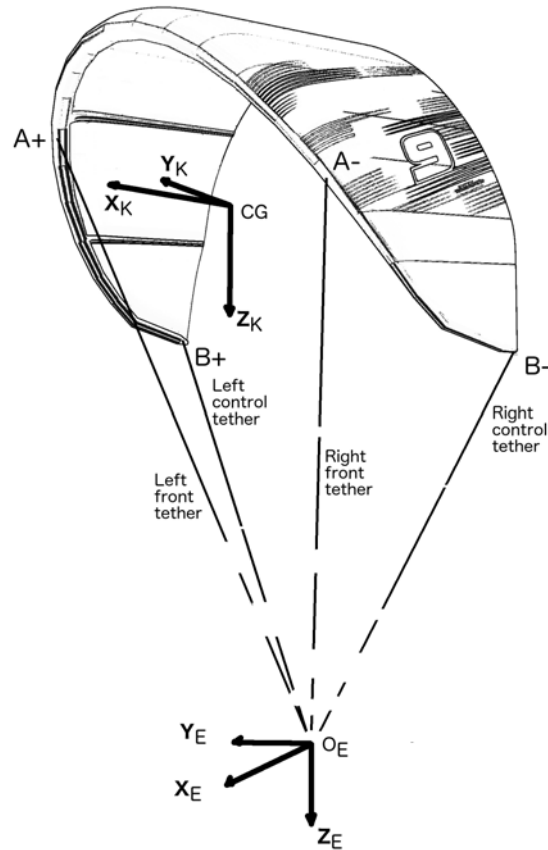
FIGURE 4.1: Four-Line LEI Kite

Two-Line RFD kites   relay on two tethers for both supporting the generated forces and providing control inputs to the kite. The two tethers span from the anchoring point in the ground O_E to two points, $A^\pm$ placed symmetrically with respect to the symmetry plane of the kite in the intrados of the wing (Fig. 4.2). Kite control is achieved by changing the relative lengths of both tethers, but opposite to four-line kites, this does not produces a deformation of the kite but a direct change in its attitude (bank angle). When the the left tether ($\overline{O_E A^+}$) is shortened with respect to the right one ($\overline{O_E A^-}$), a positive bank angle is induced. If the left tether is shortened, a negative bank angle is induced. Opposite to four-line kites, direct external control over the kite pitch angle is not feasible. For a 2-line kite, $\overline{O_E O_B}$ is not contained in the plane of symmetry of the kite in a generic flight state.

FIGURE 4.2: Two-Line RFD Kite

4.1 System Layout

For the *Flight Path Reconstruction* algorithm formulation, the hypothesis of *rigid body* is assumed. The position and orientation of the kite is completely defined by the position of its center of gravity (CoG) and the relative orientation of the kite's body axes with respect to an inertial reference frame. This approach results 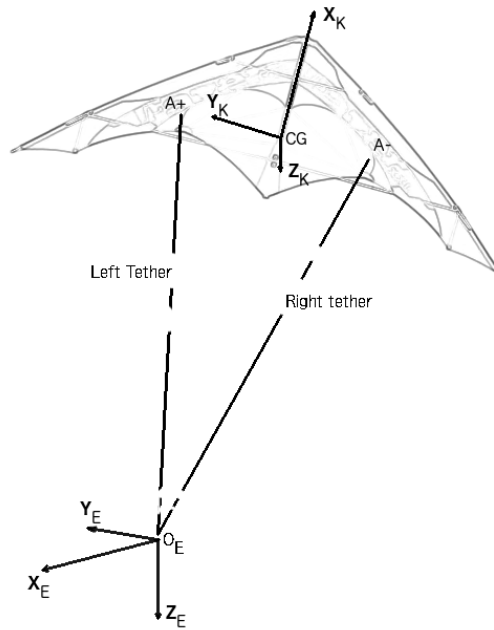in the six degrees of freedom (6DOF) problem described in Chapter. 2. In the following, reference frames are denoted generically as S_R. O_R stands for the origin of the reference frame, and $[x_R, y_R, z_R]$ stand for the unit vectors along the axes of the frame.

For both formulations of the FPR algorithm, an Earth fixed reference frame (S_E) is used. S_E is taken as an inertial reference frame, with origin (O_E) placed in the anchoring point of the kite to the ground. For the FPR formulation, flat Earth is assumed and S_E represents a NED (North, East, Down) reference frame. In the former, x_E and y_E point to the local geographic north and east respectively and z_E points downwards completing a right handed coordinate system. Additionally, two body fixed reference frames are defined

- A wind-station, body-axes (S_V), with origin (O_V) at the rotatory joint of the wind vane with the wind station tripod (a description of the wind station is provided in Chapter. 3). In the former, x_V points to the pitot tube of the vane, z_V is parallel to z_E and y_V defines a right handed coordinate frame (Fig. 4.3).

FIGURE 4.3: Wind-Station body axis.

- A kite body-axes (S_K), with origin (O_K) in the center of mass of the kite, and unit vectors x_K, y_K and z_K. Vector y_K spans from the left to the right wing tips, while x_K and z_K are placed in the plane of symmetry of the kite. Vector x_K points forward along an imaginary line linking the leading and trailing edge of the kite, and z_K completes a right handed coordinate frame (Figs. 4.1 and 4.2).

The particular control scheme and lines layout of the selected COTS LEI and RFD kites (see Chapter. 3) are modeled as following:

The layout of the four-line, LEI Cabrinha™ kite is shown in Fig. 4.4. The control bar is modeled as a rigid rod of length L_{cb}. Each of its tips is attached to a control tether of length L_t (from the control bar tips to $B^{\pm}$ respectively). As described in 3.2, this control bar can not be moved freely in the space, but only through the *de-power rope* of length L_s, which pass trough a hole in the middle point of the control bar C_o, and joins the anchoring point on the ground O_E with both frontal tethers. The point where the *de-power rope* joins with both frontal tethers is denoted as F_v, and the length of each frontal tether (from F_v to $A^{\pm}$) is L_l. For simplicity, it is assumed that during the whole flight, the pilot keeps the control bar within the plane Π. Finally, the longitudinal displacement of the control bar is limited by the described *power and de-power stoppers*.

When the control bar is placed at the *stopper* closer to O_E (the *power stopper*), the relative length of the control lines is the shortest possible and the kite is pivoted around $A^{\pm}$ with a positive pitch, thus increasing the angle of attack and powering the kite. However, when the control bar is placed at the *stopper* further from O_E (the *de-power stopper*), the relative length of the control lines is the longest possible and pitch angle is reduced. The kite would then be de-powered. The kite can also be steered by moving the control bar asymmetrically, i.e. pivoting the control bar an angle v around point C_0

in Fig. 4.4. When the control bar is steered to the left ($\nu > 0$) the relative length of the right control line is increased and the left control line is decreased. From the point of view of the pilot, the kite would turn to the left. A deflection of the control bar in the opposite direction ($\nu < 0$) makes the kite turns to the right.
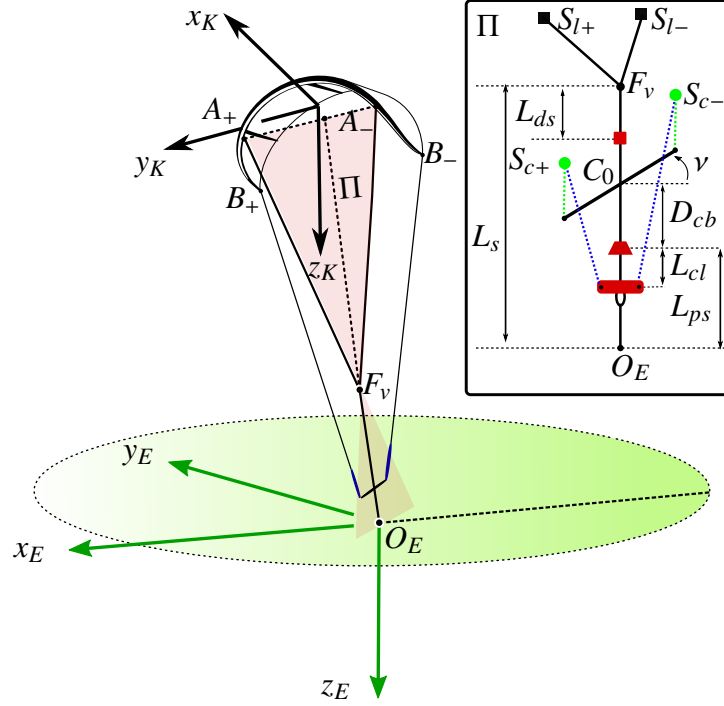
FIGURE 4.4: Four lines kite. Scheme of the experimental setup.

Control inputs to the kite are included in our model by using two time-dependent variables: ν and u_p. The former, already explained in the previous paragraph, is the angle between the control bar and the line defined by points O_E and F_ν. The latter is a dimensionless length related to the distance between the control bar and the de-power rope according to the formula [50]

$$u_p = 1 - \frac{D_{cb}}{L_s - L_{ps} - L_{ds}} \tag{4.1}$$

It takes values equal to zero and one when the kite is fully depowered (bar at the *de-power stopper*) and powered (bar at the *power stopper*).

Since $| \overline{C_0 O_K} | >> | \overline{A_\pm B_\pm} |$, we assume that the rear control lines practically belong to Π and they are parallel to the tether of length L_s. Under such assumptions, the following trigonometric relations hold

$$\tilde{d}_\pm^2 \approx \left(L_{cl} + D_{cb} \mp \frac{L_c}{2} \sin \nu + s_0 \right)^2 + \left(\frac{L_c}{2} \cos \nu - w_{cl} \right)^2 \tag{4.2}$$

These constraints and Eq. (4.1) give the power ratio u_p (or the control bar distance D_{cb}) and the bar deflection ν as a function of the measured distances $\tilde{d}_+$ and $\tilde{d}_-$

The layout of the HQ™ RFD kite is similar to the one used for the four-line kite. However, this kite only has two tethers to both anchor and control the kite. As stated before, in this case the control bar does not have the possibility to be moved along the de-power rope (between the de-power and power-stoppers) to control the pitch of the kite. Instead the bar is constantly situated at the de-power stopper ($u_p = 0$). It is assumed again that the bar can only be steered inside the plane Π defined by the points O_E and $A^\pm$. The control bar changes the relative length of the right and left tethers and allows the pilot to steer the kite.

For both types of kites, the mass of the kite is denoted as m_K and, due to the kite symmetry, $I_{xy} = 0$, $I_{yz} = 0$. Additionally, the RFD kite is assumed to be flat and we can then set $I_{xz} = 0$. The S_K-component of the tensor of inertia of the kite about its center of mass reads,

$$\bar{I}_{O_K} = \begin{pmatrix} I_x & 0 & I_{xz} \\ 0 & I_y & 0 \\ I_{xz} & 0 & I_z \end{pmatrix}_{LEI} \qquad \bar{I}_{O_K} = \begin{pmatrix} I_x & 0 & 0 \\ 0 & I_y & 0 \\ 0 & 0 & I_z \end{pmatrix}_{RFD} \qquad (4.3)$$

The main characteristics of the kites selected for the experimental setup are shown in Table. 4.1, including the coordinates of the tether attaching points in the kite body-axes and the tethers lengths. A comprehensive review of the control bar characteristic lengths are given in Table. 3.1

	Cabrinha Switchblade	**Cabrinha Contra**	**HQ Fazer XXL**
Mass	3.4 kg	3.4 kg	2 kg
I_x	8.68 kg m^2	12.33 kg m^2	0.72 kg m^2
I_y	2.43 kg m^2	3.18 kg m^2	0.09 kg m^2
I_z	8.40 kg m^2	11.41 kg m^2	0.81 kg m^2
I_{xz}	0.33 kg m^2	0.43 kg m^2	0 kg m^2
Surface	10 m^2	13 m^2	1.86 m^2
Span	4.3 m	5 m	3.6 m
Struts	5	3	–
$X_{A\pm}$	0.42 m	0.53 m	0 m
$Y_{A\pm}$	±1.05 m	±1.40 m	±0.67 m
$Z_{A\pm}$	−0.20 m	−0.31 m	0 m
$X_{B\pm}$	−0.97 m	−0.98 m	–
$Y_{B\pm}$	±2.15 m	±2.50 m	–
$Z_{B\pm}$	1.38 m	1.60 m	–
L_l	23.85 m	24.37 m	39.28 m
L_t	23.19 m	23.45 m	–

TABLE 4.1: Kite parameters including all the on-board equipment, referenced to the kite body frame.

4.2 EKF process model

The process model of the filter is written in the compact form

$$\frac{d\boldsymbol{x}(t)}{dt} = \boldsymbol{f}_{proc}\left[\boldsymbol{x}(t)\right] + \bar{\boldsymbol{G}}\boldsymbol{w}(t) \tag{4.4}$$

with $\boldsymbol{x}$ representing the state vector and $\boldsymbol{w}$ the process noise, which is modeled from a multi-variable normal distribution function with zero mean and covariance $\bar{\boldsymbol{Q}}$. Explicit equations for the flow $\boldsymbol{f}_{proc}$ and the constant matrix $\bar{\boldsymbol{G}}$ are given in Appendix A.

The state vector of the filter,

$$\boldsymbol{x} = [\boldsymbol{x}_k \ \boldsymbol{x}_{bias} \ \chi_1 \ \chi_2 \ \chi_3] \tag{4.5}$$

appearing in Eq. (4.4) includes:

i The *kite state vector*

$$\boldsymbol{x}_k = [\boldsymbol{r} \ \boldsymbol{v} \ \Upsilon \ \boldsymbol{\omega}] \tag{4.6}$$

includes the S_E-components of the position vector of the kite ($\boldsymbol{r}$), the S_K-components of the absolute velocity ($\boldsymbol{v}$) and angular velocity of the kite ($\boldsymbol{\omega}$), and its roll, pitch,

and yaw angles (Υ):

$$r = \overline{O_E O_K} = x_E \mathbf{i}_E + y_E \mathbf{j}_E + z_E \mathbf{k}_E \tag{4.7}$$

$$v = d\mathbf{r}/dt = u\mathbf{i}_K + v\mathbf{j}_K + w\mathbf{k}_K \tag{4.8}$$

$$\omega = p\mathbf{i}_K + q\mathbf{j}_K + r\mathbf{k}_K \tag{4.9}$$

$$\Upsilon = [\phi \ \theta \ \psi] \tag{4.10}$$

ii A *bias state vector*, $\mathbf{x}_{bias} = \begin{bmatrix} \Theta_B & \Theta_{B_V} & \Theta_f & \Theta_\omega & \Theta_{V_w} & \Theta_{r_V} \end{bmatrix}$, that contains the error biases for the on board the kite measured magnetic field ($\tilde{\mathbf{B}}$), specific force ($\tilde{\mathbf{f}}$) and angular velocity ($\tilde{\omega}$), plus the biases for the wind-station measured magnetic field ($\tilde{\mathbf{B}}_V$), wind speed ($\tilde{V}_w$) and yaw angular rate ($\tilde{r}_V$).

iii A set of three *pseudo states vectors* stochastically described using third-order Markov Models:

- $\chi_i = \begin{bmatrix} \mathbf{F}_{a_i} & \mathbf{M}_{a_i} & T_{A^+_i} & T_{A^-_i} & T_{B^+_i} & T_{B^-_i} & V_{w_i} & \psi_{w_i} \end{bmatrix}_{i=1,2,3}$ for the four lines, inflatable kite setup.

- $\chi_i = \begin{bmatrix} \mathbf{F}_{a_i} & \mathbf{M}_{a_i} & T_{A^+_i} & T_{A^-_i} & V_{w_i} & \psi_{w_i} \end{bmatrix}_{i=1,2,3}$ for the two lines, acrobatic kite setup.

The first vector, χ_1, contains the S_K-components of the aerodynamic force and moment about the kite center of mass ($\mathbf{F}_{a1}$ and $\mathbf{M}_{a1}$), the magnitudes of the tether tensions $T_{A^\pm 1}$ (and $T_{B^\pm 1}$), the magnitude of the wind velocity V_{w1} and its heading angle ψ_{w1}. The process equations of this vector and the ones for χ_2 and χ_3 yield a three-term quadratic interpolation as a function of time, whose coefficients are updated by the filter at each sampling instant.

The wind heading angle (ψ_{w1}) is related with the S_E to S_V rotation angle (ψ_V) as:

$$\psi_V = \psi_{w1} + \pi \tag{4.11}$$

Finally, the dimensions of the kite state vector $\mathbf{x}_k$, bias state vector $\mathbf{x}_{bias}$, and each Markov vector χ_i are equal to 12, 14, and 12 (10), respectively. Therefore, the dimension of the total state vector of the filter $\mathbf{x}$ is $N_F = 62$ for the 4-lines kite and $N_F = 56$ for the 2-lines kite.

4.3 EKF observation model

After denoting with symbol $\sim$ the magnitudes measured by the sensors (see Chapter. 3), the measurement model of the filter is,

$$\tilde{\mathbf{y}} = \mathbf{h}(\mathbf{x}) + \boldsymbol{\eta} \tag{4.12}$$

with $\tilde{\boldsymbol{y}}$ representing the observation vector, $\boldsymbol{h}(\boldsymbol{x})$ the observation model that maps the true state space into the observed space, and $\boldsymbol{\eta}$ the observation noise which is assumed to be zero mean Gaussian white noise with covariance $\bar{\boldsymbol{R}}$.

The observation vector of the 4-line kites,

$$\tilde{\boldsymbol{y}} = \left[\tilde{\boldsymbol{B}} \ \ \tilde{\boldsymbol{v}} \ \ \tilde{\boldsymbol{r}} \ \ \tilde{\boldsymbol{f}} \ \ \tilde{\boldsymbol{\omega}} \ \ \tilde{v}_a \ \ \tilde{\alpha} \ \ \tilde{\beta} \ \ \tilde{T}_{A^+} \ \ \tilde{T}_{A^-} \ \ \tilde{T}_{B^+} \ \ \tilde{T}_{B^-} \ \ \tilde{\boldsymbol{B}}_V \ \ \tilde{r}_V \ \ \tilde{V}_w \ \ \tilde{D} \ \ \tilde{P}_{y_k}\right]' \qquad (4.13)$$

includes the S_K-components of the Earth magnetic field measured by the onboard magnetometer ($\tilde{\boldsymbol{B}}$), the S_E-components of the velocity and position vectors of the kite measured by the onboard GPS ($\tilde{\boldsymbol{v}}$ and $\tilde{\boldsymbol{r}}$), the S_K-components of the specific force and angular velocity measured by the IMU ($\tilde{\boldsymbol{f}}$, $\tilde{\boldsymbol{\omega}}$), the magnitude of the kite true airspeed, the angle of attack and the angle of side slip measured by the onboard air-data computer ($\tilde{v}_a$, $\tilde{\alpha}$ and $\tilde{\beta}$), the four magnitudes of the measured tether forces ($\tilde{T}_{A^\pm}$ and $\tilde{T}_{B^\pm}$), the S_V-components of the Earth magnetic field ($\tilde{\boldsymbol{B}}_V$) measured at the wind station, the wind yaw angular rate ($\tilde{r}_V$) and the wind airspeed magnitude ($\tilde{V}_w$).

Aside from the measurements provided by the onboard and ground sensors, two constant *virtual* measures are derived from the particular layout of the system. The constant distance from the kite anchoring point on the ground O_E to the CoG of the kite ($\tilde{D}$), and the null projection ($\tilde{P}_{yb}$) of the vector $\overline{O_E O_B}$ over $\boldsymbol{y}_k$.

The observation vector of the 2-line kite,

$$\tilde{\boldsymbol{y}} = \left[\tilde{\boldsymbol{B}} \ \ \tilde{\boldsymbol{v}} \ \ \tilde{\boldsymbol{r}} \ \ \tilde{\boldsymbol{f}} \ \ \tilde{\boldsymbol{\omega}} \ \ \tilde{v}_{aer} \ \ \tilde{\alpha} \ \ \tilde{\beta} \ \ \tilde{T}_{A^+} \ \ \tilde{T}_{A^-} \ \ \tilde{\boldsymbol{B}}_{wind} \ \ \tilde{r}_{wind} \ \ \tilde{V}_{wind} \ \ \tilde{D}\right]' \qquad (4.14)$$

includes the same variables than the one of the 4-line kite setup, albeit the $\tilde{T}_{B^\pm}$ tether tensions and the projection ($\tilde{P}_{y_k}$) of the vector $\overline{O_E O_B}$ over $\boldsymbol{y}_k$.

Next section presents the error models used in Eq. (4.12) and the process models of the biases used in Eq. (4.4). A detail description of the process and observation models (functions $\boldsymbol{f}_{proc}$ and $\boldsymbol{h}$ in Eqs. (4.4) and (4.12)) and the pre-flight calibration process are explained in Appendix. A and B.

4.4 Sensors error models

4.4.1 IMU error model

Specific force and angular velocity measurements in the S_K body axes, as well as the yaw angular rate measured by the ground wind-station in the S_V axes, are provided by Inertial Measurement Units (IMUs). Classic characterization of IMU error models involves techniques such as the "Allan Variance" and "Power Spectral Density (PSD)" [28, 53]. Those methods present limitations when applied to low-cost MEMS (micro-electro-mechanical systems) consumer-grade inertial sensors, such as poor frequency differentiation of different error sources. Nevertheless, classic error models for IMUs

measurements, tend to be overcomplicated and difficult to implement on real time applications such as *state estimation* on flight controls systems. Xing and D. Gebre described a more efficient method for modeling low cost inertial units which are not supposed to be used in a stand-alone fashion, but integrated with additional sensors (namely GPS and magnetometer) [107]. Such a post calibration error model is

$$\tilde{y} = (1 + k)y + b(t) \tag{4.15}$$

where y is the measured physical magnitude (i.e. the body-axes components of the specific force/angular velocity), k is a scale factor error, b is a time varying Bias and $\tilde{y}$ is the sensor representation of y.

For low cost sensors, in-run stochastic variations of k are neglected against variations of b, thus considered constant and calculated during the calibration phase. Bias error can be modeled as $b(t) = b_0 + b_R(t)$ where b_0 is usually referred as a "turn-on to turn-on bias" and also considered an in-run constant easily calculated during the calibration phase as a constant null-shift. Finally, b_R represents a random bias-drift (or model post-calibration residual error).

Xing and D. Gebre proposed $b_R(t)$ to be the sum of wide band, uncorrelated noise $\eta_{imu}(t)$ and correlated noise $b_c(t)$. The correlated noise, $b_c(t)$, is then defined using a first order Gauss-Markov process, where the variance of the driving noise, $\sigma^2_{b_c}$, and the time constant τ_{b_c} are tuning parameters adjusted to over bound the Allan Variance plot of correlated noise. Assuming that in-run constant errors (k scale factor and b_0 turn-on to turn-on bias) have been previously removed in a pre-flight calibration phase (Appendix. B), and denoting the IMU correlated noise $b_c(t)$ as $\mathbf{\Theta}_{imu}(t)$, our model reads

$$\tilde{\mathbf{y}}_b = \mathbf{y}_b + \mathbf{\Theta}_{imu}(t) + \boldsymbol{\eta}_{imu}(t) \qquad\qquad \eta_{imu_i} \in N(0, \sigma^2_\eta) \tag{4.16}$$

$$\dot{\mathbf{\Theta}}_{imu}(t) = -\frac{1}{\tau_{b_c}}\mathbf{\Theta}_{imu}(t) + \mathbf{w}_{imu} \qquad\qquad w_{imu_i} \in N(0, \sigma^2_{b_c}) \tag{4.17}$$

where subscript b denotes body-axes (S_K or S_V reference frames). Eq. (4.16) is the error model for the specific forces/angular rates measurements included in the EKF observation model, and Eq. (4.17) is the IMU Bias-Drift model included in the EKF process model. The selected values for τ_{b_c} and $\sigma^2_{b_c}$ using Xing and D. Gebre methodology are given in Table. A.1.

4.4.2   Magnetometer error model

Earth magnetic field measurements in both, kite (S_K) and wind-station (S_V) body axes, are affected by both, Earth magnetic field local perturbations and magnetometer sensors error. A comprehensive description of local soft and hard iron perturbations and calibration procedures can be found in [38]. Hard-iron calibrations were performed prior

every flight while soft-iron perturbations were monitored to be neligible according to calibration figures (Appendix. B).

A post-calibration sensor error model is proposed as a constant bias plus wide band not correlated noise

$$\tilde{\boldsymbol{B}}_b = \boldsymbol{B}_b + \boldsymbol{\Theta}_{\boldsymbol{B}} + \boldsymbol{\eta}_B \qquad \eta_B \in N(0, \sigma_{\eta_B}^2) \tag{4.18}$$

$$\dot{\boldsymbol{\Theta}}_B = 0 \tag{4.19}$$

where subscript b denotes body-axis (S_K or S_V reference frames). Eq. (4.18) is the error model for the Earth magnetic field measurements included in the EKF observation model, and Eq. (4.19) is the magnetometer bias model included in the EKF process model.

4.4.3 GPS velocity and position error model

Ground velocity and kite position in the S_E Earth reference frame are provided by a GPS sensor. In this work, GPS latency was not considered, and the error model includes only wide band, not correlated noise

$$\tilde{\boldsymbol{v}} = \boldsymbol{v} + \boldsymbol{\eta}_v \qquad \eta_v \in N(0, \sigma_{\eta_v}^2) \tag{4.20}$$

$$\tilde{\boldsymbol{r}} = \boldsymbol{r} + \boldsymbol{\eta}_r \qquad \eta_r \in N(0, \sigma_{\eta_r}^2) \tag{4.21}$$

where Eqs. (4.20)-(4.21) are the error models for the S_E kite ground velocity and position measurements included in the EKF observation model.

4.4.4 Air data error models

An on-board multi-hole pitot tube and air-data computer, provides measurements of the kite AoA ($\tilde{\alpha}$) and AoS ($\tilde{\beta}$) plus impact and static pitot pressures ($\tilde{p}_i$ and $\tilde{p}_s$). The kite true airspeed is pre-computed and treated as an input measure to the filter as

$$\tilde{v}_a = \sqrt{\frac{2(\tilde{p}_i - \tilde{p}_s)}{\rho}} \tag{4.22}$$

where ρ represents the air density at the test area obtained from the International Standard Atmosphere [52].

This sensor is factory pre-calibrated by the manufacturer and a post-calibration error model is limited to wide band not correlated noise

$$\tilde{\alpha} = \alpha + \eta_\alpha \qquad\qquad \eta_\alpha \in N(0, \sigma_{\eta_\alpha}^2) \tag{4.23}$$

$$\tilde{\beta} = \beta + \eta_\beta \qquad\qquad \eta_\beta \in N(0, \sigma_{\eta_\beta}^2) \qquad (4.24)$$

$$\tilde{v}_a = v_a + \eta_{v_a} \qquad\qquad \eta_{v_a} \in N(0, \sigma_{\eta_{v_a}}^2) \qquad (4.25)$$

where Eqs. (4.23)-(4.25) are the error models for the kite AoA, AoS and aerodynamic speed included in the EKF observation model.

Additionally, measurements of on the ground atmospheric static pressure ($\tilde{p}_{w_s}$), and wind impact pressure ($\tilde{p}_{w_i}$) are provided by the wind-station. The wind true air speed ($\tilde{V}_w$) is analogous pre-computed and treated again as an input measure to the filter:

$$\tilde{V}_w = \sqrt{\frac{2(\tilde{p}_i - \tilde{p}_s)}{\rho}} \qquad (4.26)$$

However, opposite to the Aeroprobe™air-data computer, measurements from the Pix-Hawk™pitot tube of the ground wind-station are not factory calibrated. A measurement error for the wind airspeed is included as a random walk plus wide band not correlated noise

$$\tilde{V}_w = V_w + \Theta_{V_w} + \eta_{V_w} \qquad \eta_{V_w} \in N(0, \sigma_{\eta_{V_w}}^2) \qquad (4.27)$$

$$\dot{\Theta}_{V_w} = -\frac{1}{\tau_{V_w}}\Theta_{V_w} + w_{V_w} \qquad w_{V_w} \in N(0, \sigma_{w_{V_w}}^2) \qquad (4.28)$$

where Eq. (4.27) is the error model for the wind airspeed included in the EKF observation model, and Eq. (4.28) is the wind airspeed Bias model included in the EKF process model.

4.4.5 Tether forces

Linear load-cells are used to measure generated tensions over the tethers at the anchoring points on the control bar (A detailed descrition of the experimental rig is provided in Chapter. 3). All the tethers of the experimental rig are considered mass-less and their aerodynamic drag is deprecated, so that the measured tensions are considered to be transferred directly to the kite. It must be denoted that, although the state vector of the filter just contains the magnitude of the tether forces, an estimation of the vectors can be provided if we assume that the generated tensions are along the line determined by the attachment points $A^\pm$ (and $B^\pm$ for the 4-lines kites) and O_E.

Hereafter, we will take

$$\boldsymbol{T}_{A^\pm} = -T_{A^\pm}\overline{O_E A^\pm}/|\,\overline{O_E A^\pm}\,| \qquad (4.29)$$

$$\boldsymbol{T}_{B^\pm} = -T_{B^\pm}\overline{O_E B^\pm}/|\,\overline{O_E B^\pm}\,| \qquad (4.30)$$

with

$$\overline{O_E A^\pm} = r + \overline{O_B A^\pm}, \tag{4.31}$$

$$\overline{O_E B^\pm} = r + \overline{O_B B^\pm}, \tag{4.32}$$

$$\overline{O_B A^\pm} = X_A i_K \pm Y_A j_K + Z_A k_K \tag{4.33}$$

$$\overline{O_B B^\pm} = X_B i_K \pm Y_B j_K + Z_B k_K \tag{4.34}$$

The coordinates of the attachment points of the two kites are given in Table 4.1. Equations (A.11)-(A.12) assume that the tethers are straight, and also used the fact that the tethers are much longer than the distance between the center of mass of the kite and the IMU, and also any distance related with the setup of the control bar (see Table 3.1). This pair of equation gives the tether tensions as a function of the state vector of the filter.

Load cells were calibrated prior to test flights for scale factor k, and zero-crossing identification. A post-calibration error model containing only wide band, not correlated noised is proposed

$$\tilde{T} = T + \eta_T \qquad\qquad \eta_T \in N(0, \sigma_{\eta_T}^2) \tag{4.35}$$

where Eq. (4.35) is the error model of the tether forces magnitude included in the EKF observation model.

4.5 EKF implementation

The application of the EKF to Eqs. (4.4)-(4.12) is standard (see for instance Ref. [100]). As usual, superscripts $-$ and $+$ denote the *a priori* (before measurement) and *a posteriori* (after measurement) estimated values, respectively. Given the estimated value of the state vector $\hat{x}_j^+$ and the covariance matrix $\bar{P}_j^+$ at instant t_j, the EKF computes their values at a later instant t_{j+1} as follows. First, in the prediction phase, the reference trajectory $x_R(t)$ is computed by integrating Eq. (4.4) without noise

$$\frac{dx_R(t)}{dt} = f[x_R(t)] \tag{4.36}$$

from $t = t_j$ to $t = t_{j+1}$ and with the initial condition $x_R(t_j) = \hat{x}_j^+$. An approximation of the state transition matrix $\bar{\Phi}$ is obtained by integrating the linearized version of Eq. (4.36)

$$\frac{d\bar{\Phi}}{dt} = \bar{J}\bar{\Phi} \tag{4.37}$$

with initial condition $\bar{\Phi}(t = 0) = \bar{I}$, and $\bar{J}$ the Jacobian of f evaluated at $\hat{x}_j^+$. The *a priori* state vector and covariance matrix at t_{j+1} are

$$x_{j+1}^- = x_R(t_{j+1}) \tag{4.38}$$

$$\bar{P}_{j+1}^- = \bar{\Phi}\bar{P}_j^+\bar{\Phi}^T + \bar{G}\bar{Q}\bar{G}^T \tag{4.39}$$

The Kalman gain is

$$\bar{K}_{j+1} = \bar{P}_{j+1}^- \bar{H}_{j+1}^T \left(\bar{H}_{j+1} \bar{P}_{j+1}^- \bar{H}_{j+1}^T + \bar{R} \right)^{-1} \tag{4.40}$$

with $\bar{H}_{j+1}$ the Jacobian of h evaluated at $\hat{x}_{j+1}^-$. The *a posteriori*, i.e. corrected by the measurements, estimations at t_{j+1} are

$$\hat{x}_{j+1}^+ = \hat{x}_{j+1}^- + \bar{K}_{j+1} \left[\tilde{y}_{j+1} - h\left(\hat{x}_{j+1}^- \right) \right] \tag{4.41}$$

$$\bar{P}_{j+1}^+ = \left(\bar{I} - \bar{K}_{j+1}\bar{H}_{j+1} \right) \bar{P}_{j+1}^- \tag{4.42}$$

Initialization of the filter is done by a-priori knowledge of the kite position and attitude at take off. Usually, the LEI kite is launched from on side of the flying window, with a bank angle of $\phi = \pm\pi/2$, zero pitch ($\theta = 0$) and a heading angle (ψ) determined by the wind direction, and estimated from the on-board magnetometer measures at launching time. On the other hand, the RFD kite is launched downwind of the O_E attaching point, right into the center of the *flying window*. In this case, pitch angle (θ) equals to $\pi/2$, bank angle ϕ equals zero, and as for the LEI kite, the heading angle (ψ) is determined by the wind direction. The remaining kite state vector x_k are initialized by using the information provided by the GPS at launching time, and assuming zero angular velocity.

The state vector of the first order of Markov models (χ_1) for the aerodynamic force and moment, tether tensions and wind speed and heading, is initialized by setting the specific forces equal to minus the weight, zero moments, and wind velocity and its heading angle taken from average measurements before the flight. Finally, vectors x_{bias}, χ_2, and χ_3 are initialized to zero.

On the other hand, following [46], the covariance matrix is initialized with the measured noise of the measured variables, and to one-forth of the estimated initial value of the state for the unmeasured ones. The filter parameters has been tuned by using the sensors data sheets and also by analyzing the effect of the different parameters on the filter output. A full description of the filter and the parameters used in this work are given in Appendix A and Table A.1, respectively.

5 EXPERIMENTAL RESULTS

In this chapter, the application of the proposed methodology to three different flight campaigns is described and the results are presented. The experimental setup described in Chapter. 3, and the FPR approach in Chapter. 4, represent the final iteration of the methods developed throughout this thesis work. However, low cost, simpler solutions were used for concept validation and understanding of the problem. Once the first flight campaign with the $10\,m^2$ and $13\,m^2$ LEI kites was completed, an analysis of the obtained data and the viability of the method (specially the FPR solution) was performed. Such analysis allowed to improve and modify the experimental setup. For this reason, a description of the first *"proof of concept"* setup, and the results of its flight tests, are described in section 5.1 to justify the introduced modifications. When the experimental setup was updated and reached its final configuration, two additional flight campaigns were conducted with the $10\,m^2$ LEI and RFD kites. Its results are shown in Sec. 5.2, which also presents quantitative information about the aerodynamic characteristics of the LEI and RFD kites. A general overview of the different phases of this project, showing the evolution of the experimental setup, FPR algorithm and lessons learned at each phase is given in Table. 5.1

Project phase	Experimental Setup	FPR algorithm	Lessons Learned
Proof of Concept	**Instrumented four-line, COTS, LEI kites ($10m^2$ and $13m^2$) with PixHawk open hardware, including:** GPS, IMU, magnetometer, static and dynamic pressure sensors. **Instrumented, COTS Control bar with:** Four load-cells and two distance sensors	**Four-line kite, first implementation** Direct measurements of the kite AoA, and AoS are not implemented. The kite aerodynamic speed is measured by the onboard PixHawk pitot tube. Direct measurements of the wind state vector are not implemented.	Handling qualities of LEI kites are heavily affected by the weight of the control lines load cells, and the forwarded CoG due to the onboard instruments. PixHawk dynamic pressure sensor is heavily biased and noisy. High quality, direct measurements of the kite AoA, AoS and TAS, are required to aerodynamically characterize the kite.
LEI kite flight testing	**$10m^2$, four-line, LEI kite. Proof of concept design plus:** Onboard multi-hole pitot tube and high quality Aeroprobe air data computer. Instrumented wind station. Ad-hoc control bar with integrated load-cells (distance sensors are not included).	**Four-line kite, final implementation** EKF observation model includes the kite AoA and AoS, plus the wind speed, yaw angular rate, and wind-vane body-axes Earth magnetic field measurements. The kite aerodynamic speed is measured by the Aeroprobe airdata computer.	Albeit the new control bar, the kite handling qualities are still heavily affected and the kite easily overflies its anchoring point on the ground. Limitations of the experimental setup such as short tether lengths, manual control and maximum acceptable generated forces, led to small flying windows and higher AoA as in comparison with other power-producing systems. The experimental setup provided only limited flight data due to the kite crashing.
RFD kite flight testing	**Two-line RFD kite. Same that LEI kite plus:** Ad-hoc control bar adapted to two-line kites.	**Two-line kite implementation** Same that for the LEI kite, adapted to two-line kites.	Good handling qualities of the instrumented kite. The kite flies with higher aerodynamic speed and lower AoA than LEI kites. The experimental setup provided abundant and good quality flight data.

TABLE 5.1: Evolution of the experimental setup and FPR algorithm.

5.1 Proof of concept

The first iteration of the proposed methods was an experimental setup as simple and low cost as possible. As described in Chapter. 3, low cost, COTS instruments based on the PixHawk™ hardware were selected for the onboard instrumentation. Consequently, the high cost and fragile multi hole pitot tube and air data computer were not present in the original configuration. Additionally, some hypothesis were introduced which greatly simplified the experimental setup,

i Under the assumption that the wind remains relatively constant during a short flight test, the first iteration of the experimental setup did not provide direct measurements of the wind speed and heading during the flight. A ground wind-station was not included in the setup.

However, the wind state vector ($\boldsymbol{x}_w = [V_w, \ \psi_w]$) was already introduced in the FPR algorithm and modeled as a second order Markov system. The parameters of these Markov model were adjusted to allow only limited dynamics of the state variables (V_{w1} and ψ_{w1}) around the measured initial values for wind speed and heading. Manual tuning of these parameters allowed enough variability of the wind state variables for a good convergence of the EKF, while keeping close to the initial wind measures.

ii A precise estimation of the kite true airspeed, AoA and AoS are required to characterize the aerodynamic forces. In the proposed approach to the FPR problem, an estimation of the kite aerodynamic velocity component in the S_K body axes ($\boldsymbol{v}_a$), was obtained a-posteriori as a combination of the reconstructed wind vector and kite ground speed,

$$\boldsymbol{v}_a = \boldsymbol{v} - \bar{\boldsymbol{R}}_{EK}^T \begin{pmatrix} \cos\psi_{w1} \\ \sin\psi_{w1} \\ 0 \end{pmatrix} V_{w1} \tag{5.1}$$

where $\bar{\boldsymbol{R}}_{EK}^T = f(\Upsilon)$ represents the rotation matrix from S_E to S_K as a function of the kite state variables (ϕ, θ and ψ). Eq. 5.1 is equivalent to Eq. A.2, albeit for the kite angular rotation contribution. This is because, in the first flight configuration, the boom with the multi hole pitot tube was not introduced and, consequently, the distance from the IMU to the pitot tube nose was ignored.

After denoting the kite aerodynamic velocity as $\boldsymbol{v}_a = u_a \boldsymbol{i}_K + v_a \boldsymbol{j}_K + w_a \boldsymbol{k}_K$,

$$v_a = \mid \boldsymbol{v}_a \mid \tag{5.2}$$

$$\alpha = \arctan\left(\frac{w_a}{u_a}\right) \tag{5.3}$$

$$\beta = \arcsin\left(\frac{v_a}{\mid \boldsymbol{v}_a \mid}\right) \tag{5.4}$$

In the first version of the experimental setup, the aerodynamic speed of the kite was measured onboard by the low cost, PixHawk™ pitot tube. However, the kite AoA and AoS were not measured. This was due to the fact that, a straightforward, precise and low cost solution for measuring the kite attitude within the airflow was not available. This was a major limitation for the original experimental setup performance. Although in-house developed sensors for AoA and AoS measurement (wind vanes) were considered, they were discarded because of expected high hysteresis and biases due to insufficient dynamic pressure over the wind vanes, unbalanced wind vane mass distribution due to manufacturing (mainly 3D printing) limitations, and rotation axis frictions. Finally, it was decided that, if a sensor for AoA and AoS measurements would be introduced in the next generation of the experimental setup, it should be a COTS, high quality and costly instrument.

iii Due to the expected higher payload of big LEI kites, COTS kitesurfing kites were firstly considered. It was assumed that, for a big LEI kite, the weight of the on-board instruments plus the ad-hoc 3D printed rig to support those instruments to the kite, were negligible in comparison with the generated aerodynamic force. Additionally, for simplicity and fast implementation, a kitesurfing COTS control bar was chosen to control the kites as described in Chapter. 3.2. In this control bar, the load-cells used to measure the tethers tensions were directly inserted in the lines and again it was assumed that the weight of theses load cells was negligible in the system dynamics.

In the first flights, measurements of the control bar inputs to the kite were considered. Assuming that the pilot maneuvers the kite while keeping the control bar inside plane Π (Chapter. 3.2), the control bar state vector ($\boldsymbol{x}_c = [u_p \ v]$) was obtained through the measurements of two distance sensors secured to the safety fuse of the control bar. The measurements of the control inputs to the kite allowed to evaluate the coherence of the FPR algorithm.

The state vector of the FPR algorithm for the first flights reads,

$$\boldsymbol{x} = \begin{bmatrix} \boldsymbol{x}_k & \boldsymbol{x}_{bias} & \chi_1 & \chi_2 & \chi_3 \end{bmatrix} \tag{5.5}$$

Including, (i) the *kite state vector* ($\boldsymbol{x}_k$ in Eq. (4.6)). (ii) The *bias state vector* $\boldsymbol{x}_{bias} = \begin{bmatrix} \Theta_B & \Theta_f & \Theta_\omega & \Theta_a \end{bmatrix}$, where Θ_a stands for the bias of the aerodynamic speed measured by the PixHawk™ pitot tube. And (iii), the three *pseudo states vectors* $\chi_i = [\boldsymbol{F}_{ai} \ \boldsymbol{M}_{ai} \ T_{A^+i} \ T_{A^-i} \ T_{B^+i} \ T_{B^-i} \ V_{wi} \ \psi_{wi}]_{i=1,2,3}$

The observation vector of the FPR algorithm reads,

$$\tilde{\boldsymbol{y}} = \begin{bmatrix} \tilde{\boldsymbol{B}} & \tilde{\boldsymbol{v}} & \tilde{\boldsymbol{r}} & \tilde{\boldsymbol{f}} & \tilde{\boldsymbol{\omega}} & \tilde{v}_a & \tilde{T}_{A^+} & \tilde{T}_{A^-} & \tilde{T}_{B^+} & \tilde{T}_{B^-} & \tilde{D} & \tilde{P}_{yb} \end{bmatrix} \tag{5.6}$$

Including, the S_K-components of the Earth magnetic field measured by the onboard magnetometer ($\tilde{\boldsymbol{B}}$), the S_E-components of the velocity and position vectors of the kite

measured by the onboard GPS ($\tilde{\boldsymbol{v}}$ and $\tilde{\boldsymbol{r}}$), the S_K-components of the specific force and angular velocity measured by the IMU ($\tilde{\boldsymbol{f}}$, $\tilde{\boldsymbol{\omega}}$), the magnitude of the kite true airspeed, the four magnitudes of the measured tether forces ($\tilde{T}_{A\pm}$ and $\tilde{T}_{B\pm}$), the constant distance from the kite anchoring point on the ground O_E to the CoG of the kite ($\tilde{D}$), and the null projection ($\tilde{P}_{yb}$) of the vector $\overline{O_E O_B}$ over $\boldsymbol{y}_k$.

5.1.1 Flight data analysis and validation

First flight tests were carried out with the $13\,\mathrm{m}^2$ and $10\,\mathrm{m}^2$ LEI kites under similar wind conditions. Testing procedure started by powering all the sensors while the kite was on the ground. Px4™ software was modified to automatically start recording data from all the on-board sensors after powering up. Once a valid GPS signal was acquired, the kite was launched and steered towards a stable equilibrium state close to the zenith. At that moment, the data acquisition software and the synchronization time signal were started, thus allowing a synchronous data acquisition of the onboard and on the ground instruments (see *Start* point in Fig. 5.1). The kite was piloted into different equilibrium positions and dynamic maneuvers. When the experiment was finished (see *Finish* point in Fig. 5.1), the kite was landed, the data acquisition software was stopped, and all systems were powered off.
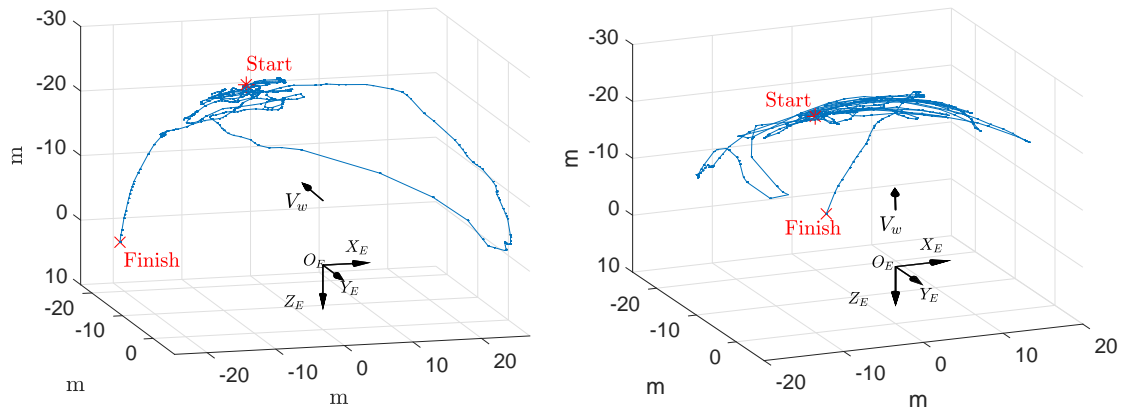

FIGURE 5.1: Left and right panels show respectively, the GPS trajectories of the $13\,\mathrm{m}^2$, and $10\,\mathrm{m}^2$ LEI kites.

Acquired measurements were analyzed off line for experimental setup validation and general data coherence. For signals synchronization, the first rising-up edge of the recorded synchronism signal is used as t_0 initial point. All signals were re-sampled using a common 50 Hz time vector. A general overview of the $13\,\mathrm{m}^2$ and $10\,\mathrm{m}^2$ LEI kites, S_E projected trajectories, as measured by the on-board GPS are shown in Figure 5.1. These trajectories are contained in the so called *wind window*, defined as the

downwind quadrant of the sphere of radius equal to the tethers length and origin at the anchoring point of the kite to the ground (O_E).

Load cells range validation.

One key design decision was load cells range selection, which was made according to the expected generated aerodynamic forces. Two main hypothesis were assumed (Chapter. 3.4.2): (i) the generated aerodynamic forces could be limited to twice the maximum static lift, and (ii) due to the kite design, most of the aerodynamic forces are supported by both front lines.

As shown in Figure 5.2, total tension in the main front lines for the $13\,\mathrm{m}^2$ kite remained under $500\,\mathrm{N}$. The only exception was a high dynamic maneuver that exceeded the $1000\,\mathrm{N}$ design point (two $50\,\mathrm{kg}$ load cells were used in the front line). Additionally, as expected, tensions in the control lines represented only a small fraction of the generated total forces.
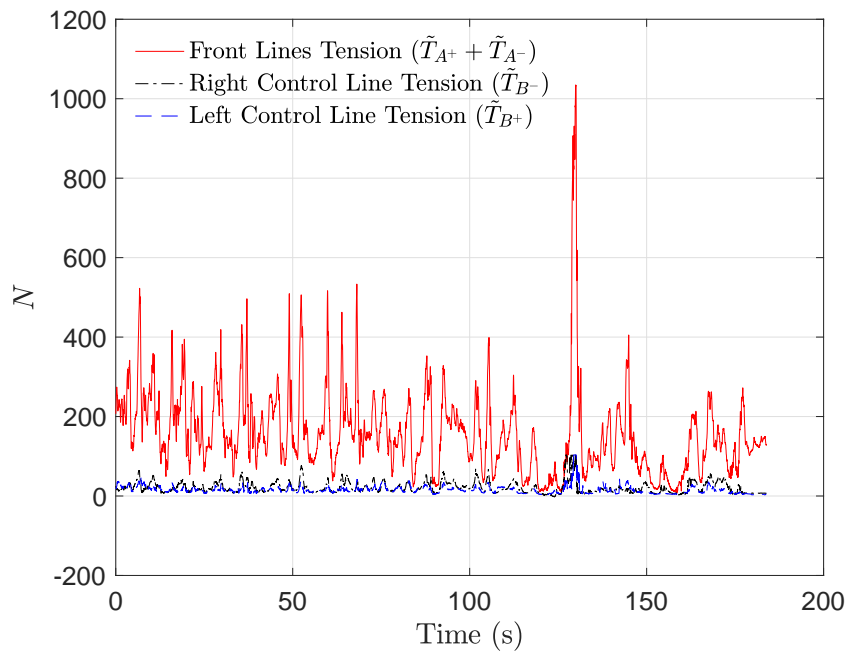

FIGURE 5.2: Tensions in the front and control lines in the proof of concept tests with the $13\,\mathrm{m}^2$ Kite.

Kite True Air Speed validation.

As described in 4.4.4, the differential pressure $\tilde{p}_d$, measured by the pitot tube was transformed into True Air Speed (TAS) by using

$$TAS = \sqrt{\frac{2\tilde{p}_d}{\rho}} \tag{5.7}$$

where $\rho = 1.15 kg/m^2$ is the air density at the test area obtained from the International Standard Atmosphere for the given flight test date. The calculated TAS was used by the observation model as $\tilde{v}_a$. The dashed line in panel (a) of Figure. 5.3, shows the differential pressure ($\tilde{p}_d$) measured by the PixHawk on-board differential pressure sensor. These pressure measurements are heavily biased and noisy. For specific instants, they were zero or even negative, thus revealing the low quality of the aerodynamic data in the proof-of-concept experimental setup.
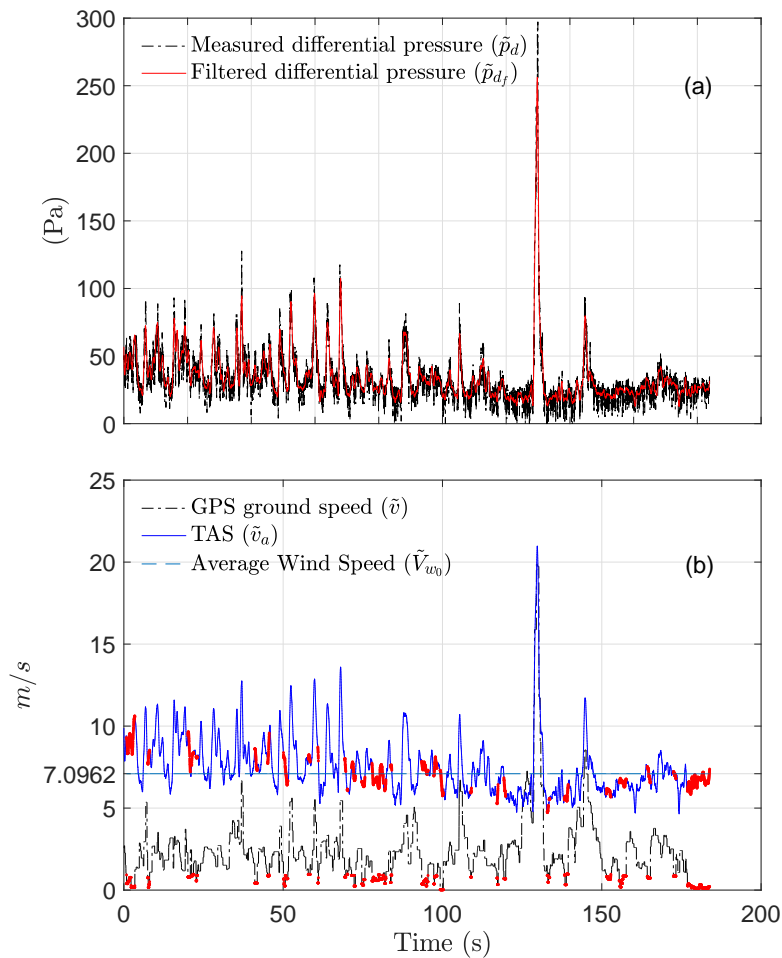
FIGURE 5.3: Panel (a) shows raw and filtered measured differential pressures. Panel (b) shows calculated TAS and GPS measured ground speed

For validation purposes, $\tilde{p}_d$ was filtered using a third order Savitzky Golay filter (red line in Fig. 5.3(a)), and used to calculate a filtered TAS ($\tilde{v}_a$). The resulting TAS was compared with the GPS measured kite ground speed ($\tilde{v}$) in panel (b) of Fig. 5.3. For a stationary flight with zero ground speed, measured TAS equals wind air speed.

A selection of stationary flight periods with negligible kite ground speed (marked in red in Fig. 5.3(b)) were used to calculate an estimated average TAS (wind speed) of $7\,\mathrm{m\,s^{-1}}$. This wind speed estimation was coherent with pre-flight measurements and flight day forecast. Also, the magnitude of the aerodynamic forces was coherent with the expected values for that wind speed and kite size (Chapter. 5.1.1). Thereafter, albeit the poor performance of the PixHawk differential pressure sensor, the measurements were coherent with the flight parameters. However, it was decided that a precise measurement of the kite aerodynamic speed would require a new differential pressure sensor.

FPR algorithm validation.

The application of the filter to the recorded flight data exhibited a high robustness with little sensitivity to its initialization. For instance, in the first flights, the FPR state vector was initialized when the kite was flown to the zenith of the wind window and the synchronization signal was started. At that point, the kite attitude was assumed to be with zero pitch and roll angles (x_K body axis is pointing into the wind and z_K is parallel to z_E pointing into the ground). Then, the kite state vector reads:

$$\boldsymbol{r} = \overline{O_E O_K} = x_E \boldsymbol{i}_E + y_E \boldsymbol{j}_E + z_E \boldsymbol{k}_E = \tilde{\boldsymbol{r}}_0 \tag{5.8}$$

$$\boldsymbol{v} = d\boldsymbol{r}/dt = u \boldsymbol{i}_K + v \boldsymbol{j}_K + w \boldsymbol{k}_K = \boldsymbol{0}_{1\mathrm{x}3} \tag{5.9}$$

$$\boldsymbol{\omega} = p \boldsymbol{i}_K + q \boldsymbol{j}_K + r \boldsymbol{k}_K = \boldsymbol{0}_{1\mathrm{x}3} \tag{5.10}$$

$$\boldsymbol{\Upsilon} = [\phi\ \theta\ \psi] = [0\ \ 0\ \ \tilde{\psi}_{w_0} + \pi] \tag{5.11}$$

where $\tilde{\boldsymbol{r}}_0$ represents the S_E kite position at the *starting point* measured by the GPS, $\boldsymbol{0}_{1\mathrm{x}3}$ represents a three components null vector and $\tilde{\psi}_{w_0}$ is the wind heading at take off.

The Bias state vector, $\boldsymbol{x_{bias}}$, was initialized to zero, and the pseudo states vectors were initialized as:

$$\chi_1 = \left[\tilde{\boldsymbol{f}}_{a_0}\ \tilde{\boldsymbol{M}}_{a_0}\ \tilde{T}_{A^+_0}\ \tilde{T}_{A^-_0}\ \tilde{T}_{B^+_0}\ \tilde{T}_{B^-_0}\ \tilde{V}_{w_0}\ \tilde{\psi}_{w_0}\right] \tag{5.12}$$

$$\chi_2 = \chi_3 = \boldsymbol{0}_{1\mathrm{x}12} \tag{5.13}$$

where, $\tilde{T}_{A^+_0}\ \tilde{T}_{A^-_0}\ \tilde{T}_{B^+_0}\ \tilde{T}_{B^-_0}$ denotes the measured magnitudes at that point, $\tilde{\boldsymbol{f}}_{a_0}$, $\tilde{\boldsymbol{M}}_{a_0}$ are calculated from a static equilibrium state, and $\boldsymbol{0}_{1\mathrm{x}12}$ represents a twelve components null vector.

An initial estimation of the wind state vector ($\boldsymbol{x}_{w_0} = [\tilde{V}_{w_0},\ \tilde{\psi}_{w_0}]$) was obtained by flying the kite to the most up-wind stable positions at both sides of the wind window (S_1 and S_2). The wind vector was then estimated as a vector perpendicular to the plane defined by vectors $\overline{S_1 S_2}$ and $\boldsymbol{Z}_E$, and its modulus is obtained by averaging the measured kite TAS while the kite is stationary at S_1 and S_2. The estimated initial wind direction for the $13\,\mathrm{m^2}$ and $10\,\mathrm{m^2}$ LEI kites' flights, projected in the S_E (NED) reference frame,

is also shown in Figure 5.1 ($\boldsymbol{V_w}$).

For validation of the FPR results, some key state variables were studied and compared with the estimations of an independent estimator. This independent estimator is provided by the Px4™ flight control software, and the resulting estimated state vector was recorded synchronously with the sensors signals on-board. The state vector of the Px4™ software, does not provide all the required state variables for the EBM aerodynamic characterization of the kites. However it provides some basic variables such as kite trajectory and attitude during the flight. Figures 5.4 (a)-(c) show the evolution of the pitch, roll, and yaw angles for the 13 m²-kite during the first two minutes of flight. The dashed black lines, and the solid red lines correspond to the Px4™ and the FPR estimated attitude, respectively.
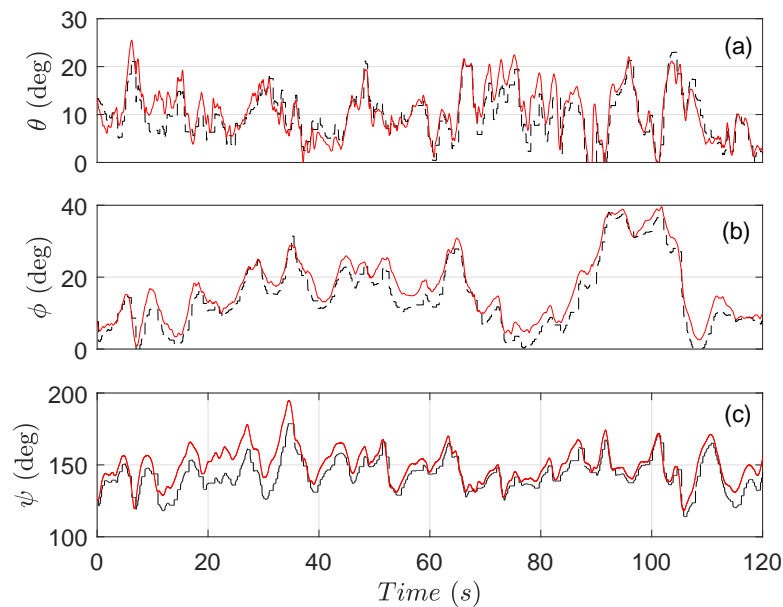
FIGURE 5.4: Euler angles of the 13 m²-kite estimated by the PixHawk™ software (dashed black) and the FPR algorithm (solid red).

Both estimations, obtained from totally independent algorithms and software, are in good agreement with discrepancies in the estimated pitch and roll angles under 5 degrees, and a little bit higher for yaw angles (specially at the beginning of the flight). They prove that the experimental setup and the filter are correctly implemented.

A second verification of the integrity of the filter is given in Fig. 5.5, which shows the GPS measured (dashed black lines) and FPR estimated (solid red lines) values of the kite position components X_E and Y_E, its altitude $H = -Z_E$, and the constraint distance D appearing in Eq. 5.6. The addition of such a constraint in the EKF greatly improved the GPS accuracy. As shown in Fig.5.5 (d), raw GPS distance to the attachment point O_E, oscillate with typical GPS accuracy values, while the FPR solution follows the
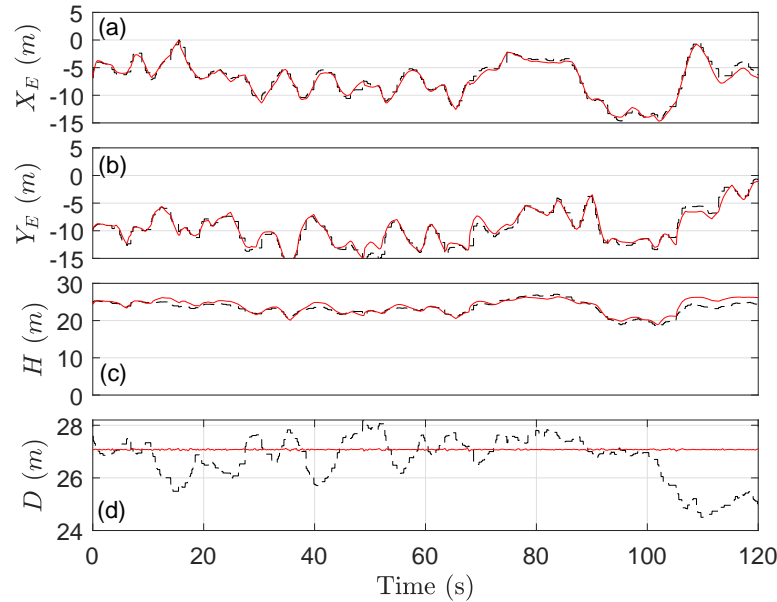
imposed constrain.

FIGURE 5.5: Positions X_E, Y_E and H, and distance D measured by the sensors (dashed black) and estimated with the FPR algorithm (solid red).

In the following, the experimental results of two different maneuvers: (i) a pull-up, i.e. continuous enhancement of the power ratio with vanishing (or small) lateral deflection of the control bar, and (ii) a steering maneuver with periodic variations of the deflection angle of the control bar, are discussed. The goal of the analysis is twofold. First, it provides quantitative information about the performances of the experimental setup and the filter, and shows coherence between control inputs and kite response. Second, it highlights some of the distinguished features of the filter such as the estimation of the aerodynamic force and moment.

Pull-up maneuver

Figure 5.6 shows the evolution of the power ratio and deflection angle of the control bar during a pull-up maneuver of the $10\,\mathrm{m}^2$-kite. As shown in the figure, the maneuver is not perfectly symmetric but close to it. The power ratio was increased smoothly from 40% to 90% approximately, and the deflection angle was held almost constant at $-4°$, i.e. the pilot was pulling slightly the right control line (the one linked to point B^- in Fig. 4.4). The position of the center of mass of the kite (not shown) remained almost constant during the time span displayed in Fig. 5.6.

The FPR of the Euler angles (pitch, yaw and roll) versus the power ratio during the pull-up maneuver are shown in Fig. 5.7 (a), where, for clarity, the yaw angle has been divided by a factor of 10. As expected, yaw and roll angles are almost constant during

the pull-up, and the pitch angle increased notably ($\Delta\theta \sim 7.1°$). These results are in agreement with the sign of the estimated angular velocities (Fig. 5.7 (b)).
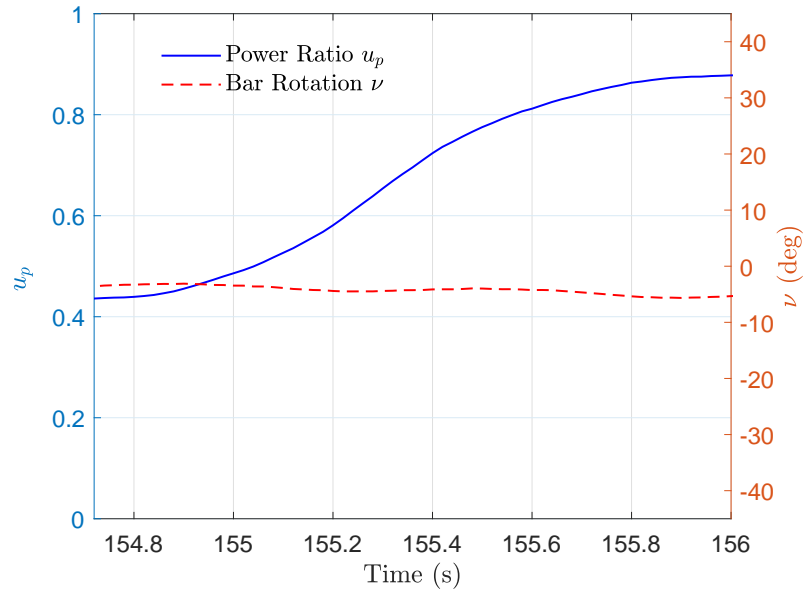

FIGURE 5.6: Power Ratio and bar deflection angle versus time during a symmetric pull-up maneuver.
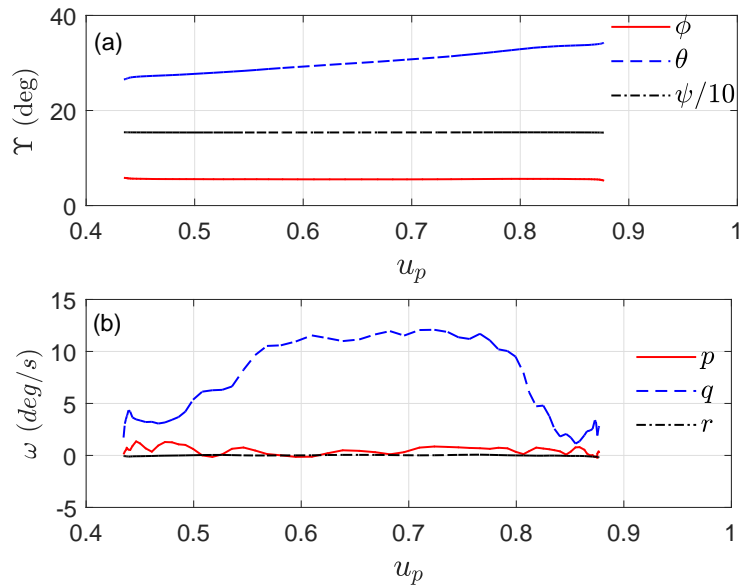

FIGURE 5.7: Pull-up maneuver: Euler angles and angular velocity versus power ratio during. Yaw angle is divided by a factor 10.

The linear dependence between the pitch angle and the power ratio can be understood from simple kinematic considerations. After assuming straight and inextensible tethers, pure rotation along j_K, and small pitch angle variations, we can write $\Delta\theta \approx -\Delta D_{cb}/R_G$ with $\Delta\theta$ being the increment of the pitch angle, ΔD_{cb} the distance increment between the control bar and the power stopper, and

$$R_G = \sqrt{(X_A - X_B)^2 + (Z_A - Z_B)^2} = 2.12\,\mathrm{m} \tag{5.14}$$

the distance between the two lines passing through points A^+ and A^- and B^+ and B^- for the $10\,\mathrm{m}^2$ kite. Calling $u_{p0} \approx 0.42$ and $u_{p\infty} = 0.9$ the initial and final power ratios, one has

$$\Delta D_{cb} = (L_s - L_{ps} - L_{ds})(u_{p0} - u_{p\infty}) \approx -0.216\,\mathrm{m} \tag{5.15}$$

that gives a pitch increment ($\Delta\theta$) of $5.84°$.

A quasi-stationary ($\Delta t \approx 1.2\,\mathrm{s}$) variation of pitch angle translates into an instantaneous increase of the kite angle of attack and modifies the aerodynamic forces. Its lateral S_K-component remains almost constant, as shown by the dashed red line in Fig. 5.8 (a). However, as expected, the longitudinal components F_{ax1} and F_{az1} increased considerably during the maneuver. Figure 5.8 (b) shows the components of the estimated aerodynamic moment.
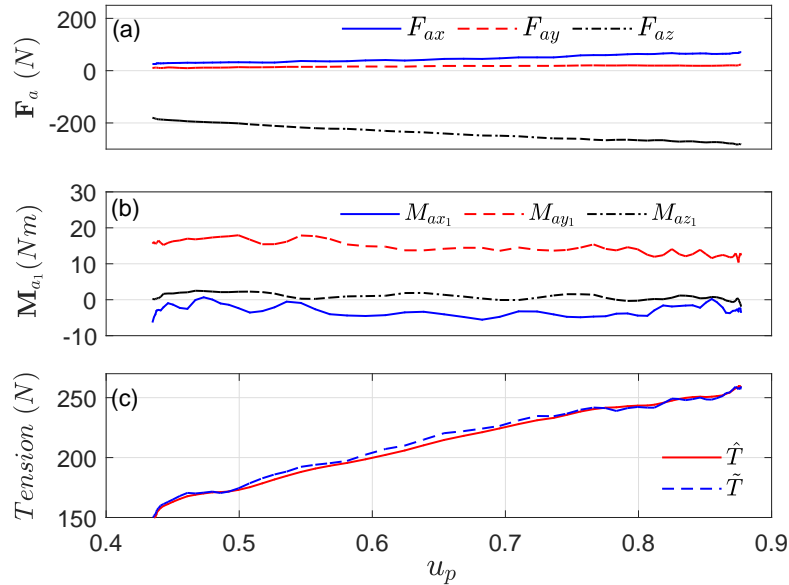

FIGURE 5.8: Pull-up manoeuver: panels (a-b) show the S_K-components of the aerodynamic force and moment versus power ratio, and panel (c) the magnitude of the estimated (solid and red) and measured (dashed and blue) total tension.

The pitch moment M_{ay1} remains relatively constant, thus suggesting a position of the center of mass close to the aerodynamic center $c/4$. This can be checked using data

provided in Table 4.1, where $c/4 \approx (X_A - X_B)/4 = 0.38$ m, and the distance of the CoG to the leading edge of the kite is approximately $X_A = 0.42$ m. On the other hand, an average wind heading angle $\psi_w \approx -60°$ and a yaw angle during the maneuver of $\psi \approx 150°$ resulted in a negative side slip angle of the kite. As expected, the estimated roll moment M_{ax1} is negative due to the negative dihedral of the wing. Finally, Fig. 5.8 (c) shows the magnitude of the resultant of the four tether tensions estimated in the FPR ($\hat{T}$), and for reference, the tensions measured by the load sensors $\tilde{T}$. Again, the tension exhibits a linear dependence with the power ratio and is almost doubled during the pull-up.

Steering maneuver

The lateral-directional dynamics of the $10\,\text{m}^2$-kite was investigated by varying periodically the deflection angle of the control bar. As shown in Fig. 5.9, the maximum and minimum deflections were about $20°$ and $-30°$. Since the force at the bar increased notably during the induced crosswind motion of the kite, the pilot could not keep the power ratio constant and it also varied periodically around the nominal value $u_p \approx 0.4$. The kite flew in crosswind conditions and moved from side to side in the wind window. A top view of the measured trajectory is displayed in Fig. 5.10, where the wind direction and the Earth axes at the initial instant of the steering maneuver are also plotted. In the following, the lateral-directional steering maneuver as seen from the point of view of the pilot placed at the origin of the wind reference frame displayed in Fig. 5.10 is discussed.
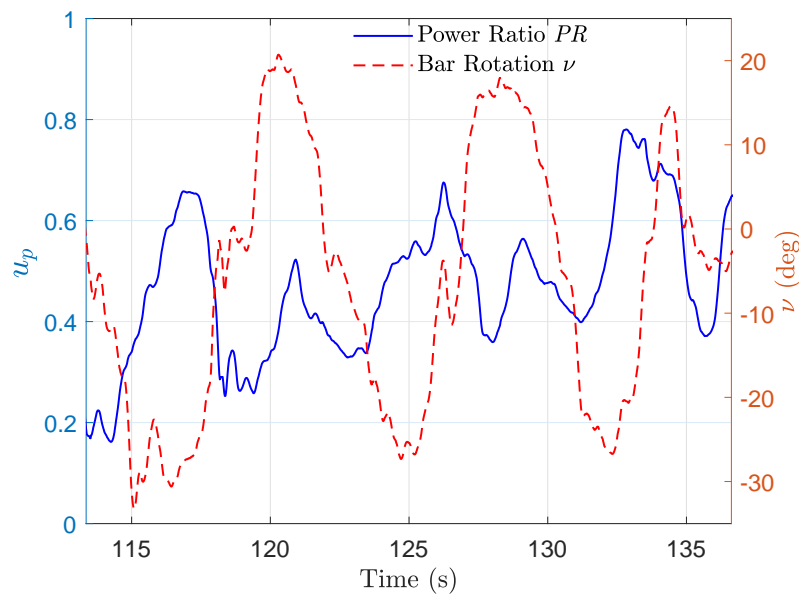

FIGURE 5.9: Power Ratio and bar deflection angle versus time during a steering maneuver.

The steering maneuver starts with the kite placed at the right side of the wind window (black circle in Fig. 5.10). Since the kite had initially a lateral velocity

pointing to the left and the pilot imposed almost zero deflection to the control bar at that instant, the kites moved laterally. While the kite was moving to the left with a positive and increasing roll angle (Fig. 5.11 (a)), the pilot pulled the right tip of the control bar, thus decreasing angle ν (Fig.5.9). Such a control input stopped the lateral motion of the kite, and avoided a kite crash at the left hand side of the wind window. The kite reached the center of the wind window and the maximum lateral displacement at instants $t = 114.6$ s and $t = 116.9$ s, respectively. The latter coincided approximately with the minimum of ν. After reaching the maximum lateral displacement at the left side, the kite moved to the right and the pilot increased the value of ν from $-27°$ at $t \approx 117$ s to $+20.46°$ at 120.4 s. The kite performed a second crosswind motion during that time interval. It is also interesting to look at the behavior of the roll angular velocity component p. At the beginning of the maneuver, p was positive and at a maximum. The action of the pilot, decreased the value of p and, once it vanished, the kite banked to the right and moved to the opposite side of the wind window. An analysis of the control inputs in Fig. 5.9 and the Euler angles in Fig. 5.11 reveals a strong correlation between the deflection of the bar and the yaw angle of the kite. The roll response does also follow these two variables but with certain delay.
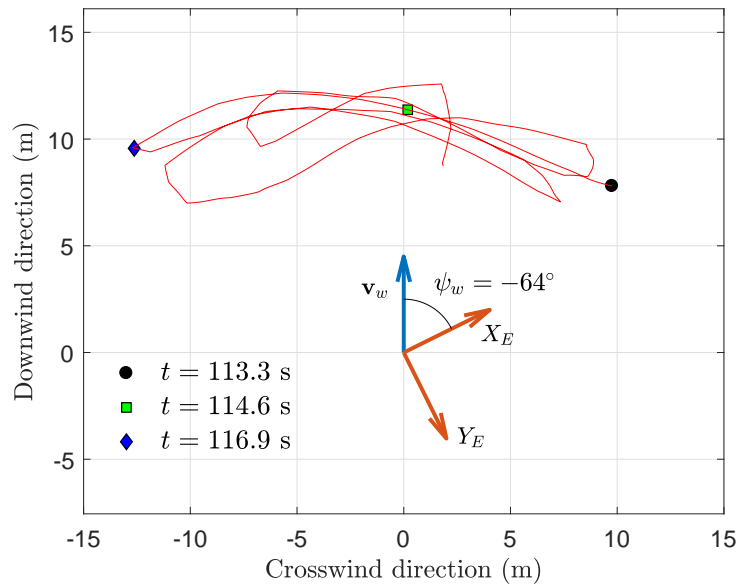

FIGURE 5.10: Top view of the kite trajectory during the steering maneuver.

The forces and torques provided by the EKF (Fig. 5.12 (a)-(b)) are coherent with the dynamics described previously. The lateral force component F_{ay1} and the roll torque M_{ax1} oscillates among positive and negative values. The longitudinal force components, especially F_{az1}, are larger than the one observed during the pull-up due to the crosswind conditions of the steering maneuver. This effect is also evident in Fig. 5.12 (c), where the magnitude of the resultant of the four tether tensions is plotted.
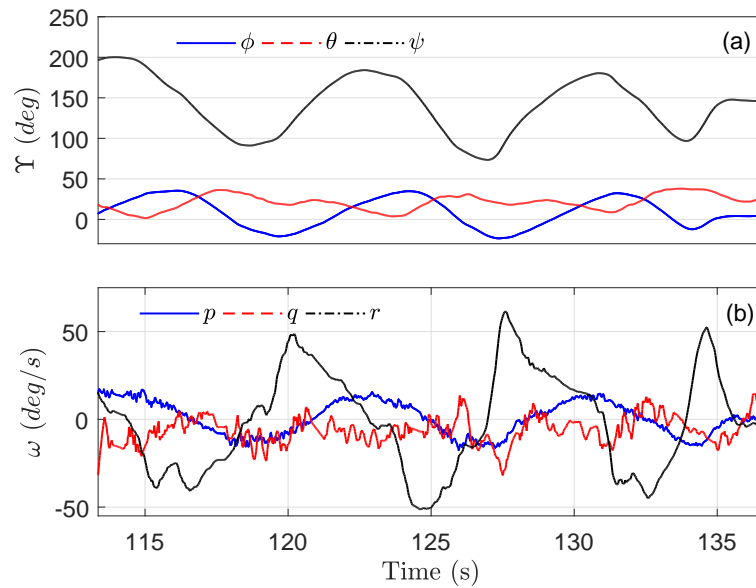
FIGURE 5.11: Panels (a) and (b) show the Euler angles and the angular velocity during the steering maneuver.
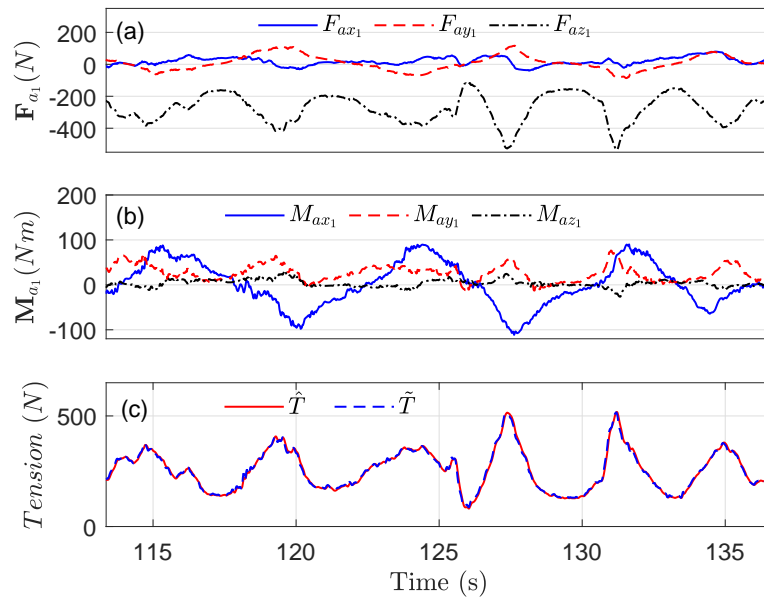

FIGURE 5.12: Panels (a) to (c) show the evolution of the aerodynamic force, torque, and the modulus of the resultant of the four tether tensions.

5.1.2 Conclusions

Two flight tests, with the $13\,\text{m}^2$ and $10\,\text{m}^2$ surfkites, have been analyzed for general coherence of the FPR results and experimental setup validation. As described before,

these flight tests were performed without onboard measurements of the kite AoA and AoS, and without on the ground measurements of the wind speed and heading. The kites were manually controlled by a human pilot on the ground using a COTS control bar, and both symmetric (pull-up) and cyclical steering maneuvers were performed. Flight tests were carried out in moderate winds of about $7\,\mathrm{m\,s^{-1}}$ gusting from $3\,\mathrm{m\,s^{-1}}$ up to $9\,\mathrm{m\,s^{-1}}$, as showed by the estimated wind speed (V_{w1}) (Fig. 5.13). The reconstructed state variables of the system (*reconstructed flight path*) showed a good agreement with the estimations of an independent estimator (Px4™software). Control inputs on the control bar also showed coherence with the dynamic behavior of the kite. The reconstructed aerodynamic forces and moments were also consistent with kite attitude and aerodynamic speed recorded by the sensors.
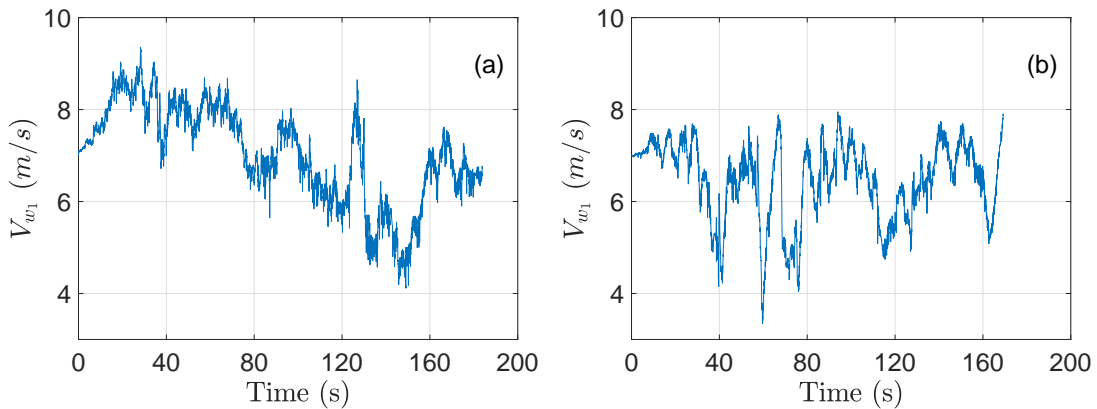

FIGURE 5.13: Panel (a) and (b) shows respectively the estimated wind speed (V_{w1}) for the $13\,\mathrm{m^2}$ and $10\,\mathrm{m^2}$ kite flights

During these flight tests, it was found that the handling qualities of the kites were heavily affected by the weight of the load cells hanging on the control lines. This effect was specially important during the wind lulls, making the kites move downwind towards the back of the wind window, loosing altitude with little lateral control authority, and even stalling the kites. As expected, this effect was more important for the smaller kite. Additionally, the weight of the onboard instruments and specially, the long boom supporting the pitot tube, made the CoG of the kites to move forward from its original location.

In some situations, when the kites were flown close to the zenith of the wind window with a combination of fast wind speed variation and low power ratio on the control bar, they could overfly their anchoring point on the ground and crash. This effect is explained because of, at placing the kite's CoG forward of the wing center of pressure, an increase of the kite lift results in a negative pitching moment around the CoG (positive static stability). At this point, if the power ratio of the control bar is instinctively diminished by the pilot due to the increased tension in the control lines, the pitch angle of the kite decreases, and consequently its AoA. The resulting lower drag translate into

a movement forward of the kite, towards the zenith of the wind window, which at the same time, it further reduces its pitch angle. If a combination of fast AoA and wind speed drop happens at the same time, the tensions on the front lines can become low enough to allow the kite to start flying like an untethered aircraft, penetrating into the wind and overflying its anchoring point on the ground. However, opposite to aircraft, if the AoA of the kite becomes negative, the textile nature of the kite canopy will loose its geometry. The lift is suddenly reduced and the kite falls. This is a well known effect in the kitesurfing sport, and makes kites with a forwarded CoG (such as low wind, strut-less kites) more critical to fly, while kites with good *drifting* abilities (negative static stability) are often preferred due to their capability to fall to the back of the wind window until tension in the front lines is restored. Nevertheless, as described bellow, the flight of the $10\,\text{m}^2$ kite finished in a crash because of a lost of control as the kite *nose-stalled* from the zenith of the flying window.

As shown in panel (b) of Figure. 5.13, 160 s after the beginning of the experiment, wind was gusting from $7.5\,\text{m s}^{-1}$ to $5\,\text{m s}^{-1}$. At that moment, the kite was starting to move towards the zenith of the wind window (Fig. 5.14), and its aerodynamic speed was increasing from $5\,\text{m s}^{-1}$ to $9\,\text{m s}^{-1}$. This resulted in an increasing lift from 50 N to 100 N, beside the reduction of the AoA due to the vertical speed of the kite (Fig. 5.15 panels (c)-(e))[1]. As a reaction to the increased lift force, the pilot quickly decreased the control bar power ratio (u_p) at $t = 161$ s, lowering the pitch of the kite and further reducing its AoA (Fig. 5.15 panels (a)-(c)). Consequently, the generated lift and drag forces were quickly reduced (panels (e)-(f)). Due to the lower drag force, the kite moved further towards the zenith of the flying window at the same time that it was flying in a wind lull of only $5\,\text{m s}^{-1}$. This resulted in a very low lift force and consequently very low tension in the tethers, with the kite overflying the anchoring point on the ground (O_E) at $t = 164$ s (Fig. 5.14). Although the pilot reacted to this situation by increasing again the control bar power ratio, which resulted in a slightly increase in the AoA, the kite stalled at $t = 165$ s. The pitch angles decreased below $0°$ and the kite fell to the left of the wind window. In an attempt to improve the LEI kite handling qualities, and avoid the added weight of the load cells on the control lines, a new control bar with integrated load-cells was developed (Fig. 3.6). Additionally, the relative lengths of the front and rear lines were tuned in an attempt to compensate the effects of a forward CoG.

Figures 5.16 and 5.17 show the a-posteriori estimation of the $10\,\text{m}^2$ kite AoA and AoS during the symmetric *pull up* and *steering* maneuvers based on the reconstructed kite state variables. The estimated magnitudes of the kite AoA and AoS for those maneuvers are high enough to consider that the kite was flying in a post-stall situation.

---

[1]If a linear behavior of the kite lift coefficient with the kite AoA is assumed, for an increment of two times of the kite aerodynamic velocity, and a reduction of two times of the AoA, a two times increase of the lift force could be expected. This is coherent with the reconstructed forces for the given maneuver.
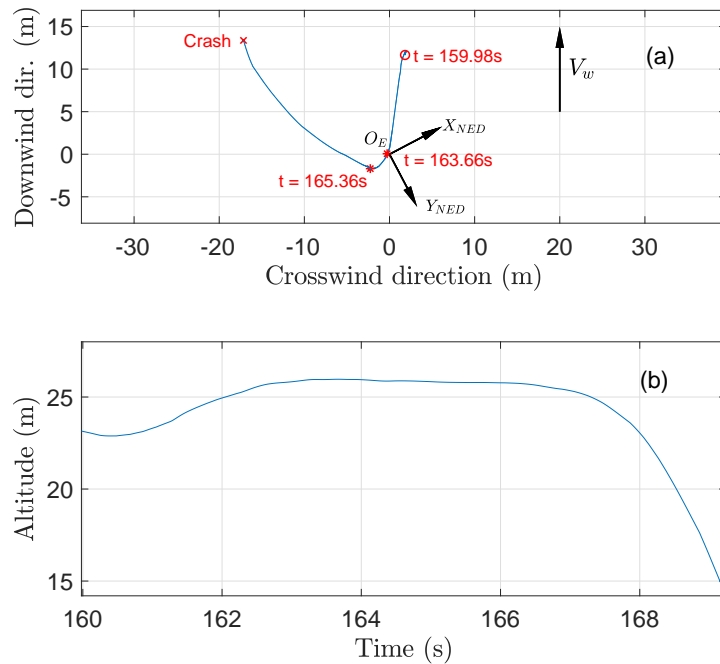
FIGURE 5.14: Panels (a) and (b) show the downwind and vertical trajectories of the $10\,\text{m}^2$ LEI kite during the crash.

This showed contradictory to previous works, where typical AoA values under 15° and AoS under 10° for a $40\,\text{m}^2$ LEI kite were reported [72, 96]. This can be explained because the presented experimental setup, albeit representative of an AWE system based on a LEI kite, still has some major differences with a "power-producing" system. Two of them are the kite size and the length of the tethers. Consequently, the trajectory described by the kite and the aerodynamic velocity vector are very different to the ones of big power-producing systems. This finding drove the need to introduce a high quality sensor for direct measurement of the kite AoA and AoS which could confirm these preliminary results. The measurement point of this new sensor should be positioned as far as possible from the kite leading edge to avoid aerodynamic interference with the kite. For this reason a 1 m long boom was considered for mounting the new multi-hole pitot tube and a new ad-hoc supporting rig was designed. This approach was also applied to a new RFD kite, with the aim of comparing its flying characteristics with the big LEI kites, as RFD kites are expected to fly faster and more forward in the wind window, resulting in overall smaller AoA.
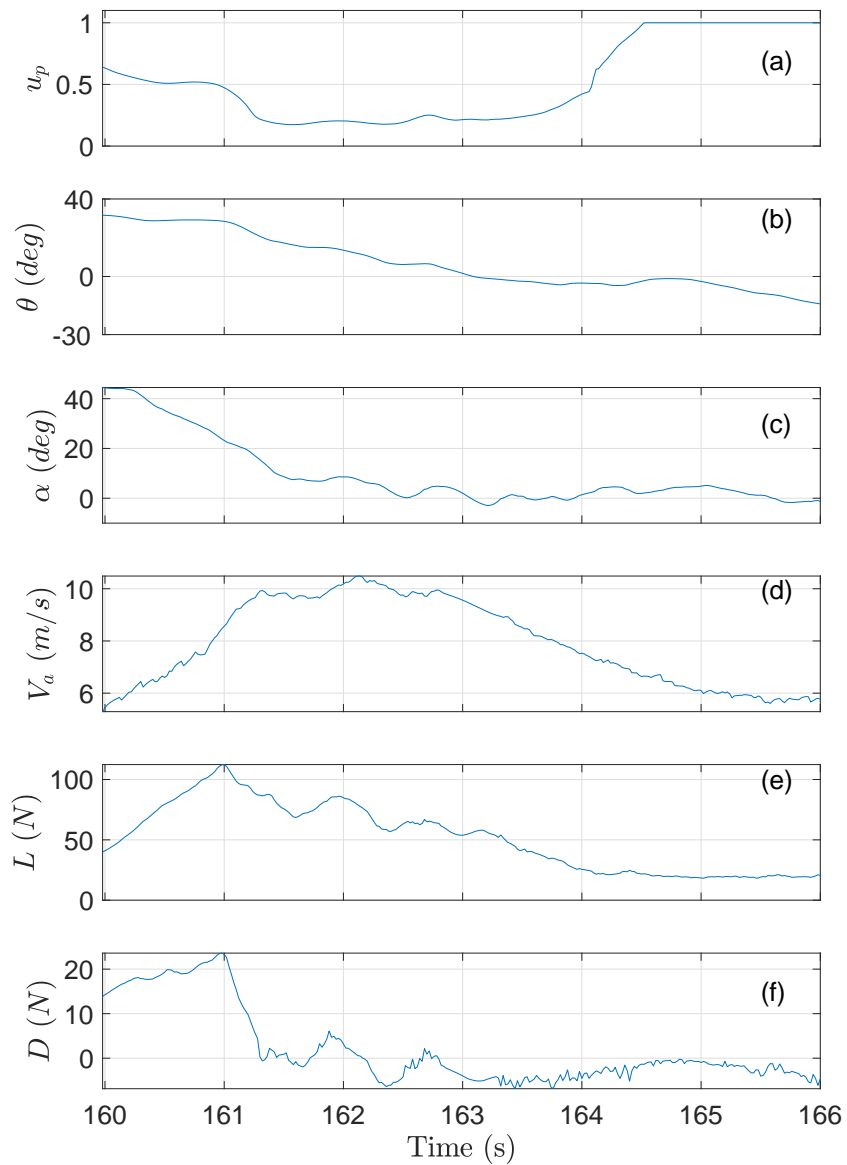
FIGURE 5.15: Panels (a)-(d) show the reconstructed control bar power ratio (u_p), pitch (θ), AoA (α), TAS (V_a), lift (L) and drag (D) of the $10\,\text{m}^2$ LEI kite during the crash.
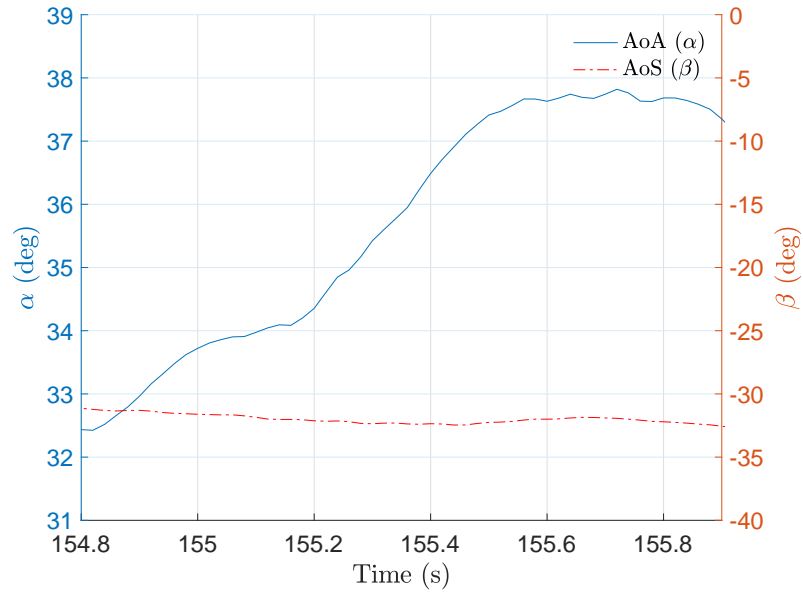
FIGURE 5.16: AoA and AoS of the $10\,\text{m}^2$ kite during the *pull-up maneuver*.
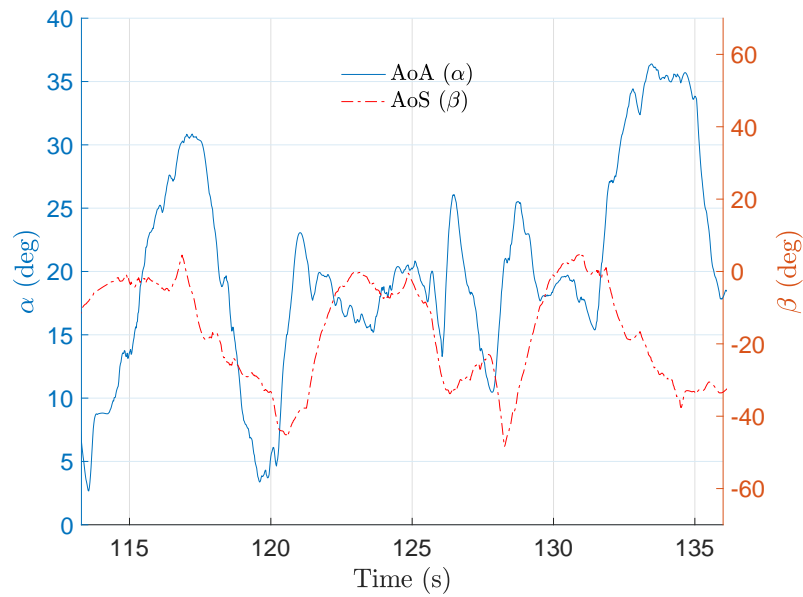

FIGURE 5.17: AoA and AoS of the $10\,\text{m}^2$ kite during the *steering maneuver*.

5.2 Results of the flight testing

In the following, the results of two flight campaigns, one with the $10\,\text{m}^2$ LEI kite and one with the RFD kite are presented. In both cases, the same experimental setup was used with the only difference of the four-line/two-line configuration of the LEI

and RFD kites. In the last iteration of the experimental setup, the Pitot tube of the PixHawk2™ used in the *proof of concept* flights was substituted by an Aeroprobe™ micro Air Data System V2.0. After the findings of previous flights, the booms were mounted with an offset angle of 30° with respect to the x_K-axis in order to avoid the saturation of the instrument, and according to the range of the instrument (see Table 3.2), the experimental setup can capture AoA values from 10° to 50°.

Additionally, the experimental setup was improved with the wind station installed on the ground. The wind station has a rotary platform that is orientated to the wind by means of a wind vane, and provides the S_V projection of the Earth magnetic field ($\tilde{\boldsymbol{B}}_V$), the angular velocity of the vane ($\omega = \tilde{r}_V z_V$), and the wind flow static and dynamic pressures (p_s, p_d) measured by a PixHawk2™ hardware equipped with a Pitot tube.

5.2.1 Experimental results for the LEI kite

The quantity and quality of the flight data obtained with the LEI kite are limited because, beside the changes introduced to improve the handling qualities of the kite, difficulties arose to fly the kite in cross-wind conditions and with high airspeed and tether tensions. These difficulties are intrinsic to the low cost experimental setup, which involves relatively short tether lengths and, due to limitations related to the load cells and the manual control system of the kite, it should operate with low wind speeds and within relatively small flying windows. Other experimental setups do not exhibit these issues and low AoA (around 10°) were measured by performing figure-eight trajectories in cross-wind conditions with a bigger size LEI kite[72]. Since figure-eight maneuvers could not be performed, the LEI kite flew in post-stall conditions most of the time and, around one minute after take-off, the kite crashed and the multi-hole Pitot tube was damaged. This triggered the experimental activities with the RFD kite that, as shown in Sec. 5.2.2, were carried out successfully and with a new Pitot tube. However, some interesting records about the aerodynamics of the LEI kite were obtained before the accident and deserve attention.

Fig. 5.18 shows the projection of the trajectory in the $x_E - y_E$ plane where, for convenience, the horizontal and vertical axes correspond to the crosswind and downwind directions. The takeoff happened at the left side of the wind window and the kite flew from one side to the other several times until it crashed at the right side of the window. As shown in panels (a) and (b) of Fig. 5.19, the tensions at the front lines were low (below 200 N) and the AoA measured by the Pitot tube was saturated most of the time. Such experimental evidence demonstrates that the AoA of the LEI kite was higher that 50°. However, during the pass that lasted from time 38.5 s to 40.3 s, the velocity of the kite was large enough to produce a high tether tension (above 500 N). The Pitot tube measured an AoA that varied from 35° to 50° and the AoS decreased from 15° to −6°. The data obtained by the sensors during this interesting maneuver, which is highlighted with red color in panels (a) and (c), were used to feed the FPR algorithm and get an estimation of the full state vector of the kite.

At the beginning of the selected maneuver, the kite was at a quasi-stationary state in the left corner of the wind window and had a positive roll angle of 50°. The weight of the kite and the tensions of the lines were mainly counter balanced by the lift and, to a lesser extent, by a (negative) aerodynamic lateral force. After the pilot pulled the right control line, the kite moved towards the zenith, while increasing its airspeed and altitude. The roll angle and the AoS decreased and became negative.
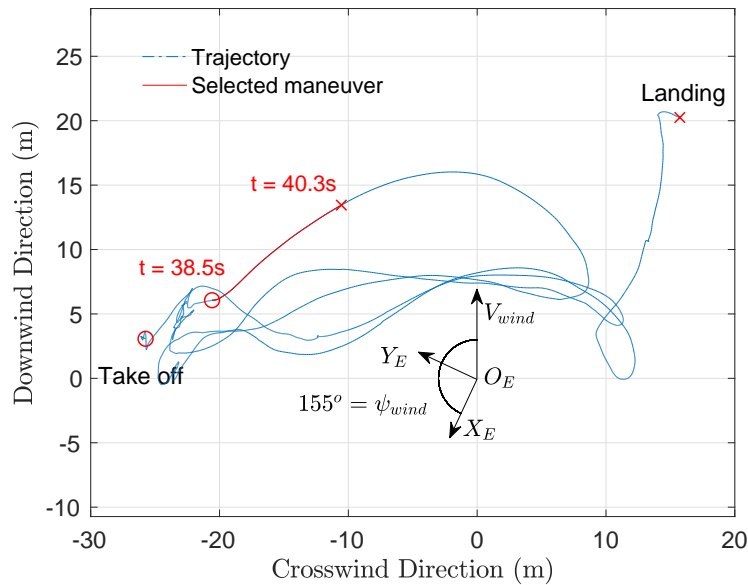

FIGURE 5.18: Trajectory of the LEI kite.

Figures 5.20 and 5.21 display quantitative results provided by the FPR algorithm during the maneuver. As shown in panel (a) of Fig.5.20, the TAS increased monotonically and reached a maximum of around 15 m/s. This feature explains the strong peak exhibited by the tensions of the front lines of panel (a) in Fig. 5.19. The lift coefficient decreased from around 1 to below 0.5 because the kite was in post-stall conditions (see panel b). The AoA at the beginning of the maneuver was 35°, and it increased up to 50°, when the sensor was saturated. Such a feature is highlighted in Fig. 5.21, which shows the value of C_L versus α provided by the FPR algorithm and exhibits the typical post-stall behavior. Unlike the lift coefficient, the variation of the drag coefficient was moderate. Its value at the beginning of the maneuver was around 0.06, reached a maximum of 0.25, and went down to 0.1. Regarding the lateral force coefficient, its behavior is consistent with the low AoS measured by the sensor. Initially C_Y was negative, as expected for the positive AoS measured by the Pitot tube, and then it changed its sign when the AoS varied from 15° to −6°. Its absolute value remained small during the full maneuver.
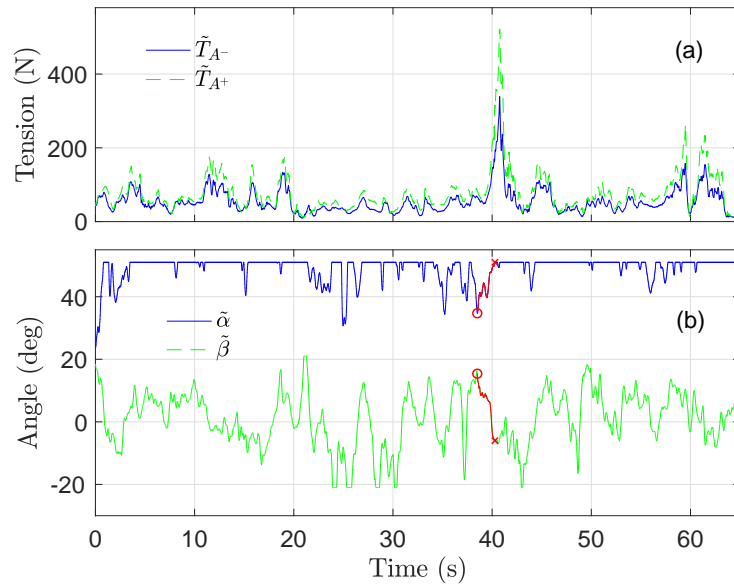
FIGURE 5.19: Tension at the front lines (a), and AoA measured by the Pitot tube (b).
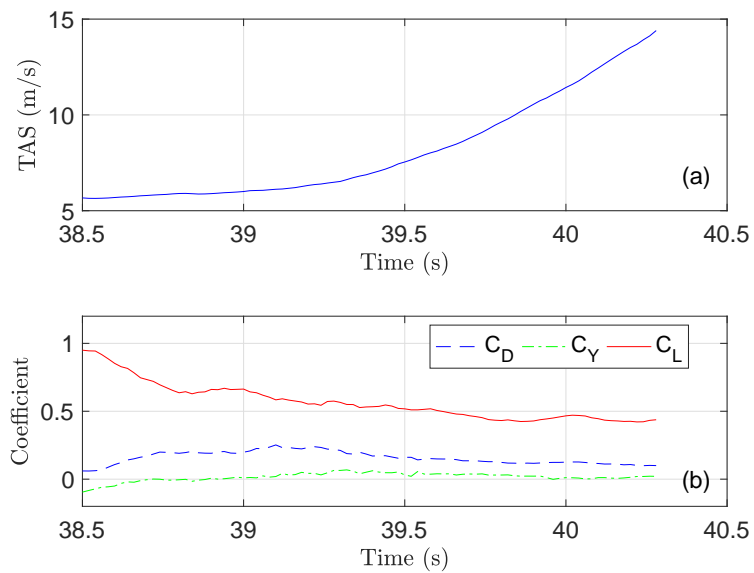

FIGURE 5.20: Time evolution of the TAS (a) and the aerodynamic coefficients (b) of the
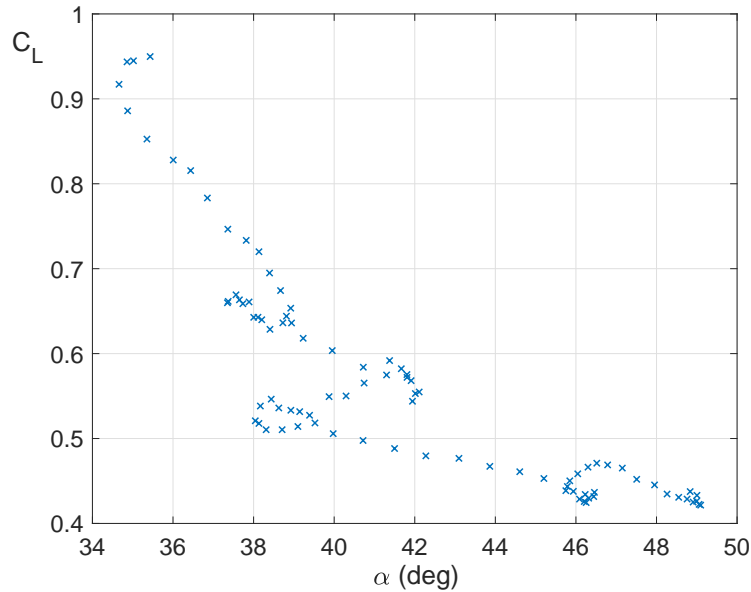LEI kite.

FIGURE 5.21: Lift coefficient versus angles AoA of the LEI kite.

5.2.2 Experimental results for the RFD kite

Since its maneuverability was excellent, abundant flight data were obtained for the RFD kite. Figure 5.22 shows the projection of the kite trajectory in the horizontal plane (blue dashed line). After the take-off, which happened in the downwind direction, kite pitch angle equal to 90°, and aided by an assistant who propelled the kite upwards, more than ten figure-eight trajectories were performed in the interval 20 s < t < 125 s. From t = 125 s to t = 150 s, the kite was steered to an equilibrium state close to the zenith and then a few more figure-eight trajectories of smaller amplitude were performed before the landing. In order to protect the Pitot tube, the kite was steered to the left side of the wind window slowly and an assistant grabbed it before touching the ground.

Panel (a) of Fig. 5.23 shows the evolution of the tether tensions measured by the load cells. They exhibit a high repeatability and match very well with the expected behavior. For instance, the tensions in every figure-eight maneuver has two maxima and, depending on the traveling directions of the kite (left or right), the maxima of $\tilde{T}_{A^+}$ is higher or lower than the one of $\tilde{T}_{A^-}$. As expected, the measured tension was higher when the kite flew in cross-wind condition, and lower at the equilibrium state. The AoA and AoS varied within the ranges $20° < \tilde{\alpha} < 50°$ and $-18° < \tilde{\beta} < 18°$ (panel (b)). Hereafter, we discuss the aerodynamics characteristics of the RFD kite in the selected maneuver, which is highlighted with a red solid line in Fig. 5.22 and corresponds with the figure-eight orbits in the interval 20s < t < 125s. When these trajectories are examined in the crosswind direction versus altitude plane (not shown), straight and turning segments are identified.
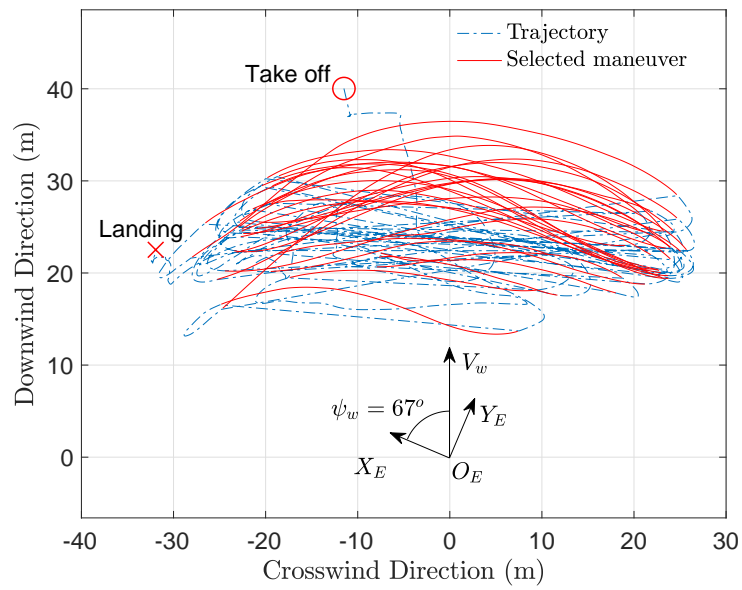
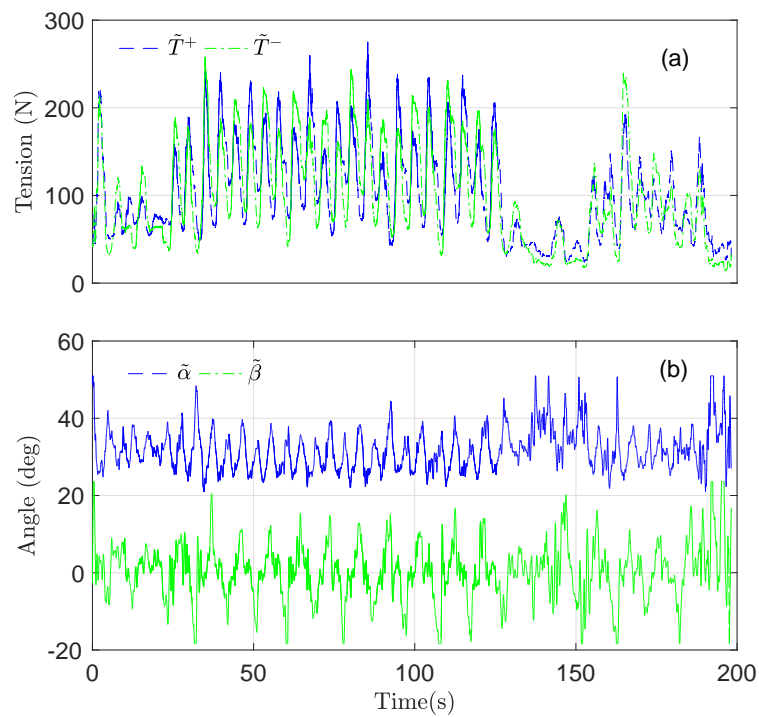FIGURE 5.22: Trajectory of the RFD kite.

FIGURE 5.23: Tension at the front lines (a), and AoA measured by the Pitot tube (b).

Panels (a)-(b) in Fig. 5.24 show in detail the evolution during four figure-eight selected maneuvers of the TAS and the AoA measured by the sensors and estimated by the FPR algorithm respectively. The estimated TAS and AoA are in good agreement with the air data computer raw measurements.
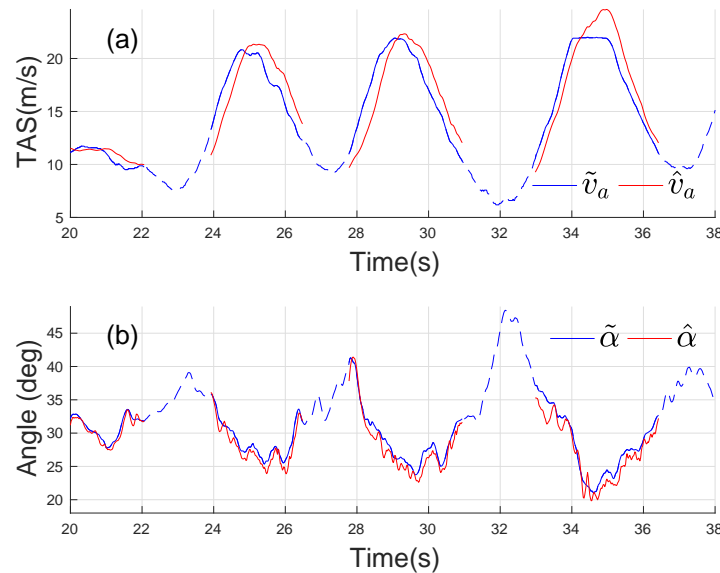

FIGURE 5.24: Evolution of the TAS (panel (a)) and estimated AoA (panel(b)).

From $t = 34$ s to $t = 35$ s, the TAS measurement was saturated but the filter is still capable of reconstructing the kite aerodynamic speed, thus showing the robustness of the FPR algorithm. On the other hand, panels (a)-(d) in Fig. 5.25 display the aerodynamic coefficients provided by the FPR algorithm. The solid lines correspond to the selected straight segments, while the dashed lines correspond to the turns. The maxima (minima) of the TAS, which are reached during the straight (turning) segments, coincide in time with the maxima (minima) of the tether tensions in the panel (a) of Fig. 5.23. When the TAS exhibits a maximum (minimum), the lift and the drag coefficients have a minimum (maximum) because the AoA decreases as the TAS increases in the straight segments. The time histories of these variables are smooth and have a high repeatability. The pitch moment coefficient (C_m) is small and negative for most of the flight. The lateral force coefficient (C_Y) is also small and, as expected due to the time history of the AoS, it changes its sign periodically.

For the straight segments of the figure-eight maneuvers there are abundant data and, as the tensions are high, they are also expected to be the most reliable information to identify the aerodynamic parameters of the kite. For this particular set of data, a statistical analysis of the lift and drag coefficients was carried out by using box plots (Fig. 5.26). In these diagrams, the horizontal and central line of the box represents the

median. The bottom and top edges indicate the 25th and 75th percentiles. The outliers are denoted with crosses and two vertical lines indicate the remaining data outside the central box that are not outliers. Data were gathered by AoA (intervals of width equal to 1 degree) and we made three different groups for the AoS: $| \beta | < 3$, $3 < | \beta | < 6$, and $6 < | \beta | < 9$. Panels (a)-(c) show the lift coefficient versus the angle of attack for these three groups of AoS. The fitting of the medians to a straight line gives the slops $C_{L\alpha} = 2.83, 2.42$ and 2.38 for $| \beta | < 3$, $3 < | \beta | < 6$, and $6 < | \beta | < 9$, respectively. These values are below the typical value for low-speed attached-flow lift-curve slope that, for an aspect ratio (AR) of 7, is around 4 (see Fig. 5 in Ref. [64]). The analysis of the drag coefficient (see panels (d)-(f)), besides showing the expected growth of C_D with C_L, highlights the important drag produced by the kite. For instance, for $C_L = 1$ one has $C_D \approx 0.4$ and the induced drag predicted by the lifting-line theory is only around $C_L^2/\pi A R e \approx 0.057$ for $AR = 7$ and a planform efficiency factor of $e = 0.8$. We finally mention that a similar analysis was carried out to study the behavior of the pitch moment coefficient (C_m) when the angle of attack is varied (not shown). The slope of the curve was around $C_{m\alpha} \approx -0.05$. A direct application of this identification of the aerodynamic parameters is the improvement of the aerodynamic model in two-line kite flight simulators[85].
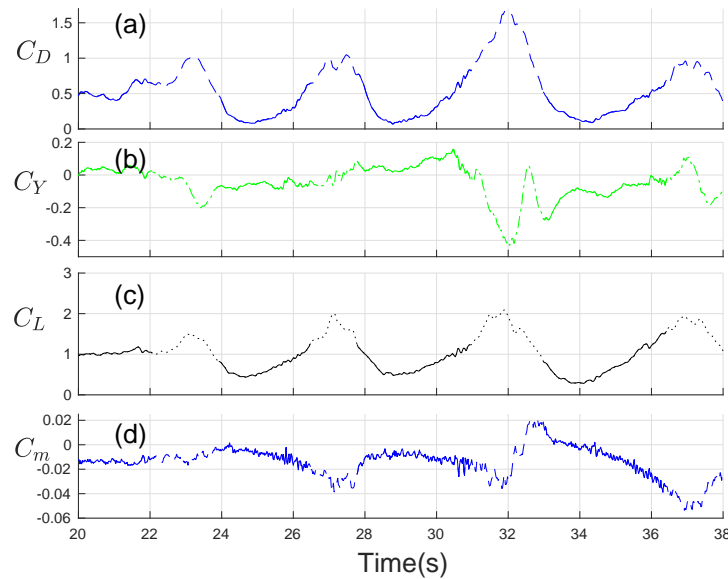

FIGURE 5.25: Evolution of the aerodynamics coefficients of the RFD kite during the figure-eight maneuvers.

There are some interesting features in Figs. 5.25 and 5.26 that require complementary analysis using computational fluid dynamics techniques. Even during the straight

segments of the figure-eight maneuver, the kite does not fly in steady conditions because, beside wind fluctuations, the angular velocity does not vanish. This fact can explain the dispersion observed in some data of Figs. 5.25 and 5.26. Moreover, previous comments about $C_{L\alpha}$ and C_D, and the high AoA measured during the flight, indicate that linear aerodynamic theories do not hold. For instance, the C_L versus α diagrams show that C_L grows monotonically even after reaching a high AoA. This may be due to nonlinear aerodynamic effects. It is well-known that the typical angle of attack for maximum lift of a delta wing with low aspect ratio can be much higher (around 40°) than for a two-dimensional airfoil due to the presence of two vortices [59]. The convex curvature of the flow near the leading edge produces a suction that increases the C_L. However, although panels (a)-(c) show a positive $C_{L\alpha}$ even at AoA around 40°, the results for low aspect ratio wings cannot be directly applied to our kite because it has an AR = 7. Unsteady aerodynamic effects, like dynamic stall, can also increase the C_L and delay conventional flow separation on wings beyond the static stall angle.
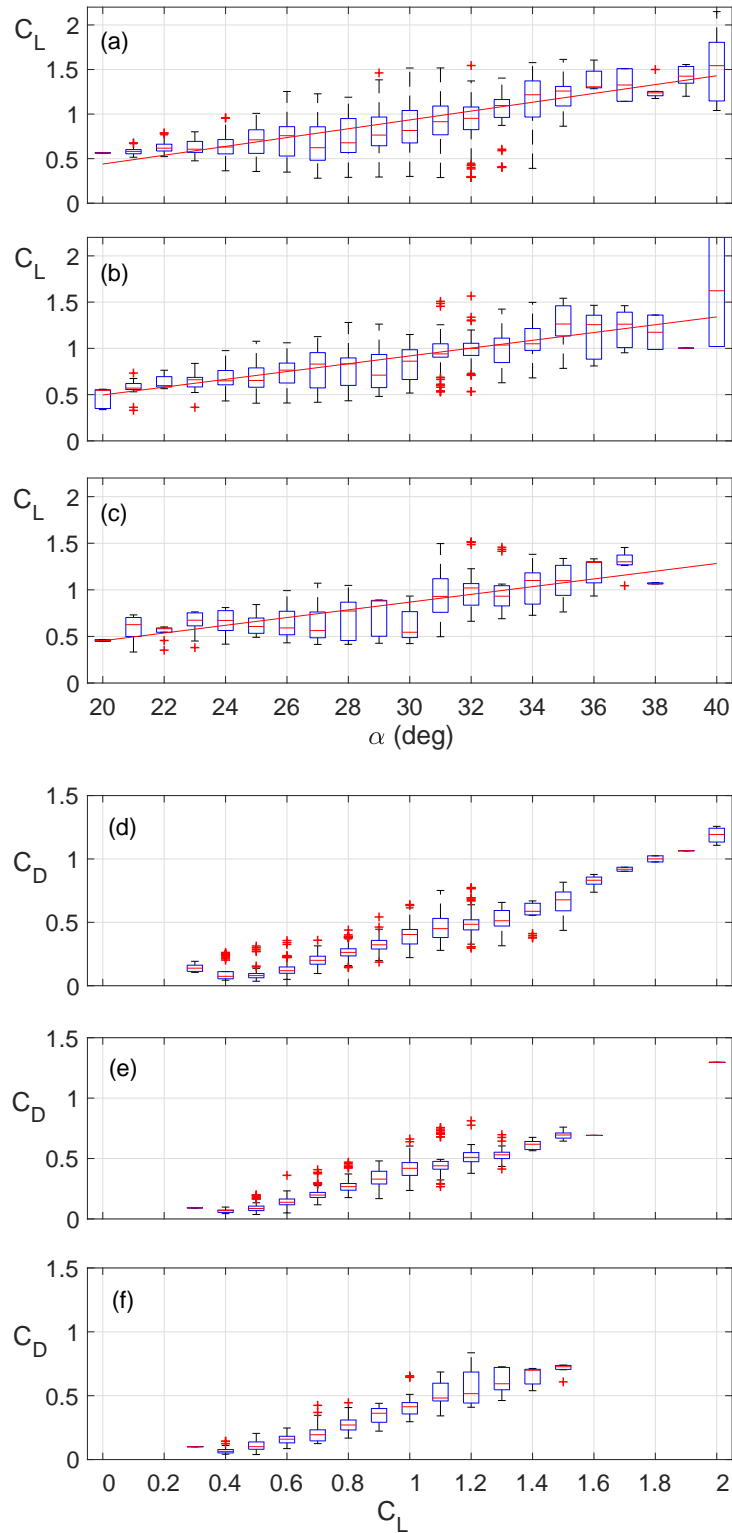
FIGURE 5.26: Lift coefficient versus angle of attack (panels (a)-(c)) and drag coefficient versus lift coefficient (panels (d)-(f)). The AoS was filtered within the ranges $|\beta| < 3$ (panels (a) and (d)), $3 < |\beta| < 6$ (panels (b) and (e)) and $6 < |\beta| < 9$ (panels (c) and (f)).

6 CONCLUSIONS AND FUTURE WORK

Although important efforts have been made in the last few years by using computational fluids dynamics and experimental methods, trustworthy and complete aerodynamic models of aircraft used in AWE applications are not yet available. This thesis proposed the use of the Estimation Before Modeling (EBM) technique for the aerodynamic characterization of AWES based on experimental flight data.

The EBM is a two-steps method. Firstly, the state vector of the aircraft during the whole flight is reconstructed in the so called *estimation* or *Flight Path Reconstruction* (FPR) phase. This state vector includes, aside from the generic state variables (i.e. position, velocity or attitude) the aerodynamic forces and torques. The aerodynamic coefficients are derived a-posteriori from the reconstructed forces, torques, and the other state variables. In the second step (*modeling* phase), a mathematical model is fitted to the reconstructed aerodynamic coefficients. The biggest advantage of the EBM technique is that both phases are independent, and the *modeling* phase becomes a model fitting problem isolated from the aircraft equations of motion. Consequently, different mathematical model structures and model fitting techniques can be used without the need to reformulate the system process model.

To demonstrate the application of the EBM technique to tethered aircraft, an ad-hoc experimental setup has been developed together with a flight testing methodology for kites. Several flight tests have been carried out and the EBM technique has been applied to the obtained measurements. A conservative approach has been applied during this thesis work. Firstly, a simpler experimental setup was developed with low-cost commercial of the shelf (COTS) hardware and a four-line, leading edge inflatable (LEI) surf-kite. The obtained data was used to validate a first version of a FPR algorithm and reconstruct the full state vector of the kite. After the first flights were concluded and the FPR algorithm was validated, conclusions on the required experimental setup improvements were obtained and implemented. The FPR algorithm was then updated and reformulated to be used also with two-line rigid frame delta (RFD) kites and the reconstructed aerodynamic forces and torques were used to provide some characteristics of the aerodynamic behavior of both LEI and RFD kites.

6.1 Lessons learned from the first flight tests

The proposed experimental setup and FPR algorithm were firstly validated with data recorded with both, the $13\,\mathrm{m}^2$ and $10\,\mathrm{m}^2$ LEI kites. After analyzing the obtained measurements, it was determined that the selected sensors were working within their expected measurement ranges and the provided data could be used to reconstruct the space state trajectory of the kites. However, the static and dynamic pressure signals

from the onboard pitot tube were found to be heavily noisy and biased, and the need for a new sensor was concluded.

Additionally, some of the reconstructed state variables, such as the kite attitude and the kite trajectory, were compared with the outputs of an independent estimator provided by the software Px4™ and showed in good agreement. Two basic control maneuvers were studied to validate the coherence of the reconstructed state vector of the kite, a *pull-up maneuver* and a *steering maneuver*. In both cases the kinematics of the kites were in good agreement with the command inputs from the control-bar, showing coherent correlation between the kite attitude, angular rates and kite ground position and velocity. During this maneuver, the reconstructed behavior of the aerodynamic forces and torques showed coherent with the evolution of the kite attitude and aerodynamic speed.

This validation allowed us to conclude that the FPR algorithm produced coherent results. However, the poor performance of the onboard dynamic and static pressure sensors, together with the lack of direct measurements during the flight of the wind direction and speed, and the kite attitude within the airflow, resulted in the uncertainness of the a-posteriori reconstructed air-data (angle of attack (AoA), angle of side slip (AoS) and aerodynamic speed (TAS)). In particular, the estimated AoA resulted abnormally high during the studied maneuvers in comparison with conventional aircraft and other published studies with bigger LEI kites. In order to verify these findings and to increase the overall precision of the FPR algorithm, it was learned that the experimental setup should provide direct measurements of the kite AoA and AoS, and the wind state vector. From the experience obtained during these flight campaigns, it was also concluded that i) the handling qualities of the kites equipped with the required onboard sensors were heavily affected due to the added payload and the modification of the kite CoG location and ii) the COTS control bar instrumented with load-cells and distance sensors showed particularly intrusive as the weight of the load-cells inserted in the control lines heavily affected the controllability of the kite, resulting even in the kite stalling and crashing when flying in wind lulls.

The final version of the experimental setup was designed to address the observed limitations during the *proof of concept* flight tests and included a new control bar, a ground wind station, a high precision multi-hole pitot tube and a new RFD kite. Two flight campaigns were performed with the new experimental setup, one with the $10\,\text{m}^2$ LEI kite and one with the RFD kite. These flight campaigns provided quantitative and qualitative results about the aerodynamic characteristics of both type of kites, and revealed significance differences among them.

6.2 Final flight testing conclusions

After the last flight campaign with the $10\,\text{m}^2$LEI kite, we can conclude that the flying qualities of the kite are still far from ideal due to the forwarded location of it's CoG. In an effort to minimize this effect and to increase the flight safety, this campaign was

carried out in the coast of Huelva, looking for steadier sea winds in comparison with the gusty ones found in Madrid. However, the LEI kite crashed only 65 s after launch, and one of the multi-hole pitot tubes was destroyed. Unfortunately, the amount and quality of the recorded data was limited. From the direct measurements of the calibrated pitot tube and air-data computer, we can confirm that the LEI kite flew most of the time with an AoA greater than 50°. This measurement corroborates the reconstructed AoA of the first proof of concept flights and further validates the integrity of the FPR algorithm. The observed AoA constitutes a big difference with other works carried out with much bigger LEI kites during power producing flights.

A 2 s long maneuver could be identified within the flight in which the kite flew a crosswind trajectory with higher TAS and lower AoA. During this maneuver, the AoA sensor was not saturated, and the recorded data was used to feed the FPR algorithm. A comparison of the reconstructed lift coefficient (C_L) with the kite AoA showed an inverse relation among them. It has been concluded that this effect is coherent with a post-stall aerodynamic behavior of the wing, and differs from the observed behavior of large power-producing LEI kites.

The flight campaign with the RFD kite showed excellent handling qualities of the kite, and close to the behavior of the *clean* kite, rewarding the efforts done to keep the original CoG location. This allowed the pilot to perform a 200 s long flight without any incident and provided abundant and quality data for the FPR algorithm. The adaptation of the FPR algorithm to the two-line kites was also validated. As with the LEI kites, the kinematics of the kite showed coherent during the flight. Four figure-eight maneuvers were selected to study the aerodynamic characteristics of the kite. The C_D, C_Y, C_L and C_m coefficients were reconstructed and a statistical analysis of the reconstructed coefficients was carried out. From this analysis, we can conclude that the kite had a diminished aerodynamic performance in comparison with theoretical models of an equivalent wing with the same aspect ratio. For such a wing, and a low-speed attached-flow, a lift-curve slope $C_{L\alpha} = 4$ was expected, while an average $C_{L\alpha} = 2.54$ was obtained. On the other hand, the induced drag predicted by the lifting-line theory is only around $C_L^2/\pi A R e \approx 0.057$ for $AR = 7$ and a plan form efficiency factor of $e = 0.8$, versus the obtained $C_D \approx 0.4$.

Albeit smaller AoA were registered during the flight of the RFD kite in comparison with the LEI kite, the magnitude of the estimated AoA was still significantly high. However, opposite to the LEI kite, the RFD kite lift coefficient did not show a post stall behavior (the C_L versus α diagrams show that C_L grows monotonically even after reaching an AoA higher than 30°). This may be due to nonlinear aerodynamic effects, in which the convex curvature of the flow near the leading edge produces a suction that increases the C_L.

6.3 Future work

The activities carried out in this thesis work have resulted in an experimental setup, flight testing methodology, and FPR algorithm, capable of reconstruct the time histories of the state variables of a tethered aircraft flying crosswind trajectories. The reconstructed variables include the generated aerodynamic forces and torques, and from them, the aerodynamic coefficients of the aircraft are derived. A general overview of the obtained results during this thesis work, as well as the applications and future activities which can be derived from them, is given in Table. 6.1.

Results	Applications	Future Activities
Experimental Setup	**AWE systems flight testing:** Easily portable to power producing systems.	Application to power-producing systems such as Kitepower B.V
	Research activities: Further research on kites aerodynamics and flight dynamics can be performed.	Further integration of experimental measurements with analytical methods such as Unsteady Panel Methods (UPM)
	Academic applications: The developed methods and experimental setup are a used as a test bed for academic education in the fields of flight dynamics, control, aerodynamics, mechanical design or electronic design.	In-flight research of kites post-stall behaviour.
		On-board recording of the kite boundary layer separation
		Improvement of the experimental setup mechanics for increased accuracy and maximum supported loads.
FPR algorithm	**Aerodynamic characterization of AWEs:** Improve power-producing systems performance due to better modeling and characterization.	Improvement of the FPR algorithm with a tether model, increasing the algorithm accuracy, specially for bigger systems with longer tethers.
	Advanced space-state estimator: Complete state vector estimation for tethered aircraft allows for the development of advance Flight Control Systems for AWEs	Integration of newer sensors such as, ground based tracking cameras or RTK GPS for increased accuracy.
		Real time transmission of sensors measurements to a ground station
		Development of a real time version of the FPR algorithm allowing for close-loop control of the kite.

TABLE 6.1: Project results with its applications and future activities.

Although significant qualitative and quantitative results were obtained for two different typologies of tethered aircraft, a full aerodynamic model could still not be provided. The model-fitting methodology proposed by Eugene A. Morelli, to provide a generic aerodynamic model given a set of reconstructed aerodynamic coefficients and state variables, was preliminary tested with the RFD kite data. However, sounding results could not be obtained and have not been presented. In particular, the optimization function used by Morelli to determine the optimal number of independent orthogonal functions to be included into the aerodynamic model, did not provide a clear minima for our experiment. Additionally, when applied to different subsets of data, the obtained model was not repetitive. These results may be explained by the post-stall and/or no-linear behavior of the kite, together with the flexible nature of the textile canopy (even for the RFD kite), which makes obtaining an aerodynamic model much harder than for

a conventional aircraft.

Nevertheless, the developed experimental setup presented limitations to represent big sized LEI kites like the ones used for power generation, mainly related with the maximum acceptable generated tensions, and the limited size of the *flying window* and consequently of the crosswind trajectories. Major differences on the measured AoA were found with third parties studies. Finally, manual control of the kite by a human pilot through a control bar, and the load-cells installation inline with the tethers, introduced measurements errors and uncertainness, as it was assumed in the FPR algorithm that the front lines and the control bar were always contained in the same plane, which cannot be guaranteed in practice in this setup.

The presented experimental setup and flight testing methodology have played a distinctive role in UC3M *Tethered Aerospace System and Airborne Wind Energy Group*. Related academic activities of the group have resulted in multiple publications in JCR indexed journals, conference presentations and nine Bachelor and Master Theses. Future work in the application of EBM techniques to tethered aircraft like the ones used in AWEs, may tackle three main aspects:

1. Validate the described aerodynamic behavior with bigger LEI kites flying bigger and wider crosswinds trajectories. The application of the described instrumentation to an AWE system, such as Kitepower B.V system, could provide valuable information about the aerodynamic characteristics of power-producing kites. This information could be used to improve our knowledge of some aerodynamic coefficients which are key when modeling the system performance or to improve the kite control system. Additionally, the multivariate orthogonal functions method described by Morelli can be tested to provide a full aerodynamic model.

2. Improving the experimental setup towards a mechanical (fly-by-wire) system which eliminates de manual inputs to the system. This new setup should be able to stand higher loads on the tethers, allowing for faster and wider crosswind trajectories, while at the same time eliminating the uncertainness introduced in the measurements by the manual control bar.

3. Improving the FPR algorithm with a tether model, which will allow to introduce the sag of the tether in the filter process model. This will provide a better projection of the tether tensions over the aircraft body-axes and will further improve the precision of the EKF, specially if wider trajectories are studied, in which the straight line approach for the tether can not be hold.

Some of the described tasks, particularly the improvement of the experimental setup towards fly-by-wire operation, are currently ongoing in the UC3M GreenKite-2 project [43].

A ESTIMATOR DESCRIPTION

In this appendix, explicit formulations for the observation and process models of the FPR EKF are provided. This models are derived for both, the four lines LEI kites, and the two lines RFD kites. Before the observation model ($h(x)$), that maps the observation vector ($\tilde{y}$) with the EKF state vector (x) can be derived, we must introduce,

- The rotation matrix that relates the S_E and S_K vector components, as a function of the kite Euler angles (ϕ, θ and ψ),

$$\bar{R}_{EK} = \begin{pmatrix} c\psi c\theta & c\psi s\theta s\phi - s\psi c\phi & c\psi s\theta c\phi + s\psi s\phi \\ s\psi c\theta & s\psi s\theta s\phi + c\psi c\phi & s\psi s\theta c\phi - c\psi s\phi \\ -s\theta & c\theta s\phi & c\theta c\phi \end{pmatrix} \quad (A.1)$$

  where $s\alpha$ and $c\alpha$ stands for the sin and cosine of whatever angle α.

- B_o, is the S_E projection of the Earth magnetic field in the flight testing location and flight data as modeled by the World Magnetic Model (WMM) [95].

- The kite mass, m_K, and inertia tensor about its center of mass $\bar{I}_{O_K}$.

- The gravitational constant, g.

- The S_K projection of the kite aerodynamic velocity ($v_a = [u_a \ v_a \ w_a]$) as measured by the multi-hole pitot tube, can be calculated as a function of the EKF state variables as,

$$v_a = v + \omega \times \overline{O_K P} - \bar{R}_{EK}^T \begin{pmatrix} \cos\psi_{w1} \\ \sin\psi_{w1} \\ 0 \end{pmatrix} V_{w1} \quad (A.2)$$

  where $\overline{O_K P}$ is a vector with origin at the kite CG and tip at the pitot inlet, and its modulus equals to the distance from the kite CG to the $\tilde{\alpha}$, $\tilde{\beta}$ and $\tilde{v}_a$ sensing point.

- The rotation matrix, $\bar{R}_{EV}$, that relates the S_E and S_V vector components. It must be denoted that k_V is always parallel to k_E, and i_V points to the wind. Then, the rotation angle of the S_V body axis with respect to the S_E reference frame (ψ_V), is related with the wind direction state variable as, $\psi_V = \psi_{w1} + \pi$. Finally,

$$\bar{R}_{EW} = \begin{pmatrix} c(\psi_{w1} + \pi) & -s(\psi_{w1} + \pi) & 0 \\ s(\psi_{w1} + \pi) & c(\psi_{w1} + \pi) & 0 \\ 0 & 0 & 1 \end{pmatrix} \quad (A.3)$$

- The distance $\tilde{D}$ between the kite attaching point on the ground (O_E) and its CG. $\tilde{D}$ is constant and equal to $L_s + \sqrt{L_l^2 - y_{A^\pm}^2}$, where the small distance between the location of the IMU and O_K was neglected, and the distance $y_{A^\pm}$ between the attachment point $A^\pm$ and the plane of symmetry of the kite was introduced.

- For the four lines LEI kites, the projection of the vector $\overline{O_E O_K}$ along the $\boldsymbol{j}_K$-kite body axis, $\tilde{P}_{j_K}$, is a constant and equals zero.

A.1 Four lines LEI kites

The state vector of the EKF is,

$$
\begin{aligned}
\boldsymbol{x} = \big[\boldsymbol{r} \ \ \boldsymbol{v} \ \ \boldsymbol{\Upsilon} \ \ \boldsymbol{\omega} \ \ \boldsymbol{\Theta}_B \ \ \boldsymbol{\Theta}_{B_V} \ \ \boldsymbol{\Theta}_f \ \ \boldsymbol{\Theta}_\omega \ \ \Theta_{V_w} \ \ \Theta_{r_V} \\
\boldsymbol{F}_{a_1} \ \ \boldsymbol{M}_{a_1} \ \ T_{A^+_1} \ \ T_{A^-_1} \ \ T_{B^+_1} \ \ T_{B^-_1} \ \ V_{w_1} \ \ \psi_{w_1} \\
\boldsymbol{F}_{a_2} \ \ \boldsymbol{M}_{a_2} \ \ T_{A^+_2} \ \ T_{A^-_2} \ \ T_{B^+_2} \ \ T_{B^-_2} \ \ V_{w_2} \ \ \psi_{w_2} \\
\boldsymbol{F}_{a_3} \ \ \boldsymbol{M}_{a_3} \ \ T_{A^+_3} \ \ T_{A^-_3} \ \ T_{B^+_3} \ \ T_{B^-_3} \ \ V_{w_3} \ \ \psi_{w_3} \big]^T
\end{aligned}
\tag{A.4}
$$

where $\boldsymbol{x}$ is a 62×1 column vector containing, the S_E-components of the kite position vector ($\boldsymbol{r}$), the S_K-components of the kite absolute velocity ($\boldsymbol{v}$) and angular velocity ($\boldsymbol{\omega}$), its roll, pitch, and yaw angles ($\boldsymbol{\Upsilon} = [\phi \ \theta \ \psi]$), the error model biases ($\boldsymbol{\Theta}_B$, $\boldsymbol{\Theta}_f$, $\boldsymbol{\Theta}_\omega$, Θ_{V_w}, Θ_{r_V} and $\boldsymbol{\Theta}_{B_V}$) for the onboard the kite measured magnetic field, specific force and angular rates, the on the wind-station measured wind speed, yaw angular rate and magnetic field ($\tilde{\boldsymbol{B}}_V$), plus the three pseudo states for the S_K-components of the aerodynamic force and moment about the kite center of mass ($\boldsymbol{F}_{a_i}$ and $\boldsymbol{M}_{a_i}$), the magnitudes of the tether tensions ($T_{A_i^\pm}$, $T_{B_i^\pm}$) and the magnitude of the wind velocity V_{w_i} and its heading angle ψ_{w_i}.

And the observation vector of the EKF is,

$$
\tilde{\boldsymbol{y}} = \big[\tilde{\boldsymbol{B}} \ \ \tilde{\boldsymbol{v}} \ \ \tilde{\boldsymbol{r}} \ \ \tilde{\boldsymbol{f}} \ \ \tilde{\boldsymbol{\omega}} \ \ \tilde{v}_a \ \ \tilde{\alpha} \ \ \tilde{\beta} \ \ \tilde{T}_{A^+} \ \ \tilde{T}_{A^-} \ \ \tilde{T}_{B^+} \ \ \tilde{T}_{B^-} \ \ \tilde{\boldsymbol{B}}_V \ \ \tilde{r}_V \ \ \tilde{V}_w \ \ \tilde{D} \ \ \tilde{P}_{y_k} \big]^T
\tag{A.5}
$$

where $\tilde{\boldsymbol{y}}$ is a $29x1$ column vector and includes, the S_K-components of the onboard the kite measured Earth magnetic field ($\tilde{\boldsymbol{B}}$), the S_E-components of the measured position and velocity vectors of the kite ($\tilde{\boldsymbol{r}}$ and $\tilde{\boldsymbol{v}}$), the S_K-components of the measured angular rates and specific force ($\tilde{\boldsymbol{f}}$, $\tilde{\boldsymbol{\omega}}$), the measured magnitude of the kite true airspeed ($\tilde{v}_a$) the AoA and the AoS ($\tilde{\alpha}$ and $\tilde{\beta}$), the four magnitudes of the measured tether forces ($\tilde{T}_{A^\pm}$ and $\tilde{T}_{B^\pm}$), the S_V-components of the wind-station measured Earth magnetic field ($\tilde{\boldsymbol{B}}_V$), and the measured wind yaw angular rate ($\tilde{r}_V$) and wind true airspeed ($\tilde{V}_w$).

A.1.1 Observation Model

The explicit form of the observation model $\tilde{\boldsymbol{y}} = \boldsymbol{h}(\boldsymbol{x}) + \boldsymbol{\eta}$, can be written as

$$
\tilde{\boldsymbol{B}} = \bar{\boldsymbol{R}}_{EK}^T \boldsymbol{B}_0 + \boldsymbol{\Theta}_B + \boldsymbol{\eta}_B \qquad\qquad\qquad \boldsymbol{\eta}_B \in N(0, \sigma_{\eta_B}^2)
$$

$$\tilde{\boldsymbol{v}} = \bar{\boldsymbol{R}}_{EK}\boldsymbol{v} + \boldsymbol{\eta}_v \qquad \boldsymbol{\eta}_v \in N(0, \sigma_{\eta_v}^2)$$

$$\tilde{\boldsymbol{r}} = \boldsymbol{r} + \boldsymbol{\eta}_r \qquad \boldsymbol{\eta}_r \in N(0, \sigma_{\eta_r}^2)$$

$$\tilde{\boldsymbol{f}} = \frac{1}{m_k}\left[\boldsymbol{F}_{a1} + \sum_{i=\pm}(\boldsymbol{T}_{A^i} + \boldsymbol{T}_{B^i})\right] + \boldsymbol{\Theta}_f + \boldsymbol{\eta}_f \qquad \boldsymbol{\eta}_f \in N(0, \sigma_{\eta_f}^2)$$

$$\tilde{\boldsymbol{\omega}} = \boldsymbol{\omega} + \boldsymbol{\Theta}_\omega + \boldsymbol{\eta}_\omega \qquad \boldsymbol{\eta}_\omega \in N(0, \sigma_{\eta_\omega}^2)$$

$$\tilde{v}_a = |\boldsymbol{v}_a| + \eta_{v_a} \qquad \eta_{v_a} \in N(0, \sigma_{\eta_{v_a}}^2)$$

$$\tilde{\alpha} = \arctan\left(\frac{w_a}{u_a}\right) + \eta_\alpha \qquad \eta_\alpha \in N(0, \sigma_{\eta_\alpha}^2)$$

$$\tilde{\beta} = \arcsin\left(\frac{v_a}{|\boldsymbol{v}_a|}\right) + \eta_\beta \qquad \eta_\beta \in N(0, \sigma_{\eta_\beta}^2)$$

$$\tilde{T}_{A^+} = T_{A_1^+} + \eta_{T_{A^+}} \qquad \eta_{T_{A^+}} \in N(0, \sigma_{\eta_T}^2)$$

$$\tilde{T}_{A^-} = T_{A_1^-} + \eta_{T_{A^-}} \qquad \eta_{T_{A^-}} \in N(0, \sigma_{\eta_T}^2)$$

$$\tilde{T}_{B^+} = T_{B_1^+} + \eta_{T_{B^+}} \qquad \eta_{T_{B^+}} \in N(0, \sigma_{\eta_T}^2)$$

$$\tilde{T}_{B^-} = T_{B_1^-} + \eta_{T_{B^-}} \qquad \eta_{T_{B^-}} \in N(0, \sigma_{\eta_T}^2)$$

$$\tilde{\boldsymbol{B}}_V = \bar{\boldsymbol{R}}_{EV}^T\boldsymbol{B}_0 + \boldsymbol{\Theta}_{B_V} + \boldsymbol{\eta}_{B_V} \qquad \boldsymbol{\eta}_{B_V} \in N(0, \sigma_{\eta_{B_V}}^2)$$

$$\tilde{r}_V = \gamma_{\psi_{w_1}}\psi_{w_2} + \boldsymbol{\Theta}_{r_V} + \eta_{r_V} \qquad \eta_{r_V} \in N(0, \sigma_{\eta_{r_V}}^2)$$

$$\tilde{V}_w = V_{w_1} + \boldsymbol{\Theta}_{V_w} + \eta_{V_w} \qquad \eta_{V_w} \in N(0, \sigma_{\eta_{V_w}}^2)$$

$$\tilde{D} = |\boldsymbol{r}| + \eta_D \qquad \eta_D \in N(0, \sigma_{\eta_D}^2)$$

$$\tilde{P}_{j_K} = \boldsymbol{j}_K \cdot \bar{R}_{EK}^T\boldsymbol{r} + \eta_{P_{j_K}} \qquad \eta_{P_{j_K}} \in N(0, \sigma_{\eta_{P_{j_K}}}^2)$$

$$(A.6)$$

Then, $\boldsymbol{\eta}$, is a 29×1 column vector containing the measurements observation noises,

$$\boldsymbol{\eta} = \left[\boldsymbol{\eta}_B \ \boldsymbol{\eta}_r \ \boldsymbol{\eta}_v \ \boldsymbol{\eta}_f \ \boldsymbol{\eta}_\omega \ \eta_a \ \eta_\alpha \ \eta_\beta \ \eta_{T_{A^+}} \ \eta_{T_{A^-}} \right.$$
$$\left. \eta_{T_{B^+}} \ \eta_{T_{B^-}} \ \boldsymbol{\eta}_{B_V} \ \eta_{r_V} \ \eta_{V_w} \ \eta_D \ \eta_{P_{j_K}} \right]^T \qquad (A.7)$$

and the covariance matrix, $\bar{\boldsymbol{R}}$, is a 29×29 diagonal matrix with,

$$diag(\bar{\boldsymbol{R}}) = \left[\sigma_{\eta_B}^2 \ \sigma_{\eta_B}^2 \ \sigma_{\eta_B}^2 \ \sigma_{\eta_r}^2 \ \sigma_{\eta_r}^2 \ \sigma_{\eta_r}^2 \ \sigma_{\eta_v}^2 \ \sigma_{\eta_v}^2 \ \sigma_{\eta_v}^2 \ \sigma_{\eta_f}^2 \ \sigma_{\eta_f}^2 \ \sigma_{\eta_f}^2 \right.$$
$$\sigma_{\eta_\omega}^2 \ \sigma_{\eta_\omega}^2 \ \sigma_{\eta_\omega}^2 \ \sigma_{\eta_{v_a}}^2 \ \sigma_{\eta_\alpha}^2 \ \sigma_{\eta_\beta}^2 \ \sigma_{\eta_T}^2 \ \sigma_{\eta_T}^2 \ \sigma_{\eta_T}^2 \ \sigma_{\eta_T}^2$$
$$\left. \sigma_{\eta_{B_V}}^2 \ \sigma_{\eta_{B_V}}^2 \ \sigma_{\eta_{B_V}}^2 \ \sigma_{\eta_{r_V}}^2 \ \sigma_{\eta_{V_w}}^2 \ \sigma_{\eta_D}^2 \ \sigma_{\eta_{P_{j_K}}}^2 \right] \qquad (A.8)$$

A.1.2 Process model

The S_K-components of the resulting specific force and torque acting on the kite can be expressed as a function of the state variables as,

$$
\boldsymbol{f} = f_x \boldsymbol{i}_K + f_y \boldsymbol{j}_K + f_z \boldsymbol{k}_K \qquad = \frac{1}{m_k} \left[\boldsymbol{F}_{a1} + \sum_{i=\pm} (\boldsymbol{T}_{A^i} + \boldsymbol{T}_{B^i}) \right] \tag{A.9}
$$

$$
\boldsymbol{M} = M_x \boldsymbol{i}_K + M_y \boldsymbol{j}_K + M_z \boldsymbol{k}_K \qquad = \boldsymbol{M}_{a1} + \sum_{i=\pm} \left(\overline{O_K A^\pm} \times \boldsymbol{T}_{A^i} + \overline{O_K B^\pm} \times \boldsymbol{T}_{B^i} \right) \tag{A.10}
$$

where $\boldsymbol{F}_{a1}$ and $\boldsymbol{M}_{a1}$ stands respectively for the S_K projection of the kite generated aerodynamic force and moment. While $\boldsymbol{T}_{A^\pm}$ and $\boldsymbol{T}_{B^\pm}$, stands for the S_K projection of the actuating tension forces over the kite. The later can be expressed (see Chapter. 4.4.5) as a function of the state variables as,

$$
\boldsymbol{T}_{A^\pm} = - T_{A^\pm} \overline{O_E A^\pm} / | \overline{O_E A^\pm} | \tag{A.11}
$$

$$
\boldsymbol{T}_{B^\pm} = - T_{B^\pm} \overline{O_E B^\pm} / | \overline{O_E B^\pm} | \tag{A.12}
$$

And, after denoting the S_K-components of each pseudo-state (see Chapter. 4.2) for the aerodynamic forces and moments as,

$$
\boldsymbol{F}_{ai} = F_{ai_x} \boldsymbol{i}_K + F_{ai_y} \boldsymbol{j}_K + F_{ai_z} \boldsymbol{k}_K \qquad\qquad i = 1 \ldots 3 \tag{A.13}
$$

$$
\boldsymbol{M}_{ai} = M_{ai_x} \boldsymbol{i}_K + M_{ai_y} \boldsymbol{j}_K + M_{ai_z} \boldsymbol{k}_K \qquad\qquad i = 1 \ldots 3 \tag{A.14}
$$

The explicit form of the process model, $d\boldsymbol{x}(t)/dt = \boldsymbol{f}_{\text{proc}}[\boldsymbol{x}(t)] + \bar{\boldsymbol{G}} \boldsymbol{w}(t)$, can be written as,

$$
\frac{d\boldsymbol{r}}{dt} = \bar{\boldsymbol{R}}_{EK} \boldsymbol{v}
$$

$$
\frac{d\boldsymbol{v}}{dt} = \begin{pmatrix} f_x \\ f_y \\ f_z \end{pmatrix} + \bar{\boldsymbol{R}}_{EK}^T \begin{pmatrix} 0 \\ 0 \\ g \end{pmatrix} + \begin{pmatrix} rv - qw \\ pw - ru \\ qu - pv \end{pmatrix}
$$

$$
\frac{d\boldsymbol{\Upsilon}}{dt} = \begin{bmatrix} p + (q \sin \phi + r \cos \phi) \tan \theta \\ q \cos \phi - r \sin \phi \\ (q \sin \phi + r \cos \phi) \sec \theta \end{bmatrix}
$$

$$
\frac{d\boldsymbol{\omega}}{dt} = \bar{\boldsymbol{I}}_{O_K}^{-1} \begin{bmatrix} M_x - I_{xz} qp + rq \left(I_y - I_z \right) \\ M_y + I_{xz} \left(p^2 - r^2 \right) + pr \left(I_z - I_x \right) \\ M_z + I_{xz} qr + pq \left(I_x - I_y \right) \end{bmatrix}
$$

$$
\frac{d\boldsymbol{\Theta}_B}{dt} = 0
$$

$$
\frac{d\boldsymbol{\Theta}_{B_V}}{dt} = 0
$$

$$\frac{d\mathbf{\Theta}_f}{dt} = -\frac{\mathbf{\Theta}_f}{\tau_a} + \mathbf{w}_f \qquad\qquad \mathbf{w}_f \in N(0, \sigma_{w_f}^2)$$

$$\frac{d\mathbf{\Theta}_\omega}{dt} = -\frac{\mathbf{\Theta}_\omega}{\tau_\omega} + \mathbf{w}_\omega \qquad\qquad \mathbf{w}_\omega \in N(0, \sigma_{w_\omega}^2)$$

$$\frac{d\Theta_{V_w}}{dt} = -\frac{\Theta_{V_w}}{\tau_{V_w}} + w_{V_w} \qquad\qquad w_{V_w} \in N(0, \sigma_{w_{V_w}}^2)$$

$$\frac{d\Theta_{r_V}}{dt} = -\frac{\Theta_{r_w}}{\tau_\omega} + w_{r_w} \qquad\qquad w_{r_V} \in N(0, \sigma_{w_{r_w}}^2)$$

$$\frac{d}{dt}\begin{pmatrix} F_{a1_x} \\ F_{a2_x} \\ F_{a3_x} \end{pmatrix} = \begin{pmatrix} 0 & \gamma_{1,1} & 0 \\ 0 & 0 & \gamma_{2,1} \\ 0 & 0 & 0 \end{pmatrix}\begin{pmatrix} F_{a1_x} \\ F_{a2_x} \\ F_{a3_x} \end{pmatrix} + \begin{pmatrix} \xi_{1,1} \\ \xi_{2,1} \\ \xi_{3,1} \end{pmatrix} \qquad \xi_{1,1}, \xi_{2,1}, \xi_{3,1} \in N(0, \sigma_{\xi_{F_a}}^2)$$

$$\frac{d}{dt}\begin{pmatrix} F_{a1_y} \\ F_{a2_y} \\ F_{a3_y} \end{pmatrix} = \begin{pmatrix} 0 & \gamma_{1,2} & 0 \\ 0 & 0 & \gamma_{2,2} \\ 0 & 0 & 0 \end{pmatrix}\begin{pmatrix} F_{a1_y} \\ F_{a2_y} \\ F_{a3_y} \end{pmatrix} + \begin{pmatrix} \xi_{1,2} \\ \xi_{2,2} \\ \xi_{3,2} \end{pmatrix} \qquad \xi_{1,2}, \xi_{2,2}, \xi_{3,2} \in N(0, \sigma_{\xi_{F_a}}^2)$$

$$\frac{d}{dt}\begin{pmatrix} F_{a1_z} \\ F_{a2_z} \\ F_{a3_z} \end{pmatrix} = \begin{pmatrix} 0 & \gamma_{1,3} & 0 \\ 0 & 0 & \gamma_{2,2} \\ 0 & 0 & 0 \end{pmatrix}\begin{pmatrix} F_{a1_z} \\ F_{a2_z} \\ F_{a3_z} \end{pmatrix} + \begin{pmatrix} \xi_{1,3} \\ \xi_{2,3} \\ \xi_{3,3} \end{pmatrix} \qquad \xi_{1,3}, \xi_{2,3}, \xi_{3,3} \in N(0, \sigma_{\xi_{F_a}}^2)$$

$$\frac{d}{dt}\begin{pmatrix} M_{a1_x} \\ M_{a2_x} \\ M_{a3_x} \end{pmatrix} = \begin{pmatrix} 0 & \gamma_{1,4} & 0 \\ 0 & 0 & \gamma_{2,4} \\ 0 & 0 & 0 \end{pmatrix}\begin{pmatrix} M_{a1_x} \\ M_{a2_x} \\ M_{a3_x} \end{pmatrix} + \begin{pmatrix} \xi_{1,4} \\ \xi_{2,4} \\ \xi_{3,4} \end{pmatrix} \qquad \xi_{1,4}, \xi_{2,4}, \xi_{3,4} \in N(0, \sigma_{\xi_{M_a}}^2)$$

$$\frac{d}{dt}\begin{pmatrix} M_{a1_y} \\ M_{a2_y} \\ M_{a3_y} \end{pmatrix} = \begin{pmatrix} 0 & \gamma_{1,5} & 0 \\ 0 & 0 & \gamma_{2,5} \\ 0 & 0 & 0 \end{pmatrix}\begin{pmatrix} M_{a1_y} \\ M_{a2_y} \\ M_{a3_y} \end{pmatrix} + \begin{pmatrix} \xi_{1,5} \\ \xi_{2,5} \\ \xi_{3,5} \end{pmatrix} \qquad \xi_{1,5}, \xi_{2,5}, \xi_{3,5} \in N(0, \sigma_{\xi_{M_a}}^2)$$

$$\frac{d}{dt}\begin{pmatrix} M_{a1_z} \\ M_{a2_z} \\ M_{a3_z} \end{pmatrix} = \begin{pmatrix} 0 & \gamma_{1,6} & 0 \\ 0 & 0 & \gamma_{2,6} \\ 0 & 0 & 0 \end{pmatrix}\begin{pmatrix} M_{a1_z} \\ M_{a2_z} \\ M_{a3_z} \end{pmatrix} + \begin{pmatrix} \xi_{1,6} \\ \xi_{2,6} \\ \xi_{3,6} \end{pmatrix} \qquad \xi_{1,6}, \xi_{2,6}, \xi_{3,6} \in N(0, \sigma_{\xi_{M_a}}^2)$$

$$\frac{d}{dt}\begin{pmatrix} T_{A_1^+} \\ T_{A_2^+} \\ T_{A_3^+} \end{pmatrix} = \begin{pmatrix} 0 & \gamma_{1,7} & 0 \\ 0 & 0 & \gamma_{2,7} \\ 0 & 0 & 0 \end{pmatrix}\begin{pmatrix} T_{A_1^+} \\ T_{A_2^+} \\ T_{A_3^+} \end{pmatrix} + \begin{pmatrix} \xi_{1,7} \\ \xi_{2,7} \\ \xi_{3,7} \end{pmatrix} \qquad \xi_{1,7}, \xi_{2,7}, \xi_{3,7} \in N(0, \sigma_{\xi_T}^2)$$

$$\frac{d}{dt}\begin{pmatrix} T_{A_1^-} \\ T_{A_2^-} \\ T_{A_3^-} \end{pmatrix} = \begin{pmatrix} 0 & \gamma_{1,8} & 0 \\ 0 & 0 & \gamma_{2,8} \\ 0 & 0 & 0 \end{pmatrix}\begin{pmatrix} T_{A_1^-} \\ T_{A_2^-} \\ T_{A_3^-} \end{pmatrix} + \begin{pmatrix} \xi_{1,8} \\ \xi_{2,8} \\ \xi_{3,8} \end{pmatrix} \qquad \xi_{1,8}, \xi_{2,8}, \xi_{3,8} \in N(0, \sigma_{\xi_T}^2)$$

$$\frac{d}{dt}\begin{pmatrix} T_{B_1^+} \\ T_{B_2^+} \\ T_{B_3^+} \end{pmatrix} = \begin{pmatrix} 0 & \gamma_{1,9} & 0 \\ 0 & 0 & \gamma_{2,9} \\ 0 & 0 & 0 \end{pmatrix}\begin{pmatrix} T_{B_1^+} \\ T_{B_2^+} \\ T_{B_3^+} \end{pmatrix} + \begin{pmatrix} \xi_{1,9} \\ \xi_{2,9} \\ \xi_{3,9} \end{pmatrix} \qquad \xi_{1,9}, \xi_{2,9}, \xi_{3,9} \in N(0, \sigma_{\xi_T}^2)$$

$$\frac{d}{dt}\begin{pmatrix} T_{B_1^-} \\ T_{B_2^-} \\ T_{B_3^-} \end{pmatrix} = \begin{pmatrix} 0 & \gamma_{1,10} & 0 \\ 0 & 0 & \gamma_{2,10} \\ 0 & 0 & 0 \end{pmatrix}\begin{pmatrix} T_{B_1^-} \\ T_{B_2^-} \\ T_{B_3^-} \end{pmatrix} + \begin{pmatrix} \xi_{1,10} \\ \xi_{2,10} \\ \xi_{3,10} \end{pmatrix} \qquad \xi_{1,10}, \xi_{2,10}, \xi_{3,10} \in N(0, \sigma_{\xi_T}^2)$$

$$\frac{d}{dt}\begin{pmatrix} V_{w_1} \\ V_{w_2} \\ V_{w_3} \end{pmatrix} = \begin{pmatrix} 0 & \gamma_{1,11} & 0 \\ 0 & 0 & \gamma_{2,11} \\ 0 & 0 & 0 \end{pmatrix}\begin{pmatrix} V_{w_1} \\ V_{w_2} \\ V_{w_3} \end{pmatrix} + \begin{pmatrix} \xi_{1,11} \\ \xi_{2,11} \\ \xi_{3,11} \end{pmatrix} \qquad \xi_{1,11}, \xi_{2,11}, \xi_{3,11} \in N(0, \sigma^2_{\xi_{V_w}})$$

$$\frac{d}{dt}\begin{pmatrix} \psi_{w_1} \\ \psi_{w_2} \\ \psi_{w_3} \end{pmatrix} = \begin{pmatrix} 0 & \gamma_{1,12} & 0 \\ 0 & 0 & \gamma_{2,12} \\ 0 & 0 & 0 \end{pmatrix}\begin{pmatrix} \psi_{w_1} \\ \psi_{w_2} \\ \psi_{w_3} \end{pmatrix} + \begin{pmatrix} \xi_{1,12} \\ \xi_{2,12} \\ \xi_{3,12} \end{pmatrix} \qquad \xi_{1,12}, \xi_{2,12}, \xi_{3,12} \in N(0, \sigma^2_{\xi_{\psi_w}})$$

$$(A.15)$$

The 44×1 process noise vector w, and matrix $\bar{G}$ are,

$$w = \begin{bmatrix} w_f & w_\omega & w_{V_w} & w_{r_V} & \xi_{1,1} & \xi_{2,1} & \xi_{3,1} & \xi_{1,2} & \xi_{2,2} & \xi_{3,2} \dots \xi_{1,12} & \xi_{2,12} & \xi_{3,12} \end{bmatrix}^T \quad (A.16)$$

$$\bar{G} = \begin{bmatrix} \bar{0}_{18\times44} \\ \bar{I}_{44\times44} \end{bmatrix}_{62\times44} \qquad (A.17)$$

with $\bar{0}$ a matrix with zeros and $\bar{I}$ the identity matrix. Finally, the covariance matrix, $\bar{Q}$, is a 44×44 diagonal matrix with,

$$diag\left(\bar{Q}\right) = \Big[\sigma^2_{w_f} \; \sigma^2_{w_f} \; \sigma^2_{w_f} \; \sigma^2_{w_\omega} \; \sigma^2_{w_\omega} \; \sigma^2_{w_\omega} \; \sigma^2_{w_{V_w}} \; \sigma^2_{w_{r_w}}$$
$$\sigma^2_{\xi_{1,1}} \; \sigma^2_{\xi_{2,1}} \; \sigma^2_{xi_{3,1}} \dots \sigma^2_{\xi_{1,12}} \; \sigma^2_{\xi_{2,12}} \; \sigma^2_{\xi_{3,12}} \Big] \qquad (A.18)$$

A.2 Two lines RFD kites

The state vector of the EKF is,

$$\begin{aligned} x = \big[& r \; v \; \Upsilon \; \omega \; \Theta_B \; \Theta_{B_V} \; \Theta_f \; \Theta_\omega \; \Theta_{V_w} \; \Theta_{r_V} \\ & F_{a_1} \; M_{a_1} \; T_{A^+_1} \; T_{A^-_1} \; V_{w_1} \; \psi_{w_1} \\ & F_{a_2} \; M_{a_2} \; T_{A^+_2} \; T_{A^-_2} \; V_{w_2} \; \psi_{w_2} \\ & F_{a_3} \; M_{a_3} \; T_{A^+_3} \; T_{A^-_3} \; V_{w_3} \; \psi_{w_3} \big]^T \end{aligned} \qquad (A.19)$$

where x is a 56×1 column vector.

And the observation vector of the EKF is,

$$\tilde{y} = \begin{bmatrix} \tilde{B} & \tilde{v} & \tilde{r} & \tilde{f} & \tilde{\omega} & \tilde{v}_a & \tilde{\alpha} & \tilde{\beta} & \tilde{T}_{A^+} & \tilde{T}_{A^-} & \tilde{B}_V & \tilde{r}_V & \tilde{V}_w & \tilde{D} \end{bmatrix}^T \qquad (A.20)$$

where $\tilde{y}$ is a $26x1$ column vector

A.2.1 Observation Model

The explicit form of the observation model $\tilde{y} = h(x) + \eta$, can be written as

$$\tilde{B} = \bar{R}^T_{EK} B_0 + \Theta_B + \eta_B \qquad\qquad\qquad \eta_B \in N(0, \sigma^2_{\eta_B})$$

$$\tilde{v} = \bar{R}_{EK}v + \eta_v \qquad\qquad \eta_v \in N(0, \sigma_{\eta_v}^2)$$

$$\tilde{r} = r + \eta_r \qquad\qquad \eta_r \in N(0, \sigma_{\eta_r}^2)$$

$$\tilde{f} = \frac{1}{m_k}\left[F_{a1} + \sum_{i=\pm}(T_{A^i} + T_{B^i})\right] + \Theta_f + \eta_f \qquad\qquad \eta_f \in N(0, \sigma_{\eta_f}^2)$$

$$\tilde{\omega} = \omega + \Theta_\omega + \eta_\omega \qquad\qquad \eta_\omega \in N(0, \sigma_{\eta_\omega}^2)$$

$$\tilde{v}_a =\mid v_a \mid + \eta_{v_a} \qquad\qquad \eta_{v_a} \in N(0, \sigma_{\eta_{v_a}}^2)$$

$$\tilde{\alpha} = \arctan\left(\frac{w_a}{u_a}\right) + \eta_\alpha \qquad\qquad \eta_\alpha \in N(0, \sigma_{\eta_\alpha}^2)$$

$$\tilde{\beta} = \arcsin\left(\frac{v_a}{\mid v_a \mid}\right) + \eta_\beta \qquad\qquad \eta_\beta \in N(0, \sigma_{\eta_\beta}^2)$$

$$\tilde{T}_{A^+} = T_{A_1^+} + \eta_{T_{A^+}} \qquad\qquad \eta_{T_{A^+}} \in N(0, \sigma_{\eta_T}^2)$$

$$\tilde{T}_{A^-} = T_{A_1^-} + \eta_{T_{A^-}} \qquad\qquad \eta_{T_{A^-}} \in N(0, \sigma_{\eta_T}^2)$$

$$\tilde{B}_V = \bar{R}_{EV}^T B_0 + \Theta_{BV} + \eta_{BV} \qquad\qquad \eta_{BV} \in N(0, \sigma_{\eta_{BV}}^2)$$

$$\tilde{r}_V = \gamma_{\psi_{w_1}}\psi_{w_2} + \Theta_{rV} + \eta_{rV} \qquad\qquad \eta_{rV} \in N(0, \sigma_{\eta_{rV}}^2$$

$$\tilde{V}_w = V_{w_1} + \Theta_{V_w} + \eta_{V_w} \qquad\qquad \eta_{V_w} \in N(0, \sigma_{\eta_{V_w}}^2)$$

$$\tilde{D} =\mid r \mid + \eta_D \qquad\qquad \eta_D \in N(0, \sigma_{\eta_D}^2)$$

$$\text{(A.21)}$$

Then, η, is a 26×1 column vector containing the measurements observation noises,

$$\eta = \begin{bmatrix} \eta_B & \eta_r & \eta_v & \eta_f & \eta_\omega & \eta_a & \eta_\alpha & \eta_\beta & \eta_{T_{A^+}} & \eta_{T_{A^-}} \\ \eta_{BV} & \eta_{rV} & \eta_{V_w} & \eta_D \end{bmatrix}^T \qquad\qquad \text{(A.22)}$$

and the covariance matrix, $\bar{R}$, is a 26×26 diagonal matrix with,

$$diag(\bar{R}) = \left[\sigma_{\eta_B}^2 \ \ \sigma_{\eta_B}^2 \ \ \sigma_{\eta_B}^2 \ \ \sigma_{\eta_r}^2 \ \ \sigma_{\eta_r}^2 \ \ \sigma_{\eta_r}^2 \ \ \sigma_{\eta_v}^2 \ \ \sigma_{\eta_v}^2 \ \ \sigma_{\eta_v}^2 \ \ \sigma_{\eta_f}^2 \ \ \sigma_{\eta_f}^2 \ \ \sigma_{\eta_f}^2 \ \ \sigma_{\eta_\omega}^2 \ \ \sigma_{\eta_\omega}^2 \right.$$
$$\left. \sigma_{\eta_\omega}^2 \ \ \sigma_{\eta_{v_a}}^2 \ \ \sigma_{\eta_\alpha}^2 \ \ \sigma_{\eta_\beta}^2 \ \ \sigma_{\eta_T}^2 \ \ \sigma_{\eta_T}^2 \ \ \sigma_{\eta_{BV}}^2 \ \ \sigma_{\eta_{BV}}^2 \ \ \sigma_{\eta_{BV}}^2 \ \ \sigma_{\eta_{rV}}^2 \ \ \sigma_{\eta_{V_w}}^2 \ \ \sigma_{\eta_D}^2 \right] \ \ \text{(A.23)}$$

A.2.2 Process model

The explicit form of the process model, $dx(t)/dt = f_{\text{proc}}[x(t)] + \bar{G}w(t)$, can be written as,

$$\frac{dr}{dt} = \bar{R}_{EK}v$$

$$\frac{d\boldsymbol{v}}{dt} = \begin{pmatrix} f_x \\ f_y \\ f_z \end{pmatrix} + \bar{\boldsymbol{R}}_{EK}^T \begin{pmatrix} 0 \\ 0 \\ g \end{pmatrix} + \begin{pmatrix} rv - qw \\ pw - ru \\ qu - pv \end{pmatrix}$$

$$\frac{d\boldsymbol{\Upsilon}}{dt} = \begin{bmatrix} p + (q \sin \phi + r \cos \phi) \tan \theta \\ q \cos \phi - r \sin \phi \\ (q \sin \phi + r \cos \phi) \sec \theta \end{bmatrix}$$

$$\frac{d\boldsymbol{\omega}}{dt} = \bar{\boldsymbol{I}}_{O_K}^{-1} \begin{bmatrix} M_x - I_{xz}qp + rq \left(I_y - I_z\right) \\ M_y + I_{xz} \left(p^2 - r^2\right) + pr \left(I_z - I_x\right) \\ M_z + I_{xz}qr + pq \left(I_x - I_y\right) \end{bmatrix}$$

$$\frac{d\boldsymbol{\Theta}_B}{dt} = 0$$

$$\frac{d\boldsymbol{\Theta}_{Bv}}{dt} = 0$$

$$\frac{d\boldsymbol{\Theta}_f}{dt} = -\frac{\boldsymbol{\Theta}_f}{\tau_a} + \boldsymbol{w}_f \qquad\qquad \boldsymbol{w}_f \in N(0, \sigma_{w_f}^2)$$

$$\frac{d\boldsymbol{\Theta}_\omega}{dt} = -\frac{\boldsymbol{\Theta}_\omega}{\tau_\omega} + \boldsymbol{w}_\omega \qquad\qquad \boldsymbol{w}_\omega \in N(0, \sigma_{w_\omega}^2)$$

$$\frac{d\boldsymbol{\Theta}_{V_w}}{dt} = -\frac{\boldsymbol{\Theta}_{V_w}}{\tau_{V_w}} + w_{V_w} \qquad\qquad w_{V_w} \in N(0, \sigma_{w_{V_w}}^2)$$

$$\frac{d\boldsymbol{\Theta}_{r_V}}{dt} = -\frac{\boldsymbol{\Theta}_{r_w}}{\tau_\omega} + w_{r_w} \qquad\qquad w_{r_V} \in N(0, \sigma_{w_{r_w}}^2)$$

$$\frac{d}{dt} \begin{pmatrix} F_{a1_x} \\ F_{a2_x} \\ F_{a3_x} \end{pmatrix} = \begin{pmatrix} 0 & \gamma_{1,1} & 0 \\ 0 & 0 & \gamma_{2,1} \\ 0 & 0 & 0 \end{pmatrix} \begin{pmatrix} F_{a1_x} \\ F_{a2_x} \\ F_{a3_x} \end{pmatrix} + \begin{pmatrix} \xi_{1,1} \\ \xi_{2,1} \\ \xi_{3,1} \end{pmatrix} \qquad \xi_{1,1}, \xi_{2,1}, \xi_{3,1} \in N(0, \sigma_{\xi_{F_a}}^2)$$

$$\frac{d}{dt} \begin{pmatrix} F_{a1_y} \\ F_{a2_y} \\ F_{a3_y} \end{pmatrix} = \begin{pmatrix} 0 & \gamma_{1,2} & 0 \\ 0 & 0 & \gamma_{2,2} \\ 0 & 0 & 0 \end{pmatrix} \begin{pmatrix} F_{a1_y} \\ F_{a2_y} \\ F_{a3_y} \end{pmatrix} + \begin{pmatrix} \xi_{1,2} \\ \xi_{2,2} \\ \xi_{3,2} \end{pmatrix} \qquad \xi_{1,2}, \xi_{2,2}, \xi_{3,2} \in N(0, \sigma_{\xi_{F_a}}^2)$$

$$\frac{d}{dt} \begin{pmatrix} F_{a1_z} \\ F_{a2_z} \\ F_{a3_z} \end{pmatrix} = \begin{pmatrix} 0 & \gamma_{1,3} & 0 \\ 0 & 0 & \gamma_{2,2} \\ 0 & 0 & 0 \end{pmatrix} \begin{pmatrix} F_{a1_z} \\ F_{a2_z} \\ F_{a3_z} \end{pmatrix} + \begin{pmatrix} \xi_{1,3} \\ \xi_{2,3} \\ \xi_{3,3} \end{pmatrix} \qquad \xi_{1,3}, \xi_{2,3}, \xi_{3,3} \in N(0, \sigma_{\xi_{F_a}}^2)$$

$$\frac{d}{dt} \begin{pmatrix} M_{a1_x} \\ M_{a2_x} \\ M_{a3_x} \end{pmatrix} = \begin{pmatrix} 0 & \gamma_{1,4} & 0 \\ 0 & 0 & \gamma_{2,4} \\ 0 & 0 & 0 \end{pmatrix} \begin{pmatrix} M_{a1_x} \\ M_{a2_x} \\ M_{a3_x} \end{pmatrix} + \begin{pmatrix} \xi_{1,4} \\ \xi_{2,4} \\ \xi_{3,4} \end{pmatrix} \qquad \xi_{1,4}, \xi_{2,4}, \xi_{3,4} \in N(0, \sigma_{\xi_{M_a}}^2)$$

$$\frac{d}{dt} \begin{pmatrix} M_{a1_y} \\ M_{a2_y} \\ M_{a3_y} \end{pmatrix} = \begin{pmatrix} 0 & \gamma_{1,5} & 0 \\ 0 & 0 & \gamma_{2,5} \\ 0 & 0 & 0 \end{pmatrix} \begin{pmatrix} M_{a1_y} \\ M_{a2_y} \\ M_{a3_y} \end{pmatrix} + \begin{pmatrix} \xi_{1,5} \\ \xi_{2,5} \\ \xi_{3,5} \end{pmatrix} \qquad \xi_{1,5}, \xi_{2,5}, \xi_{3,5} \in N(0, \sigma_{\xi_{M_a}}^2)$$

$$\frac{d}{dt} \begin{pmatrix} M_{a1_z} \\ M_{a2_z} \\ M_{a3_z} \end{pmatrix} = \begin{pmatrix} 0 & \gamma_{1,6} & 0 \\ 0 & 0 & \gamma_{2,6} \\ 0 & 0 & 0 \end{pmatrix} \begin{pmatrix} M_{a1_z} \\ M_{a2_z} \\ M_{a3_z} \end{pmatrix} + \begin{pmatrix} \xi_{1,6} \\ \xi_{2,6} \\ \xi_{3,6} \end{pmatrix} \qquad \xi_{1,6}, \xi_{2,6}, \xi_{3,6} \in N(0, \sigma_{\xi_{M_a}}^2)$$

$$\frac{d}{dt}\begin{pmatrix} T_{A_1^+} \\ T_{A_2^+} \\ T_{A_3^+} \end{pmatrix} = \begin{pmatrix} 0 & \gamma_{1,7} & 0 \\ 0 & 0 & \gamma_{2,7} \\ 0 & 0 & 0 \end{pmatrix}\begin{pmatrix} T_{A_1^+} \\ T_{A_2^+} \\ T_{A_3^+} \end{pmatrix} + \begin{pmatrix} \xi_{1,7} \\ \xi_{2,7} \\ \xi_{3,7} \end{pmatrix} \qquad \xi_{1,7}, \xi_{2,7}, \xi_{3,7} \in N(0, \sigma_{\xi_T}^2)$$

$$\frac{d}{dt}\begin{pmatrix} T_{A_1^-} \\ T_{A_2^-} \\ T_{A_3^-} \end{pmatrix} = \begin{pmatrix} 0 & \gamma_{1,8} & 0 \\ 0 & 0 & \gamma_{2,8} \\ 0 & 0 & 0 \end{pmatrix}\begin{pmatrix} T_{A_1^-} \\ T_{A_2^-} \\ T_{A_3^-} \end{pmatrix} + \begin{pmatrix} \xi_{1,8} \\ \xi_{2,8} \\ \xi_{3,8} \end{pmatrix} \qquad \xi_{1,8}, \xi_{2,8}, \xi_{3,8} \in N(0, \sigma_{\xi_T}^2)$$

$$\frac{d}{dt}\begin{pmatrix} V_{w_1} \\ V_{w_2} \\ V_{w_3} \end{pmatrix} = \begin{pmatrix} 0 & \gamma_{1,11} & 0 \\ 0 & 0 & \gamma_{2,11} \\ 0 & 0 & 0 \end{pmatrix}\begin{pmatrix} V_{w_1} \\ V_{w_2} \\ V_{w_3} \end{pmatrix} + \begin{pmatrix} \xi_{1,11} \\ \xi_{2,11} \\ \xi_{3,11} \end{pmatrix} \qquad \xi_{1,11}, \xi_{2,11}, \xi_{3,11} \in N(0, \sigma_{\xi_{V_w}}^2)$$

$$\frac{d}{dt}\begin{pmatrix} \psi_{w_1} \\ \psi_{w_2} \\ \psi_{w_3} \end{pmatrix} = \begin{pmatrix} 0 & \gamma_{1,12} & 0 \\ 0 & 0 & \gamma_{2,12} \\ 0 & 0 & 0 \end{pmatrix}\begin{pmatrix} \psi_{w_1} \\ \psi_{w_2} \\ \psi_{w_3} \end{pmatrix} + \begin{pmatrix} \xi_{1,12} \\ \xi_{2,12} \\ \xi_{3,12} \end{pmatrix} \qquad \xi_{1,12}, \xi_{2,12}, \xi_{3,12} \in N(0, \sigma_{\xi_{\psi_w}}^2)$$

$$(A.24)$$

The 38×1 process noise vector $\boldsymbol{w}$, and matrix $\bar{\boldsymbol{G}}$ are,

$$\boldsymbol{w} = \begin{bmatrix} \boldsymbol{w}_f & \boldsymbol{w}_\omega & w_{V_w} & w_{r_V} & \xi_{1,1} & \xi_{2,1} & \xi_{3,1} & \xi_{1,2} & \xi_{2,2} & \xi_{3,2} \dots \xi_{1,12} & \xi_{2,12} & \xi_{3,12} \end{bmatrix}^T \quad (A.25)$$

$$\bar{\boldsymbol{G}} = \begin{bmatrix} \bar{\boldsymbol{0}}_{18 \times 38} \\ \bar{\boldsymbol{I}}_{38 \times 38} \end{bmatrix}_{56 \times 38} \quad (A.26)$$

with $\bar{\boldsymbol{0}}$ a matrix with zeros and $\bar{\boldsymbol{I}}$ the identity matrix. Finally, the covariance matrix, $\bar{\boldsymbol{Q}}$, is a 38×38 diagonal matrix with,

$$diag\left(\bar{\boldsymbol{Q}}\right) = \begin{bmatrix} \sigma_{w_f}^2 & \sigma_{w_f}^2 & \sigma_{w_f}^2 & \sigma_{w_\omega}^2 & \sigma_{w_\omega}^2 & \sigma_{w_\omega}^2 & \sigma_{w_{V_w}}^2 & \sigma_{w_{r_w}}^2 \\ \sigma_{\xi_{1,1}}^2 & \sigma_{\xi_{2,1}}^2 & \sigma_{xi_{3,1}}^2 \dots \sigma_{\xi_{1,12}}^2 & \sigma_{\xi_{2,12}}^2 & \sigma_{\xi_{3,12}}^2 \end{bmatrix} \quad (A.27)$$

A.3 EKF parameters

Table A.1 shows the parameters used for the process and observation models of the EKF.

LEI Kite				RFD Kite			
Symbol	Value	Symbol	Value	Symbol	Value	Symbol	Value
$\gamma_{1,1...6}$	0.1	$\gamma_{2,1...6}$	0.1	$\gamma_{1,1...6}$	0.1	$\gamma_{2,1...6}$	0.1
$\gamma_{1,7...10}$	1	$\gamma_{2,7...10}$	1	$\gamma_{1...8}$	1	$\gamma_{2...8}$	1
$\gamma_{1,11}$	0.1	$\gamma_{2,11}$	0.1	$\gamma_{1,11}$	0.1	$\gamma_{2,11}$	0.1
$\gamma_{1,12}$	$10\pi/180$	$\gamma_{2,12}$	$10\pi/180$	$\gamma_{1,12}$	$10\pi/180$	$\gamma_{2,12}$	$10\pi/180$
τ_a	100 s	τ_ω	100 s	τ_a	100 s	τ_ω	100 s
τ_{V_w}	100 s			τ_{V_w}	100 s		
σ_{w_f}	0.2 m/s^2	σ_{w_ω}	$0.5\pi/180$ rad/s	σ_{w_f}	0.05 m/s^2	σ_{w_ω}	$0.1\pi/180$ rad/s
$\sigma_{w_{V_w}}$	0.002 m/s	$\sigma_{w_{r_V}}$	$0.5\pi/180$ rad/s	$\sigma_{w_{V_w}}$	0.001 m/s	$\sigma_{w_{r_V}}$	$0.1\pi/180$ rad/s
$\sigma_{\xi_{F_a}}$	17.0 N	$\sigma_{\xi_{M_a}}$	15.0 Nm	$\sigma_{\xi_{F_a}}$	10.0 N	$\sigma_{\xi_{M_a}}$	15.0 Nm
σ_{ξ_T}	3.0 N	$\sigma_{\xi_{V_w}}$	0.005 m/s	σ_{ξ_T}	5.0 N	$\sigma_{\xi_{V_w}}$	0.02 m/s
$\sigma_{\xi_{\psi_w}}$	$0.8\pi/180$ rad			$\sigma_{\xi_{\psi_w}}$	$0.1\pi/180$ rad		
σ_{η_B}	0.1 G	σ_{η_r}	2.0 m	σ_{η_B}	0.2 G	σ_{η_r}	5.0 m
σ_{η_v}	0.5 m/s	σ_{η_f}	0.2 m/s^2	σ_{η_v}	2.0 m/s	σ_{η_f}	4.0 m/s^2
σ_{η_ω}	$4.4\pi/180$ rad/s	$\sigma_{\eta_{va}}$	0.5 m/s	σ_{η_ω}	$8.0\pi/180$ rad/s	$\sigma_{\eta_{va}}$	1.0 m/s
σ_{η_α}	$0.5\pi/180$ rad	σ_{η_β}	$0.5\pi/180$ rad	σ_{η_α}	$0.5\pi/180$ rad	σ_{η_β}	$0.5\pi/180$ rad
σ_{η_T}	10.0 N	$\sigma_{\eta_{B_w}}$	0.01 G	σ_{η_T}	10.0 N	$\sigma_{\eta_{B_w}}$	0.02 G
$\sigma_{\eta_{r_w}}$	$8.0\pi/180$ rad/s	$\sigma_{\eta_{V_w}}$	0.5 m/s	$\sigma_{\eta_{r_w}}$	$4.0\pi/180$ rad/s	$\sigma_{\eta_{V_w}}$	0.5 m/s
σ_{η_D}	0.001 m	$\sigma_{\eta_{P_{ik}}}$	0.4	σ_{η_D}	0.01 m		

TABLE A.1: Parameters of the FPR algorithm

B PRE-FLIGHT CALIBRATIONS

In this appendix, a description of the pre-flight calibration procedures carried out to remove the in-run constant errors of the sensors used in experimental setup is presented. After pre-flight calibrations were carried out, the errors of the recorded measurements are assumed to be described by the error models defined in Chapter. 4.

B.0.1 Inertial sensors

A post calibration error model was proposed:

$$\tilde{y} = (1 + k)y + b(t) \tag{B.1}$$

where $\tilde{y}$ is the sensor representation of y, k is a scale factor error and b is a time varying Bias.

For low cost, micro-electro-mechanical-system (MEMS) sensors, in-run stochastic variations of k were neglected against variations of b, thus considered constant and calculated during the pre-flight calibration phase. Bias error was modeled as $b(t) = b_0 + b_R(t)$ where b_0 is usually referred as a *turn-on to turn-on bias* and also considered an in-run constant calculated during the pre-flight calibrations phase.

To calculate both in-run constants (k, b_0), averaged measurements of the inertial magnitudes are obtained while the sensor is positioned stationary at different orientations with respect to the S_E reference frame, i.e. with each of its unit vectors $[\boldsymbol{x}_k, \boldsymbol{y}_k, \boldsymbol{z}_k]$ along the $\boldsymbol{z}_E$ downward direction. For each axis, the averaged measured specific force is calibrated with the expected gravitational acceleration (S_E is taken as an inertial reference frame), while the averaged measured angular rate is calibrated to be negligible for low-cost IMUs (for higher grade IMUs, self-aligning procedures may apply [51, 106]). The described procedure was automatically performed by Px4™ software during the sensors configuration phase, and the recorded specific force and angular velocity are considered to be free of in-run constant errors.

B.0.2 GPS

GPS sensor does not require of any manual calibration procedure. The sensor is initialized when the PixHawk™ hardware is powered up, and a valid GPS fix is visually indicated by a blinking green light. When a valid fix is obtained, the trigger signal is commanded and the flight can be started (Chapter. 3.5).

B.0.3 Magnetometer

Earth magnetic field measurements projected in both, kite (S_K) and wind-station (S_V) body axes, are affected by Earth magnetic field local perturbations and magnetometer sensors error. For the on-board the kite magnetometer, pre-flight calibration was performed by Px4™ software during the sensors configuration phase. For the wind-station magnetometer, additionally, a calibration was carried out in the field for each flight campaign to remove *hard-iron* perturbations induced by the steel bearing of the wind station, and the local conditions of the test area. *Soft-iron* perturbations were not calibrated but monitored to be neligibele.

Calibration was performed, as described in [38], by rotating the wind station platform multiple turns along its z_V axis. The measured Earth magnetic field, projected in the x_V and y_V body axes ($\tilde{B}_V$), is represented in Fig. B.1 for the RFD kite flight-
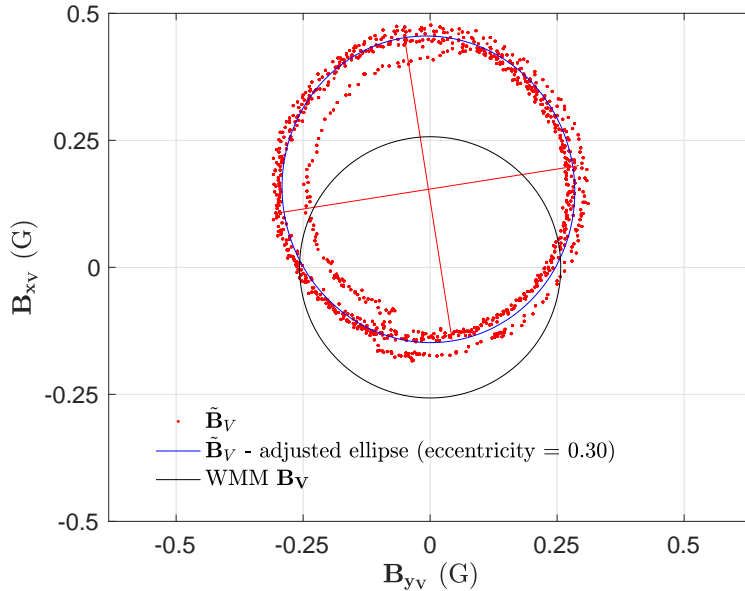
FIGURE B.1: Measured and modeled Earth magnetic field vector projected in the S_V reference frame.

campaign. In this figure, the projection of the Earth magnetic field vector, as modeled by the World Magnetic Model (WMM) (B_o)[95], is also represented for the given flight date and location. This results in a circumference of radius equal to the modulus of the local tangent plane projection of B_0 (0.2571G) and center in the origin of the reference frame (O_V). The S_V measurements of the Earth magnetic field vector have been adjusted to an ellipse of eccentricity equal to 0.3. The center of this ellipse is shifted from the origin by 0.153G and −0.003G along the x_V and y_V axes. The eccentricity of the ellipse denotes *soft-iron* perturbations which depend on the heading of the wind vane, while the shifted center of the ellipse denotes *hard-iron* perturbations which are

constant in the S_V body axes. A representation of the calibrated measurements is shown in Fig. B.2. In this figure, the measurements have been adjusted to a circumference as
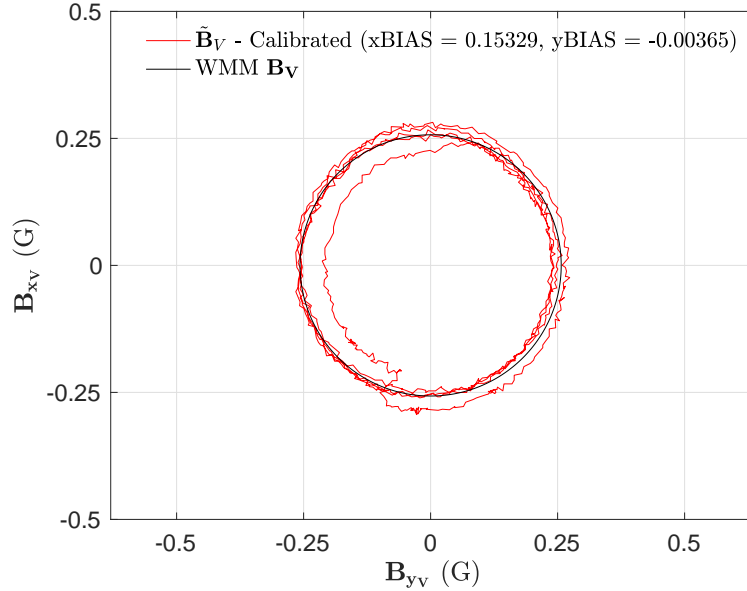

FIGURE B.2: Calibrated and modeled Earth magnetic field vector projected in the S_V reference frame.

soft-iron perturbations have been neglected due to the low eccentricity of the ellipse, constant in-run BIAS have been removed and a scale factor of 0.87 has been applied.

B.0.4 Air-data sensors

The low-cost static and dynamic pressure sensors of the PixHawk™ hardware are calibrated during the Px4™ sensors configuration phase. However, during this calibration, only a constant BIAS of the dynamic pressure sensor can be identified. This is achieved measuring the sensor output while the pitot tube is isolated from the wind (zero aerodynamic speed). The scale-factors of these sensors are preconfigured in the Px4™ software. A full calibration of the air-data sensors should include i) a leaking test of the pneumatic lines and ii) static and dynamic pressure sensors calibration along the whole flying envelope. This is achieved by providing simultaneously calibrated static and dynamic pressures to the pneumatic pitot lines using specialized equipment (e.g. D.Marchiori RVSM Air Data Test Sets [26]).

The high-cost Aeroprobe™ air-data computer and multi-hole pitot tube were factory calibrated. Pitot probes with serials 1190552-1 and 1190552- 2 were used, and specific calibration files for each probe were provided by Aeroprobe on 8/15/2019 and Mach = 0.03.

B.0.5 Load-cells

Each load-cell was individually calibrated together with its whole, analog-to-digital, acquisition chain. This was achieved by loading each load-cell with calibrated weights, while the output analog signal was acquired on the same channel of the National Instruments analog-to-digital converter used during the flight. A linear correlation between the load and the output voltage was assumed, and the scale factor k, and constant BIAS b, were identified. The selected TS-AMP load cells (Chapter. 3.4.2) are self-amplified with regulated input voltage, therefore, compensation for fluctuations on the load-cell input voltage was not required.

Figure. B.3 shows output voltages of the 10 kg TS-AMP load-cell inserted in the right control-line, when loaded with 0, 2, 4, 6, 8 and 10 kg. The measured tension in the tether ($\tilde{T}$), can be then calculated as a function of the measured voltage (V_{cell}) as

$$\tilde{T} = kV_{cell} + b \tag{B.2}$$

where $k = 12.58$ and $b = -2.28$ for the selected load-cell.
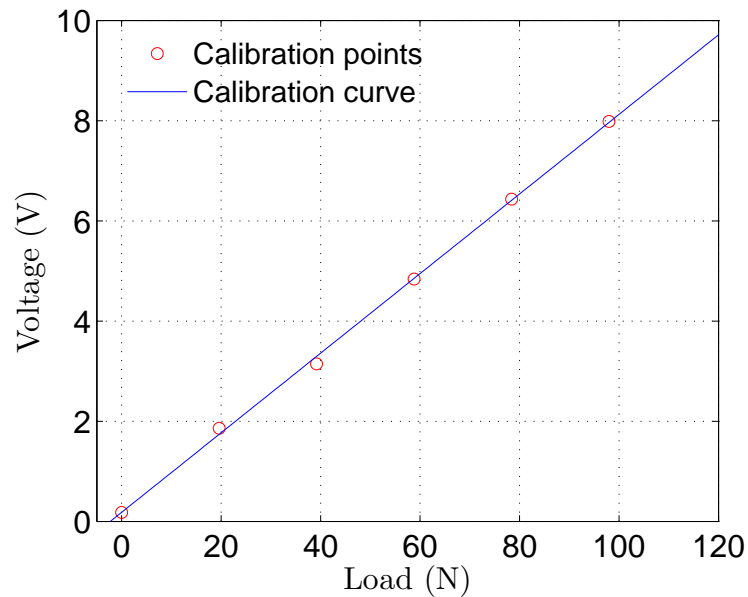

FIGURE B.3: Right control-line, 10Kg TS-AMP load cell calibration.

Bibliography

[1] Aeroprobe. *Aeroprobe micro air data computers*. URL: http://www.aeroprobe.com/micro-air-data-computer-models/.

[2] Swiss Air-Data. *Swiss Air-Data smart miniature vane*. URL: https://www.swiss-airdata.com/products/smv1.

[3] *Airborne Wind Energy Europe*. URL: http://www.airbornewindeurope.org.

[4] J. Alonso-Pardo and G. Sánchez-Arriaga. "Kite Model with Bridle Control for Wind-Power Generation". In: *Journal of Aircraft* 52.3 (2015), pp. 917–923. ISSN: 0021-8669. DOI: 10.2514/1.C033283. URL: http://dx.doi.org/10.2514/1.C033283.

[5] *Altaeros Clean Energy website*. URL: http://www.altaeros.com/energy.html.

[6] *AmpixPower*. URL: https://www.ampyxpower.com/.

[7] Cristina L. Archer and Ken Caldeira. "Global Assessment of High-Altitude Wind Power". In: *Energies* 2.2 (2009), pp. 307–319. ISSN: 1996-1073. DOI: 10.3390/en20200307. URL: http://www.mdpi.com/1996-1073/2/2/307.

[8] J. H. Baayen and W. J. Ockels. "Tracking control with adaption of kites". In: *IET Control Theory Applications* 6.2 (2012), pp. 182–191. ISSN: 1751-8644. DOI: 10.1049/iet-cta.2011.0037.

[9] R. E. BACH and R. C. WINGROVE. "Applications of state estimation in aircraft flight-data analysis". In: *Journal of Aircraft* 22.7 (1985), pp. 547–554. DOI: 10.2514/3.45164. URL: https://doi.org/10.2514/3.45164.

[10] R Borobia, G Sanchez-Arriaga, A Serino, and R Schmehl. "Flight-Path Reconstruction and Flight Test of Four-Line Power Kites". In: *Journal of Guidance, Control, and Dynamics* 41.12 (2018), pp. 2604–2614. DOI: 10.2514/1.G003581.

[11] R. Borobia-Moreno, I. Castro, A. Pastor, H. Endo, C. Cobos, R. Cavallaro, and G. Sánchez-Arriaga. "Activities and Roadmap on Airborne Wind Energy Systems at UC3M." In: *Journal of Japan Wind Energy Society* 44.134 (Aug. 2020).

[12] R. Borobia-Moreno, D. Ramiro-Rebollo, G. Sánchez-Arriaga, and R. Schmehl. "Flight Testing, Aerodynamic Parameter Identification and Dynamic Simulation of Rigid and Flexible Kites Applied to Airborne Wind Energy Systems". In: *Airborne Wind Energy Conference 2019: (AWEC 2019)*. 2019, p. 133. DOI: https://doi.org/10.4233/uuid:57fd203c-e069-11e9-9fcb-441ea15f7c9c.

[13] R. Borobia-Moreno, D. Ramiro-Rebollo, R. Schmehl, and G. Sánchez-Arriaga. "Identification of kite aerodynamic characteristics using the estimation before modeling technique". In: *Wind Energy* (2021). DOI: https://doi.org/10.1002/we.2591.

[14] R. Borobia-Moreno, G. Sánchez-Arriaga, and R. Schmehl. "Application of the Estimation-Before-Modeling Method to the Aerodynamic Characterization of Power Kites". In: *Airborne Wind Energy Conference 2017: (AWEC 2017)*. 2017, p. 26. DOI: http://doi.org/10.4233/uuid:4c361ef1-d2d2-4d14-9868-16541f60edc7.

[15] R. Borobia-Moreno, A. Serino, H. Endo, and G. Sánchez-Arriaga. *Flight Testing Setup for the Aerodynamic Characterization of Power Kites Applied to Airborne Wind Energy Generation*. World Wind Energy Conference, WWEC2017. Poster Contribution. 2017.

[16] J. Breukels. *An Engineering Methodology for Kite Design*. BOXPress, 2010. ISBN: 9789088912306. URL: https://books.google.es/books?id=-s4tmwEACAAJ.

[17] M. Canale, L. Fagiano, and M. Milanese. "Power Kites for Wind Energy Generation [Applications of Control]". In: *IEEE Control Systems Magazine* 27.6 (2007), pp. 25–38. ISSN: 1066-033X. DOI: 10.1109/MCS.2007.909465.

[18] United Nations Climate Change. *What is the Kyoto Protocol?* URL: https://unfccc.int/process-and-meetings/the-kyoto-protocol/what-is-the-kyoto-protocol.

[19] Antonello Cherubini, Andrea Papini, Rocco Vertechy, and Marco Fontana. "Airborne Wind Energy Systems: A review of the technologies". In: *Renewable and Sustainable Energy Reviews* 51.Supplement C (2015), pp. 1461 –1476. ISSN: 1364-0321. DOI: https://doi.org/10.1016/j.rser.2015.07.053. URL: http://www.sciencedirect.com/science/article/pii/S1364032115007005.

[20] Douglas Aircraft Company., R. D. Finck, and D. E. Hoak. *USAF stability and control datcom*. Springfield, Va.: National Technical Information Service, 1975, p. 9 v. URL: //catalog.hathitrust.org/Record/003147675.

[21] D Costa. "Experimental Investigation of Aerodynamic and Structural Properties of a Kite". MA thesis. ETH Zurich, 2001.

[22] Global Wind Energy Council. *Global Wind Report, Annual market update 2017*.

[23] George M. Dadd, Dominic A. Hudson, and R. A. Shenoi. "Comparison of Two Kite Force Models with Experiment". In: *Journal of Aircraft* 47.1 (2010), pp. 212–224. DOI: 10.2514/1.44738. URL: https://doi.org/10.2514/1.44738.

[24] *DAR Corporation Advanced Aircraft Analysis*. URL: https://www.darcorp.com/Software/AAA/.

[25] Moritz Diehl. "Real-Time Optimization for Large Scale Nonlinear Processes". In: 920 (Jan. 2001).

[26] D.Marchiori. *RVSM Air Data Test Sets - Pitot-static Test Equipment*. URL: https://www.dma-aero.com/eu/products/rvsm-air-data-test-sets.

[27] ECORYS. *Study on challenges in the commercialisation of airborne wind energy systems*. Tech. rep. Directorate-General for Research and Innovation (European Commission), 2018. DOI: 10.2777/87591.

[28] N. El-Sheimy, H. Hou, and X. Niu. "Analysis and Modeling of Inertial Sensors Using Allan Variance". In: *IEEE Transactions on Instrumentation and Measurement* 57.1 (2008), pp. 140–149. ISSN: 0018-9456. DOI: 10.1109/TIM.2007.908635.

[29] Michael Erhard, Greg Horn, and Moritz Diehl. "A quaternion-based model for optimal control of the SkySails airborne wind energy system". In: *CoRR* abs/1508.05494 (2015).

[30] Michael Erhard and Hans Strauch. "Control of Towing Kites for Seagoing Vessels". In: *IEEE Transactions on Control Systems Technology* 21 (Feb. 2012). DOI: 10.1109/TCST.2012.2221093.

[31] E&Y. *Technology Readiness Level: Guidance Principles for Renewable Energy technologies*. Tech. rep. Directorate-General for Research and Innovation (European Commission), 2017. DOI: 10.2777/577767.

[32] L. Fagiano. "Control of Tethered Airfoils for High-Altitude Wind Energy Generation - Advanced control methods as key technologies for a breakthrough in renewable energy generation [Doctoral dissertation - Ph.D. in Information and System Engineering - Ciclo XXI - Politecnico di Torino]". In: 2009.

[33] L. Fagiano, A. U. Zgraggen, M. Morari, and M. Khammash. "Automatic Crosswind Flight of Tethered Wings for Airborne Wind Energy: Modeling, Control Design, and Experimental Results". In: *IEEE Transactions on Control Systems Technology* 22.4 (2014), pp. 1433–1447. ISSN: 1063-6536. DOI: 10.1109/TCST.2013.2279592.

[34] Uwe Fechner, Rolf van der vlugt, Edwin Schreuder, and Roland Schmehl. "Dynamic Model of a Pumping Kite Power System". In: *Renewable Energy* (Sept. 2015). DOI: 10.1016/j.renene.2015.04.028.

[35] Liquid Force. *Liiquid Force HiFi X*. URL: https://liquidforce.com/.

[36] R Fouquet. "International handbook on the economics of energy". In: ed. by UK:Edward Elgar Publishing Cheltenham. Chap. A brief history of energy, pp. 1–19.

[37] T. J.; Galbrith T. J.; Petersen and E. C. Roth. *A Computer System for Identifying Aircraft Characteristics from Flight Test Data.* Tech. rep. The Boeing Co., 1976.

[38] Demoz Gebre-Egziabher, Gabriel H. Elkaim, J. David Powell, and Bradford W. Parkinson. "Calibration of Strapdown Magnetometers in Magnetic Field Domain". In: *Journal of Aerospace Engineering* 19.2 (2006), pp. 87–102. DOI: `10.1061/(ASCE)0893-1321(2006)19:2(87)`. eprint: `https:// ascelibrary.org/doi/pdf/10.1061/%28ASCE%290893-1321%282006% 2919%3A2%2887%29`. URL: `https://ascelibrary.org/doi/abs/10. 1061/%28ASCE%290893-1321%282006%2919%3A2%2887%29`.

[39] O. H Gerlach. "Determination of Performance,Stability and Control Characteristics from Measurements in Nonsteady Maneuvers". In: *Stability and Control, AGARD*. 17. 1966, pp. 499–523.

[40] Jacek A. Goszczyński, Wiesław J.J. Michalski, and Józef A. Pietrucha. "Estimation before modelling as the method for identification of the aircraft aerodynamic characteristics in nonlinear flight regime". In: *Journal of Theoretical and Applied Mechanics* 38.1 (2000). URL: `http://www.ptmts.org.pl/ jtam/index.php/jtam/article/view/v38n1p107`.

[41] Jared Grauer and Eugene A. Morelli. "A Generic Nonlinear Aerodynamic Model for Aircraft". In: Jan. 2014. DOI: `10.2514/6.2014-0542`.

[42] *GreenKite*. Funded by the Ministerio de Ciencia e Innovación of Spain and the European Regional Development Fund (ENE2015-69937-R, MINECO/FEDER, UE). 2016-2019.

[43] *GreenKite2*. Funded by the Agencia Estatal de Investigación of Spain (PID2019-110146RB-I00 /AEI/10.13039/501100011033). 2020-2023.

[44] S. G. C. De Groot, J. Breukels, R. Schmehl, and W. J. Ockels. "Modelling Kite Flight Dynamics Using a Multibody Reduction Approach". In: *Journal of Guidance, Control, and Dynamics* 34.6 (2011), pp. 1671–1682. ISSN: 0731-5090. DOI: `10.2514/1.52686`. URL: `https://doi.org/10.2514/1.52686`.

[45] N. K.; Hall W. E. Jr; Gupta and J. S. Tyler. "Model Structure Determination and Parameter Identification for Nonlinear Aerodynamic Fligh Regimes." In: *Stability and Control, AGARD*. Vol. CP-174. 21. 1974.

[46] J. C. Hoff and M. V. Cook. "Aircraft parameter identification using an estimation-before-modelling technique". In: *The Aeronautical Journal (1968)* 100.997 (Sept. 1996), pp. 259–268. DOI: `10.1017/S000192400002889X`. URL: `https: //www.cambridge.org/core/article/aircraft-parameter-identification- using-an-estimation-before-modelling-technique/7504DAB2C0CD496F590433584A`.

[47] B. Houska. "A 9 DOF Kite Model". In: *Internal Paper, University of Heidelberg.* (2007).

[48] Boris Houska and Moritz Diehl. "Optimal Control for Power Generating Kites". In: *2007 European Control Conference, ECC 2007* (Jan. 2006).

[49] Boris Houska and Moritz Diehl. "Optimal Control of Towing Kites". In: Jan. 2007, pp. 2693 –2697. DOI: 10.1109/CDC.2006.377210.

[50] Jan Hummel, Dietmar Göhlich, and Roland Schmehl. "Automatic measurement and characterization of the dynamic properties of tethered membrane wings". In: *Wind Energy Science* 4 (Jan. 2019), pp. 41–55. DOI: 10.5194/wes-4-41-2019.

[51] J.C. Hung and H.V. White. "On IMU Self-Alignment Algorithms". In: *IFAC Proceedings Volumes* 8.1, Part 4 (1975). 6th IFAC World Congress (IFAC 1975) - Part 3: Systems, Economics, Management, and Social Effects, Boston/Cambridge, MA, USA, August 24-30, 1975, pp. 436 –445. ISSN: 1474-6670. DOI: https://doi.org/10.1016/S1474-6670(17)67499-8. URL: http://www.sciencedirect.com/science/article/pii/S1474667017674998.

[52] ICAO. *Manual of the ICAO Standard Atmosphere: Extended to 80Kilometers (262,500 Feet)*. Tech. rep. 7488/3. International Civil Organization (ICAO), 1993.

[53] IEEE. "IEEE Standard Specification Format Guide and Test Procedure for Single-Axis Interferometric Fiber Optic Gyros". In: *IEEE Std 952-1997* (1998), pp. 1–84. DOI: 10.1109/IEEESTD.1998.86153.

[54] Wubbo J. Ockels. "Laddermill, a novel concept to exploit the energy in the airspace". In: *Aircraft Design* 4 (June 2001), pp. 81–97. DOI: 10.1016/S1369-8869(01)00002-7.

[55] Claudius Jehle, Automatische Flugregelung, seilgebundener Lenkdrachen, and Eidesstattliche Erklärung. "Automatic Flight Control of Tethered Kites for Power Generation". In: 2012.

[56] *kiteGen Research*. URL: http://www.kitegen.com/en/.

[57] *kitePower*. URL: https://www.kitepower.nl/.

[58] V Klein and J.R Schiess. *rections. Ph.D. Thesis, Delft Tech. Univ., The Netherlands, 1976. Compatibility Check of Measured Aircraft Responses Using Kinematic Equation and Extended Kalman Filter*. Tech. rep. NASA, Langley Research Center, 1977.

[59] M Lee and C-M Ho. "Vortex Dynamics of Delta Wings". In: *Frontiers in Experimental Fluid Mechanics*. Ed. by M Gad-el Hak. Berlin Heidelberg: Springer, 1989, pp. 365–427. DOI: 10.1007/978-3-642-83831-6_8.

[60] Giovanni Licitra, Adrian Bürger, Paul Williams, Richard Ruiterkamp, and Moritz Diehl. "System Identification of a Rigid Wing Airborne Wind Energy System". In: (Nov. 2017).

[61] X DEVELOPMENT LLC. *Harnessing wind energy with kites to create renewable electricity*. URL: https://x.company/projects/makani/.

[62] M. L. Loyd. "Crosswind kite power". In: *Journal of Energy* 4.3 (1980), pp. 106–111. ISSN: 0146-0412. DOI: 10.2514/3.48021. URL: http://dx.doi.org/10.2514/3.48021.

[63] A Lucas. *Wind, Water, Work: Ancient and Medieval Milling Technology*. Vol. 8, Technology and Change in History. The Netherlands: Brill Academic Publishers., 2006.

[64] JM Luckring. "The discovery and prediction of vortex flow aerodynamics". In: *The Aeronautical Journal* 123.1264 (2019), pp. 729–804. DOI: 10.1017/aer.2019.43.

[65] *Makani*. URL: https://www.makanipower.com/.

[66] I. Martín. "Flight testing of power kites." Director: G. Sánchez-Arriaga. MA thesis. UC3M, 2017.

[67] K. Marvel, B. Kravitz, and K. Caldeira. "Geophysical limits to global wind power". In: *Nature Climate Change* 3 (Feb. 2013), pp. 118–121. DOI: 10.1038/nclimate1683.

[68] Garth Milne, M. Soijer, S. Juliana, MR. Hermansyah, and J. Mulder. "Maximum likelihood stability and control derivative identification of a Cessna Citation II". In: *AIAA Atmospheric Flight Mechanics Conference and Exhibit*. American Institute of Aeronautics and Astronautics, 2001. DOI: doi:10.2514/6.2001-4013. URL: https://doi.org/10.2514/6.2001-4013.

[69] J. A. Molusis. *Analytical study to define a helicopter stability derivative extraction method, volume 1*. Tech. rep. Sikorsky Aircraft Division, 1973.

[70] Eugene A. Morelli. "Global nonlinear aerodynamic modeling using multivariate orthogonal functions". In: *Journal of Aircraft* 32.2 (1995), pp. 270–277. DOI: 10.2514/3.46712. URL: https://doi.org/10.2514/3.46712.

[71] J.A. Mulder, Q Chu, J.K. Sridhar, Jan Breeman, and Martin Laban. "Non-linear aircraft flight path reconstruction review and new advances". In: *Progress in Aerospace Sciences* 35 (Oct. 1999), pp. 673–726.

[72] J. Oehler and R. Schmehl. "Aerodynamic characterization of a soft kite by in situ flow measurement". In: *Wind Energy Science* 4.1 (2019), pp. 1–21. DOI: 10.5194/wes-4-1-2019. URL: https://www.wind-energ-sci.net/4/1/2019/.

[73] A. Otero. "Control System and Hardware-related Elements Applied to Flight Testing of Airborne Wind Energy Systems." Director: G. Sánchez-Arriaga. MA thesis. UC3M, 2018.

[74] A. Pastor-Rodríguez, G. Sánchez-Arriaga, and M. Sanjurjo-Rivo. "Modeling and Stability Analysis of Tethered Kites at High Altitudes". In: *Journal of Guidance, Control, and Dynamics* 40.8 (2017), pp. 1892–1901. ISSN: 0731-5090. DOI: 10.2514/1.G002550. URL: https://doi.org/10.2514/1.G002550.

[75] Lichota Piotr and Lasek Maciej. "meceng". In: vol. 60. 2. 2013. Chap. Maximum Likelihood Estimation for Identification of Aircraft Aerodynamic Derivatives, p. 219. DOI: `10.2478/meceng-2013-0014`. URL: `https://www.degruyter.com/view/j/meceng.2013.40.issue-2/meceng-2013-0014/meceng-2013-0014.xml`.

[76] ProfiCNC. *PixHawk2*. URL: `http://www.proficnc.com/content/13-pixhawk2`.

[77] Secretaría General Técnica. Subdirección General De Desarrollo Normativo Informes y Publicaciones. "La energía en España 2016". In: Ministerio De Energía, Turismo y Agenda Digital, 2016, p. 29.

[78] M. Bolinger R. Wiser. *2015 Wind Technologies Market Report*. 2015. URL: `https://energy.gov/sites/prod/files/2016/08/f33/2015-Wind-Technologies-Market-Report-08162016.pdf`.

[79] S. Ramachandran, H. Schneider, J. Mason, and H. Stalford. In: Guidance, Navigation, and Control and Co-located Conferences. American Institute of Aeronautics and Astronautics, 1977. Chap. Identification of aircraft aerodynamic characteristics at high angles of attack and sideslip using the estimation before modeling /EBM/ technique. DOI: `10.2514/6.1977-1169`. URL: `https://doi.org/10.2514/6.1977-1169`.

[80] D. Ramiro-Rebollo. "Flight Testing Rig for Airborne Wind Energy Systems." Director: G. Sánchez-Arriaga. MA thesis. UC3M, 2019.

[81] Hannah Ritchie. "Energy". In: *Our World in Data* (2014). https://ourworldindata.org/energy.

[82] Max Roser. "Future Population Growth". In: *Our World in Data* (2013). https://ourworldindata.org/future-population-growth.

[83] L. Salord Losantos and G. Sánchez-Arriaga. "Flight Dynamics and Stability of Kites in Steady and Unsteady Wind Conditions". In: *Journal of Aircraft* 52.2 (2014), pp. 660–666. DOI: `10.2514/1.C032825`. URL: `http://dx.doi.org/10.2514/1.C032825`.

[84] G. Sánchez. "Dynamics and Control of Single-Line Kites". In: *The Aeronautical Journal* 110.1111 (2006). DOI: `10.1017/S0001924000001470`.

[85] G. Sánchez-Arriaga, M. García-Villalba, and R. Schmehl. "Modeling and dynamics of a two-line kite". In: *Applied Mathematical Modelling* 47 (2017), pp. 473 –486. ISSN: 0307-904X. DOI: `https://doi.org/10.1016/j.apm.2017.03.030`. URL: `http://www.sciencedirect.com/science/article/pii/S0307904X17301798`.

[86] G. Sánchez-Arriaga, A. Pastor-Rodríguez, R. Borobia-Moreno, and R. Schmehl. "A constraint-free flight simulator package for airborne wind energy systems". In: *Journal of Physics: Conference Series* 1037 (2018), p. 062018. DOI: `10.1088/1742-6596/1037/6/062018`. URL: `https://doi.org/10.1088%2F1742-6596%2F1037%2F6%2F062018`.

[87] G. Sánchez-Arriaga, A. Pastor-Rodríguez, M. Sanjurjo-Rivo, and R. Schmehl. "A lagrangian flight simulator for airborne wind energy systems". In: *Applied Mathematical Modelling* 69 (2019), pp. 665 –684. ISSN: 0307-904X. DOI: https://doi.org/10.1016/j.apm.2018.12.016. URL: http://www.sciencedirect.com/science/article/pii/S0307904X18306267.

[88] Eduardo Schmidt, Marcelo De Lellis, Ramiro Saraiva, and Alexandre Trofino. "State Estimation of a Tethered Airfoil for Monitoring, Control and Optimization**This work was supported by CNPq through grants 480931/2013-5 and 406996/2013-0, and CAPES, Brazil." In: *IFAC-PapersOnLine* 50.1 (2017). 20th IFAC World Congress, pp. 13246 –13251. ISSN: 2405-8963. DOI: https://doi.org/10.1016/j.ifacol.2017.08.1960. URL: http://www.sciencedirect.com/science/article/pii/S2405896317325909.

[89] Richard Semik. *Molinos de viento, Campo de Criptana, Castilla-La Mancha, España*. [Online; accessed June 29, 2020]. URL: https://www.shutterstock.com/image-photo/windmills-campo-de-criptana-castilela-mancha-68379724.

[90] A. Serino. "On-board instruments and flight tests of giant kites applied to wind power generation." Director: G. Sánchez-Arriaga. MA thesis. Politecnico de Torino, 2016.

[91] FLYSURFER Kiteboarding | Brand of Skywalk GmbH & Co. KG. *Flysurfer Soul*. URL: https://flysurfer.com/project/soul/.

[92] M. Sri-Jayantha and R. F. Stengel. "Determination of nonlinear aerodynamic coefficients using the estimation-before-modeling method". In: *Journal of Aircraft* 25.9 (1988), pp. 796–804. ISSN: 0021-8669. DOI: 10.2514/3.45662. URL: https://doi.org/10.2514/3.45662.

[93] J Stevenson, K Alexander, and P Lynn. "Kite performance testing by flying in a circle". In: *The Aeronautical Journal* 109 (June 2005), pp. 269–276. DOI: 10.1017/S0001924000000725.

[94] J.C. Stevenson. *Traction Kite Testing and Aerodynamics: A Thesis Submitted in Partial Fulfilment of the Requirements for the Degree of Doctor of Philosophy in Mechanical Engineering in the University of Canterbury*. University of Canterbury, 2003. URL: https://books.google.es/books?id=2yZcMgAACAAJ.

[95] NCEI Geomagnetic Modeling Team and British Geological Survey. *World Magnetic Model 2020*. Tech. rep. NOAA National Centers for Environmental Information, 2019. DOI: 10.25921/11v3-da71.

[96] Axelle Viré, Patryk Demkowicz, Mikko Folkersma, Arthur Roullier, and Roland Schmehl. "Reynolds-averaged Navier-Stokes simulations of the flow past a leading edge inflatable wing for airborne wind energy applications". In: *Journal of Physics: Conference Series* 1618 (2020), p. 032007. DOI: 10.1088/1742-6596/1618/3/032007.

[97]   R van der Vlugt. "Aero- and Hydrodynamic Performance Analysis of a Speed Kiteboarder". PhD thesis. Delft University of Technology, 2009.

[98]   A de Wachter. "Deformation and Aerodynamic Performance of a Ram-Air Wing". MSc Thesis. Delft University of Technology, 2008. DOI: `http://resolver.tudelft.nl/uuid:786e3395-4590-4755-829f-51283a8df3d2`.

[99]   Bernard J. Eulrich; Norman C. Weingarten. *Identification and Correlation of the F-4E Stall/Post-Stall Aerodynamic Stability and Control Characteristics from Existing Test Data Identification and Correlation of the F-4E Stall/Post-Stall Aerodynamic Stability and Control Characteristics from Existing Test Data Identification and Correlation of the F-4E Stall/Post-Stall Aerodynamic Stability and Control Characteristics from Existing Test Data*. Tech. rep. AFFDL TR 73-125. Calspan Corporation, 1973.

[100] Greg Welch and Gary Bishop. *An Introduction to the Kalman Filter*. Tech. rep. Chapel Hill, NC, USA, 1995.

[101] Paul Williams, Bas Lansdorp, and Wubbo Ockels. "Flexible Tethered Kite with Moveable Attachment Points, Part I: Dynamics and Control". In: *AIAA Atmospheric Flight Mechanics Conference and Exhibit*. American Institute of Aeronautics and Astronautics, 2007. DOI: `doi:10.2514/6.2007-6628`. URL: `https://doi.org/10.2514/6.2007-6628`.

[102] Paul Williams, Bas Lansdorp, and Wubbo Ockesl. "Optimal Crosswind Towing and Power Generation with Tethered Kites". In: *Journal of Guidance, Control, and Dynamics* 31.1 (2008), pp. 81–93. ISSN: 0731-5090. DOI: `10.2514/1.30089`. URL: `https://doi.org/10.2514/1.30089`.

[103] Paul Williams, Bas Lansdorp, Richard Ruiterkamp, and W.J. Ockels. "Modeling, Simulation, and Testing of Surf Kites for Power Generation". In: *AIAA Modeling and Simulation Technologies Conference and Exhibition, Honolulu, Hawaii, 18-21 August, 2008* (Aug. 2008). DOI: `10.2514/6.2008-6693`.

[104] R. C. Wingrove. "Parameter Estimation of Powered-Lift STOL Aircraft Characteristics Including Turbulence and Ground Effects." In: *Stability and Control AGARD*. 172. 1974.

[105] R.C. Wingrove. "Quasi-Linearizatioh Technique for Estimating Aircraft States from Flight Data". In: *Journal of Aircraft - J AIRCRAFT* 10 (May 1973), pp. 303–307. DOI: `10.2514/3.60230`.

[106] Haifeng Xing, Zhiyong Chen, Haotian Yang, Chengbin Wang, Zhihui Lin, and Meifeng Guo. "Self-Alignment MEMS IMU Method Based on the Rotation Modulation Technique on a Swing Base". In: *Sensors* 18 (Apr. 2018), p. 1178. DOI: `10.3390/s18041178`.

[107] Zhiqiang Xing and D. Gebre-Egziabher. "Modeling and bounding low cost inertial sensor errors". In: *2008 IEEE/ION Position, Location and Navigation Symposium*. Monterey, CA, USA, 2008, pp. 1122–1132. DOI: `10.1109/PLANS.2008.4569999`.